UNIVERSITY OF TASMANIA

INTEGRATED MICROCHIP METHODS FOR BIOLOGICAL AND ENVIRONMENTAL SAMPLE ANALYSIS

By

Aliaa Ibrahim Shallan

M.Sc. (Pharmacy)

School of Physical Sciences

Submitted in fulfilment of the requirements for the Degree of

Doctor of Philosophy

University of Tasmania (August 2015)

DECLARATION OF ORIGINALITY

This thesis contains no material which has been accepted for a degree or diploma by the University or any other institution, except by way of background information and duly acknowledged in the thesis, and to the best of my knowledge and belief no material previously published or written by another person except where due acknowledgement is made in the text of the thesis, nor does the thesis contain any material that infringes copyright.

AUTHORITY OF ACCESS

The publishers of the papers in this thesis (comprising Chapters One to Four and Chapter Seven) hold the copyright for that content, and access to the material should be sought from the respective journals. The remaining non-published content of the thesis may be made available for loan and limited copying and communication in accordance with the Copyright Act 1968.

STATEMENT OF ETHICAL CONDUCT

The research associated with this thesis abides by the international and Australian codes on human and animal experimentation, the guidelines by the Australian Government's Office of the Gene Technology Regulator and the rulings of the Safety, Ethics and Institutional Biosafety Committees of the University. Ethics Approval Ref is H0010801.

Aliaa Shallan

August 2015

This thesis is dedicated to…

The Giants whom I stand on their shoulders

" Simplicity is the ultimate sophistication."

Leonardo da Vinci

ACKNOWLEDGEMENTS

"All praise is due to Allah with whose favours all good can be accomplished"

No words can describe my gratitude towards my supervisors, Prof. Michael Breadmore and Dr. Rosanne Guijt. Thank you for making my PhD such a rich journey of professional and personal evolution. I deeply appreciate your extreme understanding of cultural differences and wisdom in handling your students.

Many thanks to CSL members, Mr. John Davis from the electric workshop, Mr. Peter Dove from the mechanical workshop, and Dr. Sandrin Feig and Dr. Karsten Goemann for taking SEM images.

Thanks to all past and present members of the Chippers & CEers group and to the extended family of ACROSS members. I could not feel homesick for the whole period of my study. Thanks for those who came out of their way to help me whenever needed. Thanks for seeking my advice to solve your problem, I learned from you as much as you learned from me. Thanks to my colleagues and friends in the School of Chemistry and the School of Pharmacy, I really enjoyed morning tea discussions.

Thanks to my papers' reviewers who I may never know but have dedicated time to review my work and give constructive feedback.

I would like to gratefully acknowledge the Egyptian Ministry of Higher Education for the financial support and Helwan University for allowing me to take a study leave and come to Australia for Ph.D. Special thanks to Prof. Mohamed Salem and Prof. Safaa Tubar for their constant support, directly or indirectly, since 1997.

My family, I understand your sacrifices and would never be able to repay.

STATEMENT OF CO-AUTHORSHIP

The majority of the work presented in this thesis was published and include the contribution of the following authors:

Paper 1, Shallan, A. I.; Gaudry, A. J.; Guijt, R. M.; Breadmore, M. C., Tuneable nanochannel formation for sample-in/answer-out devices. *Chemical Communications* 2013, 49 (27), 2816-2818.

This paper constitutes 30% of the experimental part of Chapter One and Chapter Three. Ms. Aliaa Shallan was the first author and conducted all the experimental work, data analysis and writing the manuscript. Dr. Adam Gaudry wrote the LabView program to control the power supply through feedback current, which was an essential element to the success of this work. Prof. Michael Breadmore suggested the idea of using current limit feedback to control the dielectric breakdown process. Dr. Rosanne Guijt and Prof. Michael Breadmore contributed equally to the idea and development of the work.

Paper 3, Shallan, A. I.; Guijt, R. M.; Breadmore, M. C., Electrokinetic size and mobility traps for on-site therapeutic drug monitoring. *Angewandte Chemie International Edition* 2015, 54, 7359-7362. DOI: 10.1002/anie.201501794.

This paper constitutes 30% of the experimental part of Chapter One and Chapter Three. Ms. Aliaa Shallan was the first author and conducted all the experimental work, data analysis and writing the manuscript. Dr. Rosanne Guijt suggested the application of the developed size/mobility traps for therapeutic drug monitoring of ampicillin in septic patients. Dr. Rosanne Guijt and Prof. Michael Breadmore contributed equally to the idea and development of the work.

Book Chapter 2, Shallan, A. I.; Guijt, R. M.; Breadmore, M. C., Chapter 4. Microfluidic devices for the analysis of drugs and their metabolites in biological fluids in "Microfluidics, Nanotechnology and Disease Biomarkers for Personalized Medicine Applications", NOVA Science Publishers, Shiddiky, M. J. A.; Wee, E. J. H.; Rauf, S.; Trau, M., (ed), United States, pp. 73-98. ISBN 978-1628080209 (2013)

This book chapter constitutes Chapter Two. Ms. Aliaa Shallan was the first author (80%) contribution. Dr. Rosanne Guijt and Prof. Michael Breadmore contributed equally to the refinement of the text.

Review 3, Shallan, A. I.; Guijt, R. M.; Breadmore, M. C., Electrokinetics for sample preparation of biological molecules in biological samples using microfluidic systems. *Bioanalysis* 2014, 6 (14), 1961-1974.

This book chapter constitutes Chapter Four. Ms. Aliaa Shallan was the first author (80%) contribution. Dr. Rosanne Guijt and Prof. Michael Breadmore contributed equally to the refinement of the text.

Paper 2, Shallan, A. I.; Smejkal, P.; Corban, M.; Guijt, R. M.; Breadmore, M. C., Cost-effective three-dimensional printing of visibly transparent microchips within minutes. *Analytical Chemistry* 2014, 86, 3124-3130.

This paper constitutes Chapter Seven. Ms. Aliaa Shallan was the first author and conducted all the experimental work, data analysis and writing the manuscript. Dr. Petr Smejkal assisted in performing nitrate analysis using the printed device and Mrs. Monica Corban prepared the solutions only for that experiment. Prof. Michael Breadmore suggested the design for the nitrate analysis device. Dr. Rosanne Guijt and

Prof. Michael Breadmore contributed equally to the idea, refinement of the 3D-devices design and development of the work.

We the undersigned agree with the above stated "proportion of work undertaken" for each of the above published peer-reviewed manuscripts contributing to this thesis:

Signed:

Prof. Michael C. Breadmore	Prof. John Dickey
Supervisor	Head of School
School of Physical Sciences	School of Physical Sciences
University of Tasmania	University of Tasmania
Date: 10/9/2015	11/9/15

LIST OF PUBLICATIONS

Type of Publications	References
Papers in refereed Journals & book chapters	8
Posters at national and international conferences	6
Oral presentations at international conferences	5

1. Shallan, A. I.; Guijt, R. M.; Breadmore, M. C., Capillary electrophoresis: Basic principles in "*Encyclopedia of Forensic Sciences*" (Eds.: A. S. Editors-in-Chief: Jay, J. S. Pekka), Academic Press, Waltham, pp. 549-559. ISBN 978-0-12-382166-9 (**2013)**.
2. Shallan, A. I.; Guijt, R. M.; Breadmore, M. C., Chapter 4. Microfluidic devices for the analysis of drugs and their metabolites in biological fluids in "*Microfluidics, Nanotechnology and Disease Biomarkers for Personalized Medicine Applications*", NOVA Science Publishers, Shiddiky, M. J. A.; Wee, E. J. H.; Rauf, S.; Trau, M., (ed), United States, pp. 73-98. ISBN 978-1628080209 (**2013**). (Chapter Two)
3. Breadmore, M. C.; Shallan, A. I.; Rabanes, H. R.; Gstoettenmayr, D.; Abdul Keyon, A. S.; Gaspar, A.; Dawod, M.; Quirino, J. P., Recent advances in enhancing the sensitivity of electrophoresis and electrochromatography in capillaries and microchips (2010–2012). *Electrophoresis* **2013**, 34 (1), 29-54. DOI: 10.1002/elps.201200396.
4. Breadmore, M. C.; Tubaon, R. M.; Shallan, A. I.; Phung, S. C.; Abdul Keyon, A. S.; Gstoettenmayr, D.; Prapatpong, P.; Alhusban, A. A.; Ranjbar, L.; See,

H. H.; Dawod, M.; Quirino, J. P., Recent advances in enhancing the sensitivity of electrophoresis and electrochromatography in capillaries and microchips (2012–2014) *Electrophoresis* **2015**, 36, 36-61. DOI: 10.1002/elps.201400420.

5. Shallan, A. I.; Guijt, R. M.; Breadmore, M. C., Electrokinetics for sample preparation of biological molecules in biological samples using microfluidic systems. *Bioanalysis* **2014**, 6 (14), 1961-1974. DOI: 10.4155/bio.14.140. (Chapter Four)
6. Shallan, A. I.; Gaudry, A. J.; Guijt, R. M.; Breadmore, M. C., Tuneable nanochannel formation for sample-in/answer-out devices, *Chemical Communications*, **2013**, 49, 2816-2818. DOI: 10.1039/c3cc38330j. (Chapters One and Three)
7. Shallan, A. I.; Smejkal, P.; Corban, M.; Guijt, R. M.; Breadmore, M. C., Cost-effective three-dimensional printing of visibly transparent microchips within minutes. *Analytical Chemistry* **2014**, 86, 3124-3130. DOI: 10.1021/ac4041857. (Chapter Seven)
8. Shallan, A. I.; Guijt, R. M.; Breadmore, M. C., Electrokinetic size and mobility traps for on-site therapeutic drug monitoring. *Angewandte Chemie International Edition* **2015**, 54, 7359-7362. DOI: 10.1002/anie.201501794. (Chapters One and Three)
9. Shallan, A. I.; Guijt, R. M.; Breadmore, M. C., Integrated polydimethylsiloxane membrane for protein removal. *UTAS postgraduate Conference (SEiR)*, University of Tasmania, Australia, 1-2 September **2011**. (Poster)
10. Shallan, A. I.; Guijt, R. M.; Breadmore, M. C., Integrated polydimethylsiloxane membrane for protein removal. *The 11th Asia-Pacific*

International Symposium on Microscale Separations and Analysis (APCE), Hobart, Australia, 28-30 November **2011**. (Poster)

11. Shallan, A. I.; Guijt, R. M.; Breadmore, M. C., Integrated polydimethylsiloxane membrane for protein removal. *The 19th RACI Research and Development Topics Conference*, Melbourne, Australia, 7-9 December **2011**. (Poster)
12. Shallan, A. I.; Gaudry, A. J.; Guijt, R. M.; Breadmore, M. C., Integrated polydimethylsiloxane membrane for protein removal. *The 3rd Australia & New Zealand Micro/Nanofluidics and Bionano Symposium (ANZMNF)*, Wellington, New Zealand. 12-13 April **2012**. (Oral)
13. Shallan, A. I.; Gaudry, A. J.; Guijt, R. M.; Breadmore, M. C., Integrated polydimethylsiloxane membrane for protein removal. *The 28th International Symposium on Microscale Bioseparations (MSB)*, Shanghai, China, 21-24 October **2012**. (Poster)
14. Shallan, A. I.; Gaudry, A. J.; Guijt, R. M.; Breadmore, M. C., Integrated polydimethylsiloxane membrane for protein removal. *The 16th International Conference on Miniaturized Systems for Chemistry and Life Sciences (μTAS)*, Okinawa, Japan, 28 October - 1 November **2012**. (Poster)
15. Breadmore, M. C., Simple and sensitive electrophoretic methods for the detection of pharmaceuticals in biological fluids. *Latin-American Symposium on Biotechnology, Biomedical, Biopharmaceutical and Industrial Applications of Capillary Electrophoresis (LACE 2012)*, Buenos Aires, Argentina, 30 November - 4 December **2012**. (Invited plenary lecture)

16. Breadmore, M. C., Microfluidic device with nanochannels for sample-in/answer-out capability of small molecules in blood. *The 29th MSB*, Charlottesville, USA, 10-14 March **2013**. (Poster)
17. Shallan, A. I.; Guijt, R. M.; Breadmore, M. C., (2013, April). 3D-printed microchips. *The 4th ANZMNF*, Adelaide, Australia, 22-24 April **2013**. (Oral)
18. Breadmore, M. C., Sample-in/answer-out electrophoretic systems. Invited seminar at Palacký University, Olomouc, Czech Republic, 14 October **2013**.
19. Breadmore, M. C., Sample-in/answer-out electrophoretic systems, Invited seminar at institute of Analytical Chemistry of the ASCR, Brno, Czech Republic, 16 October **2013**.
20. Shallan, A. I.; Smejkal, P.; Corban, M.; Guijt, R. M.; Breadmore, M. C., 3D-printed microchips. *The 40th International Symposium on High Performance Liquid Phase Separations and Related Techniques (HPLC)*, Hobart, Australia, 18-21 November **2013**. (Oral)
21. Shallan, A. I.; Smejkal, P.; Corban, M.; Guijt, R. M.; Breadmore, M. C., 3D-printed microchips. *The 5th ANZMNF*, Hobart, Australia, 14-16 April **2014**. (Oral)
22. Shallan, A. I.; Guijt, R. M.; Breadmore, M. C., Electrokinetic traps for integrated biological sample analysis. *CE in the Biotechnology & Pharmaceutical Industries: 16th Symposium on the Practical Applications for the Analysis of Proteins, Nucleotides and Small Molecules (CE Pharm 2014)*, Seattle, United States, 12-16 October **2014**. (Poster)
23. Breadmore, M. C.; Guijt, R. M.; Shallan, A. I., Microfabrication via 3D Printing. *The 18th μTAS*, San Antonio, United States, 26 October **2014**. (Workshop)

24. Shallan, A. I.; Guijt, R. M.; Breadmore, M. C., Electrokinetic traps for integrated biological sample analysis. *The 18th μTAS*, San Antonio, United States, 26 - 30 October **2014**. (Poster)
25. Shallan, A. I.; Smejkal, P.; Corban, M.; Guijt, R. M.; Breadmore, M. C., 3D printed microfluidic devices using consumer-focused printers. *Pittcon 2015*, New Orleans, United States, 8-12 March **2015**. (Oral)
26. Shallan, A. I.; Guijt, R. M.; Breadmore, M. C., Electrokinetic traps for integrated biological sample analysis. *The 6th ANZMNF*, Melbourne, Australia, 31 March - 2 April **2015**. (Oral)

LIST OF ABBREVIATIONS

3D	Three dimensional
ABS	Acrylonitrile-butadiene-styrene
AuNPs	Gold nanoparticles
b	Slip length
B	Buffer reservoir
BGE	Background electrolyte
BSA	Bovine serum albumin
BW	Buffer waste reservoir
CAD	Computer-aided design
CAPS	3-(cyclohexylamino)-1-propanesulfonic acid
CCD	Charge coupled device
C_e	Ion concentration inside the nanochannel
CE	Capillary electrophoresis
CEDIA	Cloned enzyme donor immunoassay
CGIA	Concentration gradient immunoassay
CHAPS	3-[(3-cholamidopropyl) dimethylammonio]-1-propanesulfonate
CNF	5-(and-6)-carboxynaphtho fluorescein
C_o	Bulk salt or ion concentration
CPRG	Chlorophenol red-β-galactopyranoside

CZE	Capillary zone electrophoresis
D	Diffusion coefficient
Da	Dalton
DGPMS	Diethoy (3-glycidyloxy propyl) methyl silane
DIA	Competitive diffusion immunoassay
DKA	Diabetic ketoacidosis
DMD	Digital micromirror device
DTT	Dithioerythritol
Du	Dukhin number
e	Elementary charge
EDC	Endocrine disrupting compounds
EDTA	Ethylene diamine tetraacetic acid
ELISA	Enzyme linked immunosorbent assay
EME	Electromembrane extraction
EOF	Electroosmotic flow
$e\Sigma$	Surface charge density
EDL	Electric double layer
E_e	Applied electric field
F	Faraday constant
FASI	Field amplified sample injection
FASS	Field amplified sample stacking

FDM	Fused deposition modelling
f_e	Volume electric forces
FIA	Flow injection analysis
FITC	Fluorescein isothiocyanate
FPIA	Fluorescence polarization immunoassay
GC	Gas chromatography
h	Nanochannel height
h	Hour
HF-LPME	Hollow fibre liquid phase microextraction
HPLC	High performance liquid chromatography
HPMC	Hydroxypropylmethyl cellulose
HRP	Horseradish peroxidase
IA	Immunoassay
IC	Ion chromatography
ICP	Ion concentration polarization
ICP-MS	Inductively coupled plasma mass spectrometer
ICU	Intensive care unit
IEF	Isoelectric focusing
INS	Insulin
ITP	Isotachophoresis
J(x)	Ionic flux

K	Conductance
k_B	Boltzman constant
κ_b	Bulk conductivity
κ_s	Surface conductivity
ℓ_B	Bjerrum length
LC	Liquid chromatography
LCD	Liquid crystal display
LCoS	Liquid crystal on silicon
$\boldsymbol{\ell_{Du}}$	Dukhin length
LE	Leading electrolyte
LED	Light emitting diode
LIF	Laser induced fluorescence
LLE	Liquid-liquid extraction
LOC	Lab-on-a-chip
LOD	Limit of detection
LOQ	Limit of quantitation
LOV	Lab-on-a-valve
MBE	Moving boundary electrophoresis
MCE	Microchip capillary electrophoresis
MEKC	Micellar electrokinetic chromatography
MES	2-(4-morpholino) ethanesulfonic acid

MS	Mass spectrometry
NED	N-(1-Naphthyl) ethylenediamine dihydrochloride
NOPE	2-nitrophenyloctylether
NS	Navier-Stokes
OVA	Ovalbumin
PAGE	Polyacrylamide gel electrophoresis
PBS	Phosphate buffer saline
PCR	Polymerase chain reaction
PDMS	Poly(dimethylsiloxane)
PEEK	Polyetheretherketone
pI	Isoelectric point
PMMA	Poly(methylmethacrylate)
POC	Poin-of-care
PVA	Polyvinyl alcohol
PVP	Polyvinyl pyrrolidone
R	Gas constant
RSD	Relative standard deviation
R6G	Rhodamine 6G
S	Sample reservoir
SDS	Sodium dodecyl sulphate
SEM	Scanning electron microscope

SL	Stereolithography
SLM	Supported liquid membrane
SMT	Size/mobility trap
S/N	Signal-to-noise-ratio
SPE	Solid-phase extraction
SPR	Surface plasmon resonance
ssDNA	Single strand deoxyribonucleic acid
SW	Sample waste reservoir
T	Absolute temperature in Kelvin
TDM	Therapeutic drug monitoring
TE	Terminating electrolyte
tITP	Transient isotachophoresis
Tris	tris(hydroxymethyl)-aminomethane
TRITC	Tetramethylrhodamine isothiocyanate
UV	Ultraviolet
V_{el}	Electrostatic interaction
V_D	Donnan potential
Z	Valence of an ionic species
β-LG	β-lactoglobulin
βOHB	Beta-hydroxybutyrate
ε	Dielectric constant

ΔV	Electric field applied across the nanochannel
$\Delta\rho_s$	Salt concentration difference across the nanochannel
λ_D	Debye length
λ_{em}	Emission wavelength
λ_{ex}	Excitation wavelength
λ_S	Analyte-specific length scale
μ_{EO}	Electroosmotic velocity
μFIA	Miniaturized flow injection analysis
μTAS	Micrototal analysis system
η	Fluid viscosity
ρ_e	Charge density
ρ_s	Solution ionic strength
ψ	Electrical potential at a solid/liquid interface
ζ	Zeta potential
^oC	Degree centigrade

ABSTRACT

The introduction of the "microscale total analysis system (μTAS)" concept in the late 80's triggered the evolution of microfluidic devices that cover a vast range of applications. Automation, integration of multiple processes, and near zero dead volume for separation techniques are some benefits. Closing the gap between research and commercialization in a resource-limited environment is the main aim of this research.

This project feeds into two main streams. The first is to integrate on-chip sample preparation for biological applications, like therapeutic drug monitoring (TDM) and diagnostics, using nanojunctions created by controlled dielectric breakdown (Chapters One - Five). The second part focuses on fast prototyping of microfluidic devices with multiple integrated functionalities using a consumer-based 3D-printer (Chapters Six & Seven). These two approaches were tailored to solve specific problems inherent to each sample type and application.

Chapter One starts with a general introduction to the unique ion transport phenomena associated with nanojunctions. Many factors act together to determine whether a certain ion will be blocked or preferentially transported through the nanojunction. I developed controlled dielectric breakdown as a cost-effective alternative to conventional nanolithography methods. Pore size control was achieved by tuning the breakdown voltage in response to the feedback current measured through the formed nanojunction. Higher pre-set current limits result in larger pore size and hence the nanojunction will be permeable to larger molecules. I demonstrate the use of single nanojunction for simple extraction and the use of two nanojunctions acting together to form a size/mobility trap (SMT) for the simultaneous extraction,

concentration, and desalting. In the SMT format, the second nanojunction was introduced on the other side of the separation channel and offset by a 500 μm. While the role of the first junction remains the same, extraction, the second junction made with smaller pore size blocks the analyte but permits smaller ions. The two nanojunctions work together as a trap that concentrates the injected plug and simultaneously desalt it. This approach is very flexible and can be tuned for different applications as demonstrated in the following chapters.

Chapter Two is an introduction to microfluidic systems used for analysis of small molecules, especially pharmaceuticals, in biological samples. The methods were reviewed regarding the hardware and fluid handling processes. The chapter concludes by discussing the requirements for point-of-care devices and decision making based on the results obtained. There are still many challenges and issues that need to be addressed before the wide spread use of these devices becomes a reality.

In Chapter Three, the pore size of the nanojunctions was optimized for the analysis of small molecules in blood. First, a single nanojunction was integrated between the sample compartment and the separation channel of the microfluidic device. The nanojunction will permit the analyte of interest and small ions but block blood cells and other macromolecules. Isotachophoresis (ITP) and blue light emitting diodes (LEDs) were employed for the determination of small organic acids in blood with indirect fluorescence detection. The acids chosen in this study were pyruvate, lactate, and 3-hydroxy butyrate due to their significance as biomarkers for diabetes and ketoacidosis. The single nanojunction allowed for the extraction of acids directly from whole blood within 60 s without interference from other macromolecules. The limit of detection (LOD) was 12.5 mM and can be further improved by changing the microchannel geometry near the detection point.

The need for point-of-care devices for TDM was addressed through two examples: quinine (an example for positively charged drug) and ampicillin (an example for negatively charged drug). Quinine is a counter-ion at the experimental conditions employed, which is also the case for many pharmaceuticals like antidepressants, and hence its transport is favoured through the negatively charged nanojunction. A single nanojunction was integrated between the sample compartment and the separation channel of the microfluidic device for extraction. Peak mode ITP was employed to concentrate the injected plug and achieve a linear response that covers the therapeutically relevant range. Direct fluorescence detection was feasible due to the native fluorescence of quinine.

Finally, SMTs were employed for TDM of ampicillin. This eliminated the need to use other preconcentrating techniques like ITP. The electroosmotic flow (EOF) can be tuned in relation to the electrophoretic mobility by carefully selecting the buffers in the separation channel and the waste/desalting channel. This enables trapping of ions within a certain size/mobility range. Ampicillin is one of the front line antibiotics used for managing sepsis, a critical condition with 30-50% mortality rate. The device may facilitate accurate dose adjustment and improve the survival of septic patients.

Chapter Four is a general introduction to different electrokinetic methods for biological sample pretreatment with an interest in biopolymers like proteins and DNA. A special attention was given to devices that incorporate nanojunctions as they exhibit unique behaviour and have already being demonstrated for DNA manipulation, protein concentration, and single molecule detection. Their use was highlighted for sample pretreatment processes like purification, extraction, and concentration.

Chapter Five demonstrates the use of the developed nanojunction methods for biopolymer applications. The single nanojunction format was employed to concentrate sodium dodecyl sulphate (SDS)-protein complexes from high ionic strength buffers. Enhancement factors up to 80-fold were achieved within 200 s. The above mentioned SMTs were employed for the direct extraction of short single strand DNA (ssDNA), 20 bases, from blood. As examined with small molecules, DNA molecules were extracted into the separation channel while cells and proteins were blocked. The second nanojunction trapped the DNA in the separation channel leading to simultaneous concentration and desalting. The LOD achieved for fluorescein labelled DNA was 12.5 nM.

Chapter Six is an introduction to 3D-printing. Different modes were discussed and compared regarding their capabilities and suitability for microfluidic applications. This was followed by brief discussion of the recent portable systems reported for environmental analysis and design requirements in comparison to biological samples.

Chapter Seven explores the microfabrication capabilities of a desktop 3D-printer based on stereolithography (SL). The printer employed for this work is a commercially available low-cost printer that photocures a clear resin that resembles polymers commonly used for large-scale manufacturing. A wide range of microfluidic processes was demonstrated like mixing, gradient generation, droplet extraction and ITP. Multiple functionalities were integrated into one device for nitrate analysis in water. The final design features standard addition at five levels to correct for the matrix effect, passive mixers to shorten reaction time, and detection at different path lengths to extend the linear response range and accommodate samples regardless of their initial concentration. Development and refining of the design was accelerated by the short turn-around times as 3D objects were printed at 2 cm/h speed, in height

regardless of xy dimensions. The low price of the printer makes it a very accessible tool for small research laboratories.

In Chapter Eight, I summarise the findings of this project and suggest future directions. The outcomes of this research provide valuable solutions for multiple process integration for on-site analysis. Whether it is dielectric breakdown for controlled integration of nanojunctions or fast prototyping of complex devices, both approaches are simple and low-cost. They are suitable for disposable devices and on-site analysis and there is still a great opportunity for improvement in this area.

PREFACE

Personalized medicine promises better clinical outcomes and better global health but socioeconomic factors hinder its wide application. It relies on genetic testing and TDM to ensure that the right drug is prescribed for the patient at the optimum amount and dosing interval thus improving efficacy and minimizing toxicity. Most of the effort so far has been developing genetic tests as these provide information for better matching of the drug and patient individuality with an increasing number of instances where the US Food and Drug Administration (FDA) recommends genotyping before treatment, for example warfarin, clopidogrel and tamoxifen. While this information is highly valuable to ensure the desired suitability of the drug for the patient, these tests fail to identify intra-patient pharmacokinetic variability that evolves due to a progressing disease state, drug-drug interaction, or even dietary and life style changes.

Information regarding the pharmacokinetics can be obtained when analysing the patients' sample as done in the traditional context of TDM to ensure correct administration of narrow therapeutic window drugs. Conventional analytical methods, however, are restricted to central laboratories equipped with complicated instrumentation and are operated by professionally trained personnel. The required sample and reagent volumes are in the order of mL and turnaround times range from hours to days. Broadening the application of TDM in this context will cause a significant financial burden, overload clinical laboratories and struggle to meet the timeframe required between collection and corrective action.

The introduction of the μTAS concept in the late 80's by Manz[1] brought great hopes to biochemists and health care practitioners, promising the dream of on-site monitoring. Miniaturized systems give results within minutes or even seconds

consuming nano- to micro-litres of samples and reagents. The development of point-of-care (POC) devices based on this concept involves the integration of multiple processes into a low-cost, portable platform that is easy to use without compromising the quality of results. An excellent and well-established example that demonstrates the significance of such devices is the glucose blood meters.[2]

The extraction of the target analytes from biological samples is still the bottleneck in analysis and in the development of novel instrumentation for POC analysis. Unless a specific enzyme mediated or immunoassay is utilized, direct measurement of pharmaceuticals in whole blood requires sample pretreatment to remove blood cells, plasma proteins, and endogenous macromolecules. It is only integration of these and other analytical steps into a microfluidic platform capable of conducting the analysis in a fully automated manner is required for at-home monitoring or POC analysis.

I addressed this issue by introducing nanojunctions with adjustable permeability. Controlled dielectric breakdown was employed to create nanojunctions of different pore size to govern ionic transport based on the ion charge and hydrodynamic size. The method utilises simple microfluidic structures and is highly suited for disposable devices. Combining two nanojunctions with different pore size creates an electrokinetic Size Mobility Trap (SMT). The simultaneous extraction and concentration of pharmaceuticals from biological fluids was seamlessly followed by electrophoretic separation for quantitative analysis. The presented approach is highly flexible and was successfully applied for concentrating SDS-protein complexes from high ionic strength buffer and for the extraction of DNA from blood. This simple approach to integrated sample treatment provides a new opportunity for the field of personalized medicine through TDM and diagnostic devices.

The optimisation of microfluidic structures for specific purposes often involves a range of changes in layout. When fast concept-to-chip time is a priority, one-step manufacturing techniques are favoured over conventional methods.[3] For advanced fluidic functionality and/or when the footprint of the device are important, three dimensional (3D) structures are gaining interest. Conventional lithography-based processes, however, typically avoid 3D designs as this significantly increases the cost and complexity of the manufacturing process. The ability to transform digital designs directly into physical models, without the need for masks, will not only speed up the fabrication process, it will also make practical evaluation of different designs faster and easier. 3D manufacturing techniques can be subtractive through removal of material or additive through fused deposition modelling (FDM),[4] or photo-fabrication.[5] Additive methods in particular have developed rapidly over the past decade and there are now a number of different approaches and materials available to the consumers and professional markets.[6] I employed a low cost desktop 3D-pinter to fabricate micro- to millifluidic devices with different functionalities for different applications.

PROJECT AIMS

- Create nanojunctions with defined permeability ranges using the controlled dielectric breakdown of poly(dimethylsiloxane) (PDMS).
- Demonstrate the use of the nanojunctions for selective electrokinetic transport including the extraction of small molecules from complex matrices like whole blood.
- Simultaneous extraction, concentration, and desalting of small molecules from blood using electrokinetic SMTs.

- Explore the potential of the developed nanojunctions for biopolymer applications.
- Demonstrate the use of an entry-level 3D-printing for the fabrication of microfluidic devices with integrated functionalities.

References

1. Manz, A.; Graber, N.; Widmer, H. M., Miniaturized total chemical analysis systems: A novel concept for chemical sensing. *Sensors and Actuators B: Chemical* **1990,** *1* (1–6), 244-248.
2. (a) Sönksen, P. H.; Judd, S. L.; Lowy, C., Home monitoring of blood-glucose: Method for improving diabetic control. *The Lancet* **1978,** *311* (8067), 729-732; (b) Walford, S.; Gale, E. A. M.; Allison, S. P.; Tattersall, R. B., Self-monitoring of blood-glucose: Improvement of diabetic control. *The Lancet* **1978,** *311* (8067), 732-735.
3. Waldbaur, A.; Rapp, H.; Lange, K.; Rapp, B. E., Let there be chip-towards rapid prototyping of microfluidic devices: one-step manufacturing processes. *Analytical Methods* **2011,** *3* (12), 2681-2716.
4. (a) McDonald, J. C.; Chabinyc, M. L.; Metallo, S. J.; Anderson, J. R.; Stroock, A. D.; Whitesides, G. M., Prototyping of microfluidic devices in poly(dimethylsiloxane) using solid-object printing. *Analytical Chemistry* **2002,** *74* (7), 1537-1545; (b) Moore, J.; McCuiston, A.; Mittendorf, I.; Ottway, R.; Johnson, R. D., Behavior of capillary valves in centrifugal microfluidic devices prepared by three-dimensional printing. *Microfluid Nanofluid* **2011,** *10* (4), 877-888; (c) Symes, M. D.; Kitson, P. J.; Yan, J.; Richmond, C. J.; Cooper, G. J. T.; Bowman, R. W.; Vilbrandt, T.; Cronin, L., Integrated 3D-printed reactionware for chemical synthesis and analysis. *Nature Chemistry* **2012,** *4* (5), 349-354; (d) Kitson, P. J.; Rosnes, M. H.; Sans, V.; Dragone, V.; Cronin, L., Configurable 3D-printed millifluidic and microfluidic 'lab on a chip' reactionware devices. *Lab on a Chip* **2012,** *12* (18), 3267-3271.

5. (a) Hull, C. W. Apparatus for production of three-dimensional objects by stereolithography. U.S. Patent 4,575,330, March 11, 1986; (b) Ikuta, K.; Hirowatari, K. In *Real three dimensional micro fabrication using stereo lithography and metal molding*, Micro Electro Mechanical Systems, 1993, MEMS '93, Proceedings An Investigation of Micro Structures, Sensors, Actuators, Machines and Systems. IEEE., 7-10 Feb 1993; 1993; pp 42-47.
6. (a) Levy, G. N.; Schindel, R.; Kruth, J. P., Rapid manufacturing and rapid tooling with layer manufacturing (LM) technologies, state of the art and future perspectives. *CIRP Annals - Manufacturing Technology* **2003,** *52* (2), 589-609; (b) Vaezi, M.; Seitz, H.; Yang, S., A review on 3D micro-additive manufacturing technologies. *International Journal of Advanced Manufacturing Technology* **2012**, 1-34.

TABLE OF CONTENT

TABLE OF FIGURES

Chapter One

Nanofluidics for Point-of-care Devices

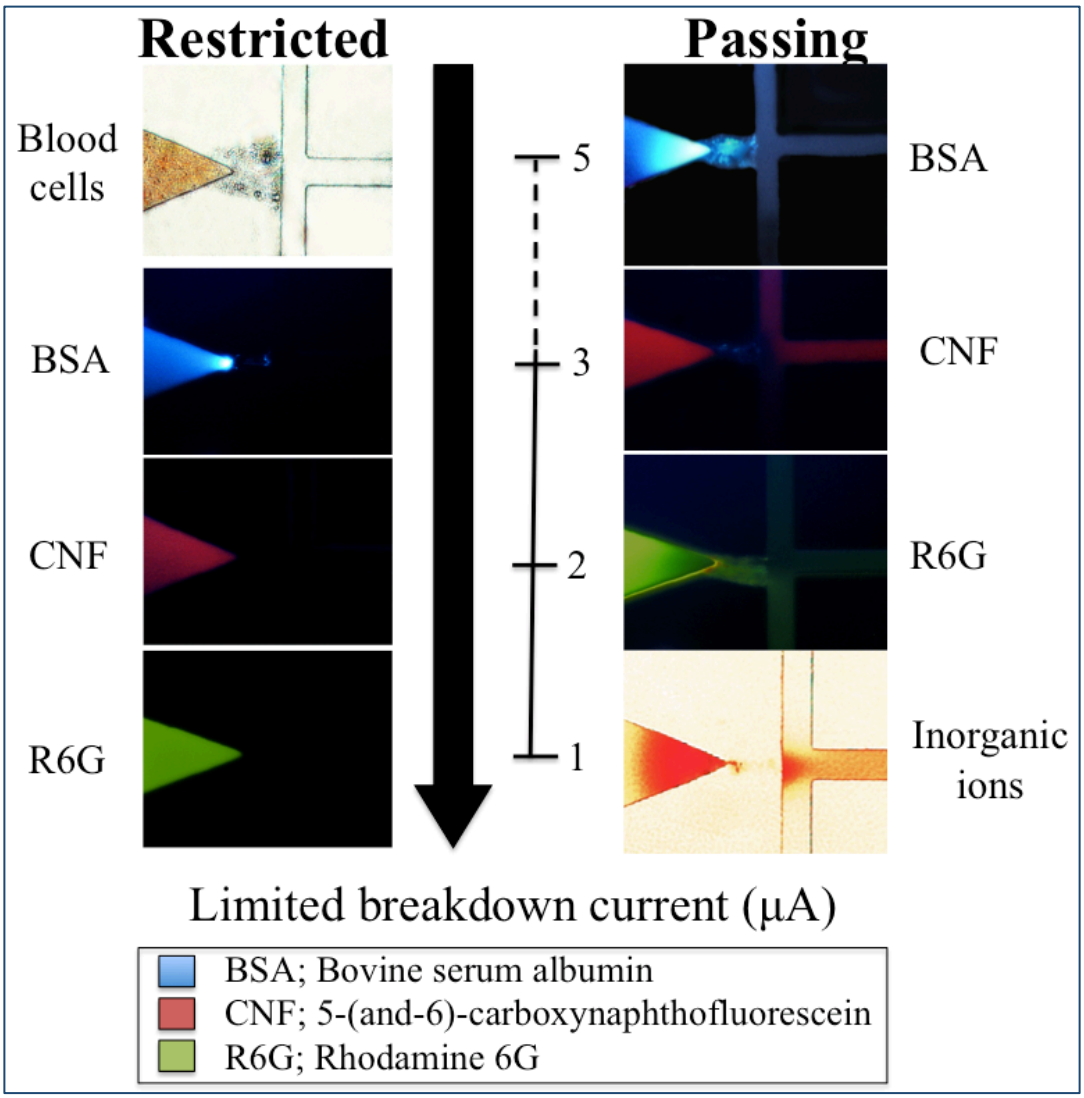

1 Nanofluidics for Point-of-care (POC) Devices

1.1 Introduction to nanofluidics

Natural systems rely on nanofluidics to perform efficiently at the lowest energy cost possible. The dream to imitate these systems and study them in a controlled environment became possible when advances in microelectronics opened the way to fabricate nanostructures. As a result, nanofluidics emerged as a fast growing field to describe the astonishing fluid behaviour in confined nanometre geometry where at least one dimension is smaller than 100 nm. Contrary to microscale structures, molecular size and electric double layer (EDL) thickness can no longer be neglected and the surface properties have more profound effects leading to unique physical and transport phenomena.[1] Models that apply to microfluidics fail to predict or describe nanofluidic behaviour and new laws govern the mass transport and fluid flow. Furthermore, nanojunctions and interfaces integrated within a microfluidic system produce new effects that enable multiple processes to be performed more efficiently, faster and at lower cost. There is a lot to be understood and unveiled about nanofluidic behaviour and it will continue to inspire researchers for years to come.

1.1.1 Nanometric Length Scales

For most nanofluidic applications, the bulk Navier–Stokes (NS) equations can be safely used to account for the fluid transport down to pore size of 1 nm.[2] In order to understand the forces that control ion transport in nanochannels, the nature of different length scales and the interactions within them need to be explained first. The different lengths are presented in Figure 1.1

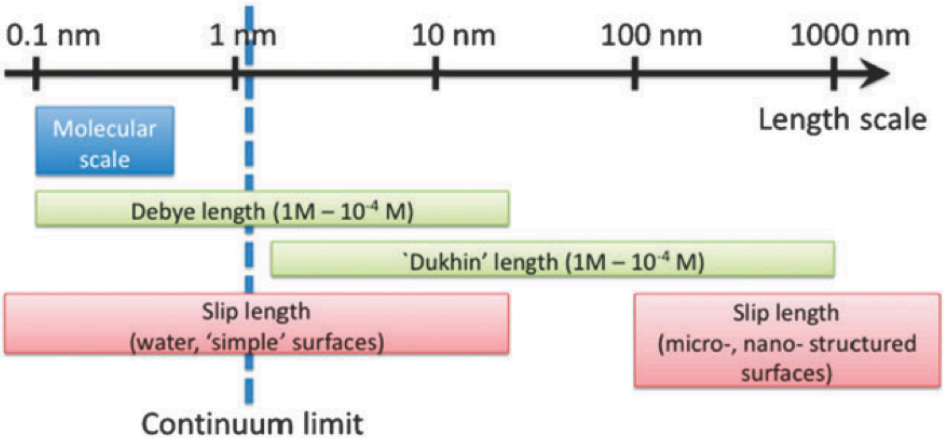

Figure 1.1 Various length scales at play in nanofluidics. Reproduced Ref [2] with permission of The Royal Society of Chemistry.

1.1.1.1 Bjerrum Length (ℓ_B)

Bjerrum length (ℓ_B) is the distance at which the electrostatic interaction V_{el} between two charged species becomes comparable to the thermal energy (k_BT), as defined in Equation 1-1 where k_B is the Boltzman constant and T is the absolute temperature in Kelvin.[2]

$$\mathcal{V}_{el}\,(\ell_B) \approx k_BT \qquad \text{Equation 1-1}$$

which can be also be written for an ion in a dielectric medium at certain temperature as;

$$\ell_B = \frac{Z^2e^2}{4\pi\varepsilon k_BT} \qquad \text{Equation 1-2}$$

For a univalent ion (Z = 1) in water at ambient temperature, ℓ_B = 0.7 nm which is common to biological systems but not yet achievable by current nanofabrication techniques. However, Equation 1-2 suggests that larger ℓ_B can

be observed for multivalent ions in a medium with low dielectric constant (ε) like organic solvents, where *e* is the elementary charge.

1.1.1.2 Debye Length Scale

When a solution comes into contact with a charged surface, an EDL forms (Figure 1.2).[3] The Stern layer closer to the solid surface consists of counter ions, cations in case of negatively charged surfaces, and can be considered as immobile. This layer is held strongly by electrostatic interactions to neutralize the surface and counter ion concentration is higher than in the bulk solution. The second layer, the diffuse layer, contains co-ions and counter-ions. The higher concentration of counter ions in the Stern layer compared to the adjacent diffuse layer leads to the evolution of the zeta potential (ζ) at the shear plane. The ion distribution between the EDL and bulk solution is described by the famous Boltzmann distribution equation;

$$c_i = C_o \, exp\left(-z_i \, \frac{F\varphi}{RT}\right) \qquad \text{Equation 1-3}$$

Where (c_i) is the ionic concentration in the EDL and (C_o) is the bulk ion concentration.

The screening length of the EDL, the Debye length (λ_D), represents the local balance between the electromigration towards the surface and diffusion away from it[4] and can be defined based on the Poisson-Boltzmann theory in terms of the bulk ionic strength (ρ_s).

$$\lambda_D = \frac{1}{\sqrt{8\pi\ell_B\rho_s}} \qquad \text{Equation 1-4}$$

From Equation 1-4 it is clear that higher ionic strength solutions, regardless of the surface charge density, will result in a more compact EDL with narrow λ_D, which

is the case when handling most biological samples (λ_D = 1 nm for an aqueous solution of a monovalent symmetric electrolyte ρ_s = 0.1 M). At very low ionic strength buffers, the λ_D may reach few tens of nanometers (λ_D = 30 nm for ρ_s = 10^{-4} M).

The EDL plays a major role in ion transport through nanochannels under an applied electric field, as it is the region where volume electric forces (f_e) take place. The magnitude of these forces is defined by the charge density (ρ_e) and the applied electric field (E_e).

$$f_e = \rho_e E_e \qquad \text{Equation 1-5}$$

The Poisson-Boltzmann equation quantify the local ionic concentration ratio between the electroneutral bulk and a location inside the EDL at a certain potential relative to the bulk as described in the following equations

$$f_e = \rho_e E_e \qquad \text{Equation 1-6}$$

$$f_e = \rho_e E_e \qquad \text{Equation 1-7}$$

In nanochannels, this leads to interesting transport behaviour especially when the nanochannel dimensions approach twice the Debye length and EDL overlap occurs. Examples include permselectivity of the nanochannels and formation of ion enrichment and depletion zones.

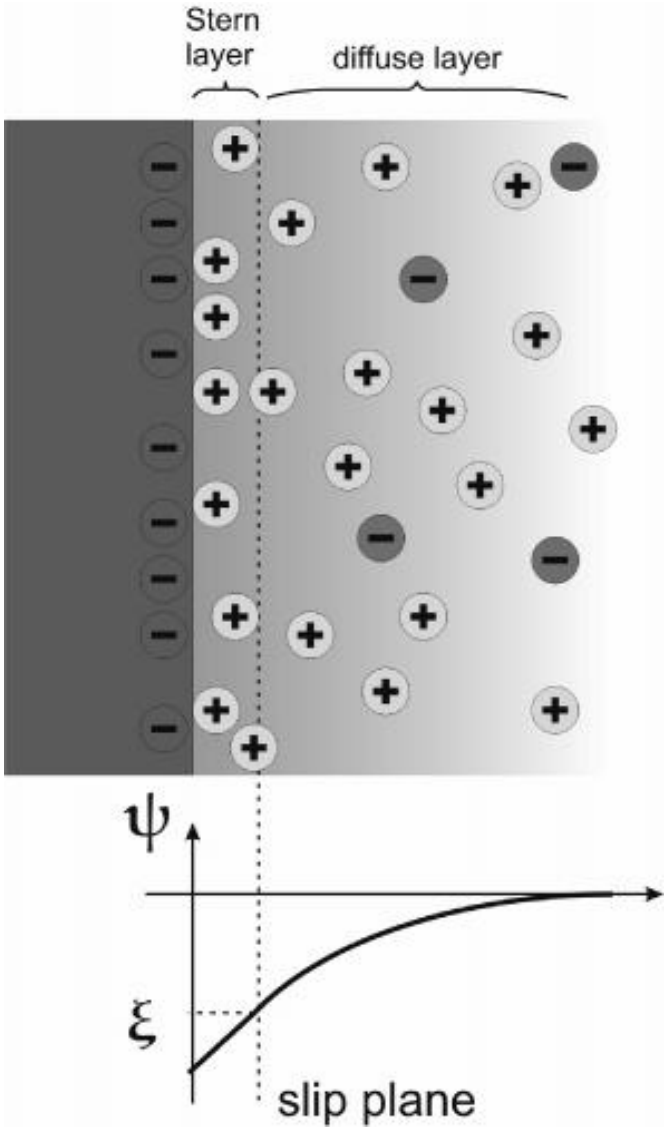

Figure 1.2 Schematic model of the electrical double layer at a solid/ liquid interface. ψ is the electrical potential. A surface with negative charges is considered. These charges are shielded by the Stern layer and the diffuse layer. The Stern layer is formed by adsorbed immobile ions. The mobile diffuse layer is located outside the shear plane. The zeta potential ζ is at the shear plane. The Stern layer and the diffuse layer form the electrical double layer. "Reprinted with permission from Abgrall, P.; Nguyen, N. T., Nanofluidic Devices and Their Applications. *Analytical Chemistry* **2008,** *80* (7), 2326-2341. Copyright (2008) American Chemical Society."

1.1.1.3 Dukhin Length (ℓ_{Du}) and Dukhin Number (Du)

The excess counter ion near the solid surface of the nanochannel leads to surface conductivity different from the bulk conductivity inside the nanochannel determined by the bulk ion concentration (C_o). The Dukhin length is defined as the surface to bulk conductivity ratio

$$\boldsymbol{\ell_{Du}} = \frac{\kappa_s}{\kappa_b} \qquad \text{Equation 1-8}$$

Accordingly, for a nanochannel height (h), the Dukhin number (Du), a dimensionless term, is defined as

$$Du = \frac{\kappa_s}{h\kappa_b} = \frac{\boldsymbol{\ell_{Du}}}{h} \qquad \text{Equation 1-9}$$

Large values (>1) indicate higher nanochannel ion selectivity due to surface dominated ion transport even in the absence of EDL overlap.[5] While both the Dukhin length and the Debye length increase with decreasing the ionic strength, the Dukhin number takes into account the nanochannel dimensions and the entrance effects under non-equilibrium conditions. When the EDL almost overlap, the Dukhin number becomes very large extending outside the nanochanel and consequently defines the electric field lines at the nanochannel entrance. Dukhin numbers can be used to predict the kind of ion concentration polarization (ICP), propagating or non-propagating, and the extent of micromixing near nano-/microchannel junctions.

Values for ℓ_{Du} can vary from 0.5 nm for C_o = 1 M to 5 μm for $C_o = 10^{-4}$ M, for a surface charge density $e\Sigma \approx 50$ mC/m^2 (≈ 0.3 e/nm^2). The surface charge for glass is at most in the 10 mC/m^2 range (≈ 0.06 e/nm^2). Increasing the surface charge density will result in larger ℓ_{Du}, which explains the enhanced conductance and ion transport through more highly charged hydrogel nanojunctions.

1.1.1.4 Slip Lengths (b) and Surface Friction

Navier length or slip length (b) describes the friction of the fluid at the interface and affect ion transport at charged surfaces. Slip length for water strongly depends on wettability and shows higher values for hydrophobic surfaces than hydrophilic ones which are negative and located at the plane of shear, few tens of nanometres as compared to sub-nanometre.[6] Interestingly, lengths in the micrometre range can be observed at nano-/micro-interfaces and enhanced fluid transport occurs when the pore size approaches b.

1.1.2 Electro-osmotic Flow (EOF) and Electrophoresis

As described before under section 1.1.1.2 Debye Length Scale, the EDL for negatively charged surfaces comprises a dense layer of counter ions, cations. Under the influence of an applied electric field, cations near the solid surface will migrate towards the cathode while dragging water molecules creating a normal or cathodic EOF. In contrast to microchannels, the profile of EOF in nanochannels is no longer flat as the geometry approaches the λ_D.[7] The direction of the EOF is determined by the type of the surface charge, positive or negative, but its magnitude is the net result of many factors.

Hydrophobic surfaces exhibit low liquid-solid friction with high slip length (b) values. The large slippage results in high EOF velocity (μ_{EO}) by amplifying the surface zeta potential (ζ) which inturn is related to the electrostatic surface potential (ψ_o). This relation can be described by the following equations, where ϵ the dielectric constant and η the fluid viscosity,[6]

$$\mu_{EO} = \frac{\epsilon\zeta}{\eta} \qquad \text{Equation 1-10}$$

$$\zeta = \psi_{\mathrm{o}}\left(1 + \frac{b}{\lambda_D}\right) \qquad \text{Equation 1-11}$$

Equation 1-11 explains why hydrophobic surfaces may show much higher zeta potential (ζ) than hydrophilic surfaces with similar surface electrostatic potential ψ_{o}.

1.1.3 Ion Permselectivity and Ion Concentration Polarization (ICP)

Nanochannels connecting two microchannels (also called nanojunction), with EDL overlap will develop a Donnan potential (V_D) at the pore entrance and exit due to co-ion exclusion. The magnitude of V_D is quantified by the ratio ℓ_{Du}/h and the following equation.

$$V_D = \frac{k_B T}{2e}\log\left[\frac{\rho_-}{\rho_+}\right] \qquad \text{Equation 1-12}$$

where ρ_- and ρ_+ are the negative and positive ion concentrations, respectively.

The nanochannel will have a uniform V_D if the two microchannels are at equilibrium with the same electric potential and salt concentration. If an electric field is applied across the nanochannel (ΔV) or a salt concentration difference exists across the nanojunction ($\Delta\rho_s$), an ion flux will develop.

Nanochannels with charged surfaces do not simply act as a mechanical filter. The cation concentration in nanochannels with negatively charged surfaces is higher than in the bulk concentration as they participate in the EDL to neutralize the surface while anions are excluded by repulsion, resulting in a lower concentration than that in the bulk, as described by the Boltzmann distribution equation (Equation 1-3). Under an applied electric field, cations will be favourably transported through the

nanochannel at a higher rate than diffusion such that a depletion zone develops at the anodic side and an enrichment zone at the cathodic side of the nanochannel (Figure 1.3). Also, anions are excluded from entering the nanochannel and will accumulate at the cathodic side but are depleted on the anodic side to preserve electroneutrality.[8]

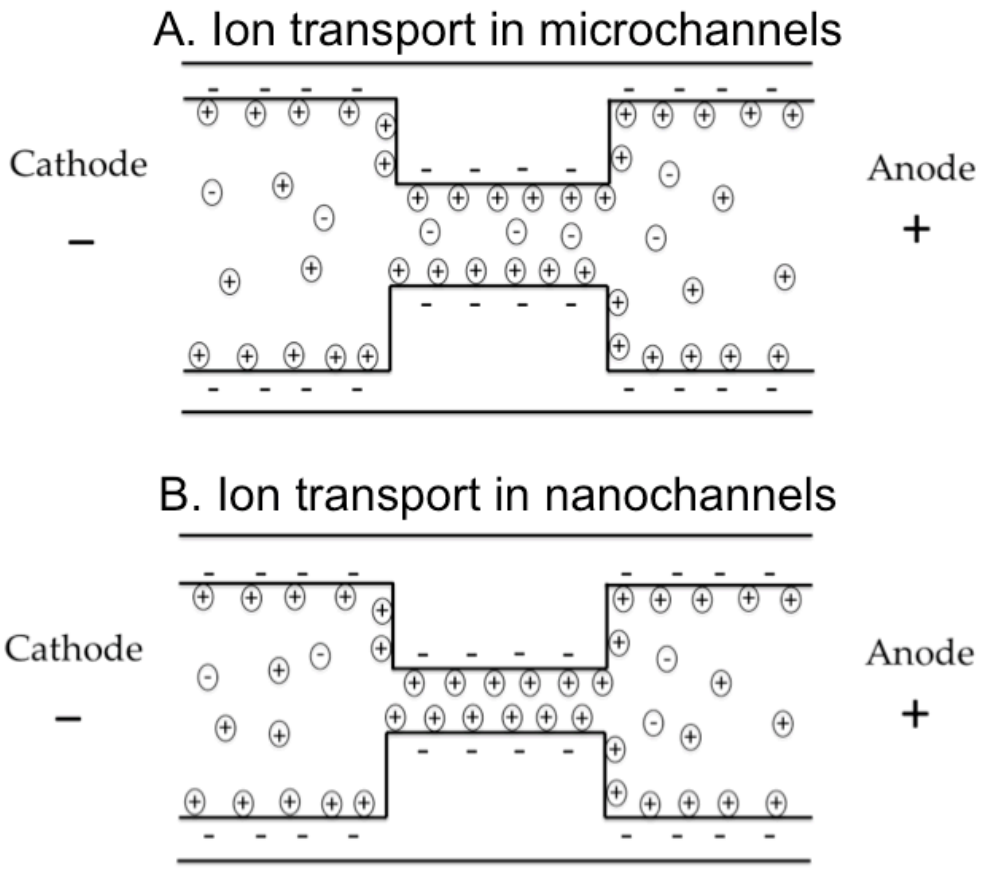

Figure 1.3 Schematic explaining the difference between ion transport in microchannels and in nanochannels with EDL overlap. The permselectivity of the nanochannels results in the development of ICP.

Current-voltage curves for nanochannels with EDL overlap comprise three distinct regions. First, an Ohmic regime in which the current increases linearly with the applied voltage. Second, the current saturates and does not increase at the same rate beyond a certain value, the limiting current. This stage marks the onset of ICP. Depletion zones at the anodic side of the nanojunction are extremely low in ion concentration, i.e. there are very few free ions to carry the current. This stage does not continue beyond a certain point as EOF imbalance at the depletion zone boundary creates vortices and fast mixing. The third regime is characterized by a sudden increase in current, the over-limiting current, as the fast mixing suddenly delivers ions into the depletion zones.[9]

Due to the small pore size of nanochannels, the size contribution of small ions can no longer be neglected especially when the hydrated ion radius is considered.[5a] As mentioned before, the Debye length (λ_D) reflects a local balance between the electromigration of counter ions towards the surface and their diffusion away from the surface. While EDL effects on ion transport can be neglected in microchannels, they play a major role in ion transport in nanochannels. Ion interaction with the EDL is complicated by the variable viscosity and permittivity within the EDL. The non-uniform transverse electric fields within the nanochannels leads to a transverse concentration gradient that can be defined by an analyte-specific length scale (λ_S) that is a function of the ion valence number, λ_D, ζ and temperature.[4] Consequently, ion transport is a function of EDL thickness, surface charge density, ion valence and of course its electrophoretic mobility.[10] Moreover, at low electrokinetic radius ($h/\lambda_D < 4$) and high surface to volume ratio, electrophoretic separations may turn into chromatographic separations due to intensified adsorption effects even for weakly adsorbing analytes with low adsorption rates of 10^{-4} s.[11]

1.1.4 Conductivity: Surface versus Bulk

Conductance (*K*) is the relationship between electric current versus electric potential drop. An increase in conductance indicates a high concentration of free moving ions. Bulk *K* is directly proportional to the solution ionic strength (ρ_s). Charged surfaces provide supplementary contribution to conductance. As described before under 1.1.1.3 Dukhin Length ($\boldsymbol{\ell_{Du}}$) and Dukhin number (D_u), the ratio between the surface and bulk conductance is ℓ_{Du}. Surface conductance will dominate for nanochannels smaller than ℓ_{Du}. High surface charge density leads to higher conductance and increased counter ion flux. This effect is also observed in glass devices at high pH for the same reason.[5b]

1.2 Dielectric Breakdown for creating nanojunctions

Dielectric breakdown is one of the easiest methods for seamless integration of nanojunctions into a microfluidic device because only the micron-sized channels need to be patterned and bonded, overcoming the difficulty associated with making microfluidic chips with nanochannels. Typically, the chip design includes a 10-100 μm wide structure separating two microchannels filled with electrolyte solution. Thermal and mechanical failure of this structure by applying high voltage that exceeds the dielectric strength introduces nanojunctions that connect the two microchannels leading to increased ion transport and measured current. Before the breakdown, no current can be detected and a sharp increase in current can be observed when the connection between the two microchannels is established. The resistance of the nanojunction is a function of its pore size, length, electrolyte ionic strength and applied electric field. Consequently, a larger pore size results in a higher current if all other variables are kept constant.

Dielectric breakdown has been reported for integrating nanojunctions into microfluidic devices using different materials such as PDMS,[12] glass,[13] toner[14] and solid-state insulating membranes.[15] Reported applications include selective reagent dispensing,[12a] protein preconcentration[12b-d] and solution mixing,[12e] but none of these reported control of the breakdown process to obtain control of the nanojunctions transport properties. Shortly after the publication of the work described in this thesis, nanopores with sub-nm precision were reported for DNA sequencing by another group using thin insulating membranes of silicone nitride.[15]

In the following sections, two configurations using the controlled dielectric breakdown of PDMS are presented for the creation of a single nanojunction device, followed by a dual nanojunction device. The single nanojunction device was used to

demonstrate control over the dielectric breakdown process, limiting the pore size using the current throughout the breakdown process. This device was applied for the extraction of drugs and small molecular weight biomarkers from blood and for the concentration of large biomolecules like SDS-protein complexes from high ionic strength buffers. The dual nanojunction device was used to introduce a SMT for the simultaneous extraction, concentration and desalting of analytes within specific size/mobility range, directly from blood. This approach was applied for small molecules and short ssDNA.

1.2.1 Single Dielectric Breakdown

1.2.1.1 Microfluidic Device

The microfluidic device is hybrid PDMS/glass with the design shown in Figure 1.4. The PDMS layer formed the top containing the microfluidic structures and was sealed to a glass slide that formed the floor of the channels. All microchannels were 30 μm deep. All separation channels were 50 μm wide while the V-channels were 500 μm wide. The tip of each V-channel was separated from the separation channel by a 100 μm gap. This distance was chosen instead of the reported distances of 20 μm[12b] or 40 μm[12c] to allow for prolonged use of higher voltages during extraction without the risk of secondary breakdowns. Extending the gap length also enabled the formation of smaller pores. However, as this increases, breakdown becomes more difficult; requires longer time and higher applied voltage. The V-shaped design helped to focus the electric field at the tip and result in single point breakdown. Distance from the intersection point to reservoirs (B) and (SW) was 12.5 mm while that to reservoir (BW) was 47.5 mm. Detection point was 40.0 mm from the intersection.

Cured PDMS and soda glass slide were plasma treated with handheld corona discharge device[16] (model BD-20, 230 V power supply, Electro Technic Products) for 15 s and placed in conformal contact for 12 h at 65^{o}C for irreversible bonding. In reversibly bound devices, the applied voltage caused the PDMS to lift off the glass surface, forming gaps that continued to widen over time. Moreover, permeability was greatly affected by PDMS fabrication conditions like degassing of the prepolymer mixture and curing temperature as it affects the surface roughness of PDMS. Using irreversibly bound devices prevented this problem and improved the reproducibility of the method. Air plasma treatment oxidizes the PDMS creating a silica-like surface stiffer than the native PDMS. Mills *et al*.[17] reported that 4 min exposure will result in a stiff layer that is 200 ± 40 nm thick and predicted the thickness to be proportional to the square root of exposure time. Devices made with exposure time of 1 min showed different results from those treated for 15 s. As the stiff silica-like layer is expected to have a different dielectric strength from that of PDMS, it is important to keep the plasma treatment conditions constant to obtain a constant stiff layer thickness.

Figure 1.4 Schematic diagram of the microfluidic design (dimensions not to scale) showing the V-channel and the separation channels (left) and profilometric image of the PerMX template used for rapid prototyping (right). Each reservoir is 20 μL capacity; Sample (S), Buffer (B), Sample Waste (SW) and Buffer Waste (BW).

1.2.1.2 Dielectric Breakdown Conditions

All microchannels were filled with the breakdown electrolyte; 1 or 10 mM disodium hydrogen phosphate ($Na_2HPO_4.2H_2O$). The applied breakdown electric field used in this work 2200 V (22 V/μm) is just above the dielectric strength of PDMS (21 V/μm). Before the formation of the nanojunctions, no current can be detected when applying a high voltage just above the dielectric strength of the PDMS gap.

Preliminary breakdown experiments were performed using 5-(and-6)-carboxynaphthofluorescein (CFN) solution in the sample compartment and recording the process with a charge coupled device (CCD) camera. Once the breakdown occurred, as indicated by sudden increase in current and observation of spark formation through the microscope, the power supply was manually switched off. The formed channels were able to restrict most of the labelled proteins. The breakdown electrolyte in this experiment was 10 mM phosphate solution because using a 1 mM solution, it was difficult to detect the onset of the breakdown as the increase in current was less sharp.

To achieve better control and repeatability, the high voltage supply was controlled using a simple Labview 8.6 program (National Instruments, Austin, TX, USA) adjusted the voltage output by monitoring the return current and kept the current at the threshold defined by the user. Once the desired current was reached the applied voltage was reduced, preventing further breakdown of the material. This approach allowed for the formation of a specific pore size, and enhanced the reproducibility as compared to other breakdown methods relying on the time and potential difference. It was also found that operating at an electric field strength just above the dielectric breakdown allows better control because the rise in current is slower than with higher electric fields, providing time to adjust the applied potential

difference without causing pore widening. Another advantage using the proposed conditions is that no bubble formation was observed which usually happens during uncontrolled breakdown.

1.2.1.3 Permeability Studies

The relationship between nanojunction permeability and current limit was investigated through a series of breakdown experiments using analytes of different hydrodynamic size and charge, like small inorganic ions (effective hydrated radii of about 0.3 nm), small organic molecules (0.3-0.5 nm), aromatic compounds (0.5-1.0 nm) and labelled proteins (2-4 nm).[5a]

The determination of the exact pore size of the nanojunction was not practical for a number of reasons. The pores are enclosed within the PDMS structure preventing the use of scanning electron microscope. Calculation of the width using current-voltage data requires a known and homogenous pore width. This is not possible because the breakdown process results in the formation of a bundle of pores with varying diameter along their length. Hence, the average size is best estimated based on their permeability to different sized analytes; a mixture of CNF dye (anionic) and fluorescamine-labelled bovine serum albumin (BSA). The effective hydrodynamic radii of CNF and BSA are about 1 and 4 nm, respectively.[5a]

After formation of the nanojunctions, the main channels were filled with 10 mM phosphate, pH 9, to which 0.1% hydroxypropylmethyl cellulose (HPMC) was added to suppress the EOF. The viscosity range for HPMC used is 2,600-5,600 cP, 2% in water at 20^{o}C. A voltage of 400 V was applied between reservoirs (S) and (SW) in Figure 1.4 to drive electrophoretic transport. At least 5 devices were tested for each current limit.

All solutions were prepared in Milli-Q water obtained from a Millipore (North Ryde, Australia) purification system. CNF from Molecular Probes (Oregon, USA) was prepared in 10 mM phosphate solution (pH 11.7) to obtain 200 μg/mL solution.

BSA was labelled with fluorescamine by mixing 200 μL of 250 μg/mL in 10 mM phosphate and 0.9% (w/v) NaCl, with 20 μL of 10 mM fluorescamine in acetone. BSA and fluorescamine were obtained from Sigma-Aldrich (Steinheim, Germany) and NaCl from Merck (Darmstadt, Germany). The BGE was 10 mM disodium hydrogen phosphate solution (pH 9.0) with 0.1% (w/v) HPMC from Sigma-Aldrich (Steinheim, Germany) to suppress EOF.

Simultaneous transport of inorganic ions was done using 0.1 g/mL solutions of iron (III) nitrate ($Fe(NO_3)_3.9H_2O$) from ChemSupply (Beverley, S.A., Australia) and potassium thiocyanate (KSCN) from Ajax chemicals (Sydney, Australia) in 100 mM nitric acid (HNO_3) from Merck (VIC, Australia).

Images and video footage of the permeability studies were recorded using a Nikon high-definition colour CCD camera head (Digital Sight DS-Fi1c, Nikon, Japan) and operated with NIS-Elements BR 3.10 software (Melville, NY, USA) mounted on an inverted fluorescence microscope (Ti-U, Nikon, Tokyo, Japan). Multiband pass excitation (λ_{ex} at 390, 482, 563 and 640 nm) and emission (λ_{em} at 446, 523, 600 and 677 nm) filters (Semrock, Rochester, NY, USA) were used for all experiments.

An in-house 4-channel (0-5 kV) dc power supply was used to apply an electrical potential to each reservoir through a custom-designed interface connected to 5 platinum electrodes. Platinum electrodes connected to a single V-channel shared the same output and hence provided the same voltage.

1.2.1.4 Results and Discussion

Under the experimental conditions, the PDMS surface is negatively charged. Different current limits were used to produce the nanojunctions and their permeability was evaluated experimentally. The results are summarised in Figure 1.5.

For a current limit of 10 μA using 10 mM buffer, the pores permitted a hydrodynamic flow from the sample V-channel into the separation channel. This suggests the formed channels may be up to a few μm in diameter because nanojunctions with pore size up to 200 nm will prevent hydrodynamic flow.[18]

When 5 μA was set as the current limit (Figure 1.5 top row), the resulting nanojunctions prevented red blood cells (6-8 μm in size) from entering the separation channel, while allowing electrophoretic transport of fluorescamine-labelled BSA.

Decreasing the current limit to 3 μA (Figure 1.5 second row), allowed the transport of anionic CNF, but not BSA. The transport of BSA (hydrodynamic radius ~4 nm) was restricted due to its size while CNF and R6G (~1 nm) passed through the nanojunctions regardless of their charge. However, when the EOF was not suppressed by HPMC in the separation channel, CNF could not be transported from the sample chamber into the separation channel, while the cationic dye R6G still passed through the nanojunction indicating the contribution of EOF towards the permeability of the nanojunction.

For nanojunctions formed with a current limit of 2 μA (Figure 1.5 third row), CNF was restricted while the cationic dye R6G passed. As discussed before, nanojunction selectivity to enhance transport of counter ions and exclude co-ions does not require EDL overlap and is related to the Dukhin number. In this case the EDL is not completely overlapped as indicated by the current measured through the

nanojunction, but the free space available for transport is smaller than the hydrodynamic radius of CNF, thus preventing its transport. R6G has a similar size to CNF, but due to its positive charge, it can participate in the EDL and be transported through the nanojunction.

Finally, using a current threshold of 1 μA (Figure 1.5 bottom row), the nanojunction prevented transport of BSA, CNF and R6G, yet was still able to transport small ions, iron (III) and thiocyanate. The formation of the red iron (III) thiocyanate complex on both sides of the nanojunctions indicates the simultaneous transport of both ions under suppressed EOF conditions, using 0.1 M HNO_3 as BGE and 400 V applied across the nanojunctions, reservoirs (S) and (SW). As this nanojunction was still able to transport small cations and anions (~0.3 nm), it indicates a smaller pore size in the nanojunction but not complete EDL overlap. In the case of R6G, it is not clear whether R6G was excluded based on the size or if the strong adsorption to the nanochannel walls rendered them positive and therefore selectively excluding cations. A characteristic voltage-current curve would help identify if the exclusion was size or ICP related. However, this procedure requires measuring very low currents, in the range of nA, which is not feasible using the instruments available in our laboratory.

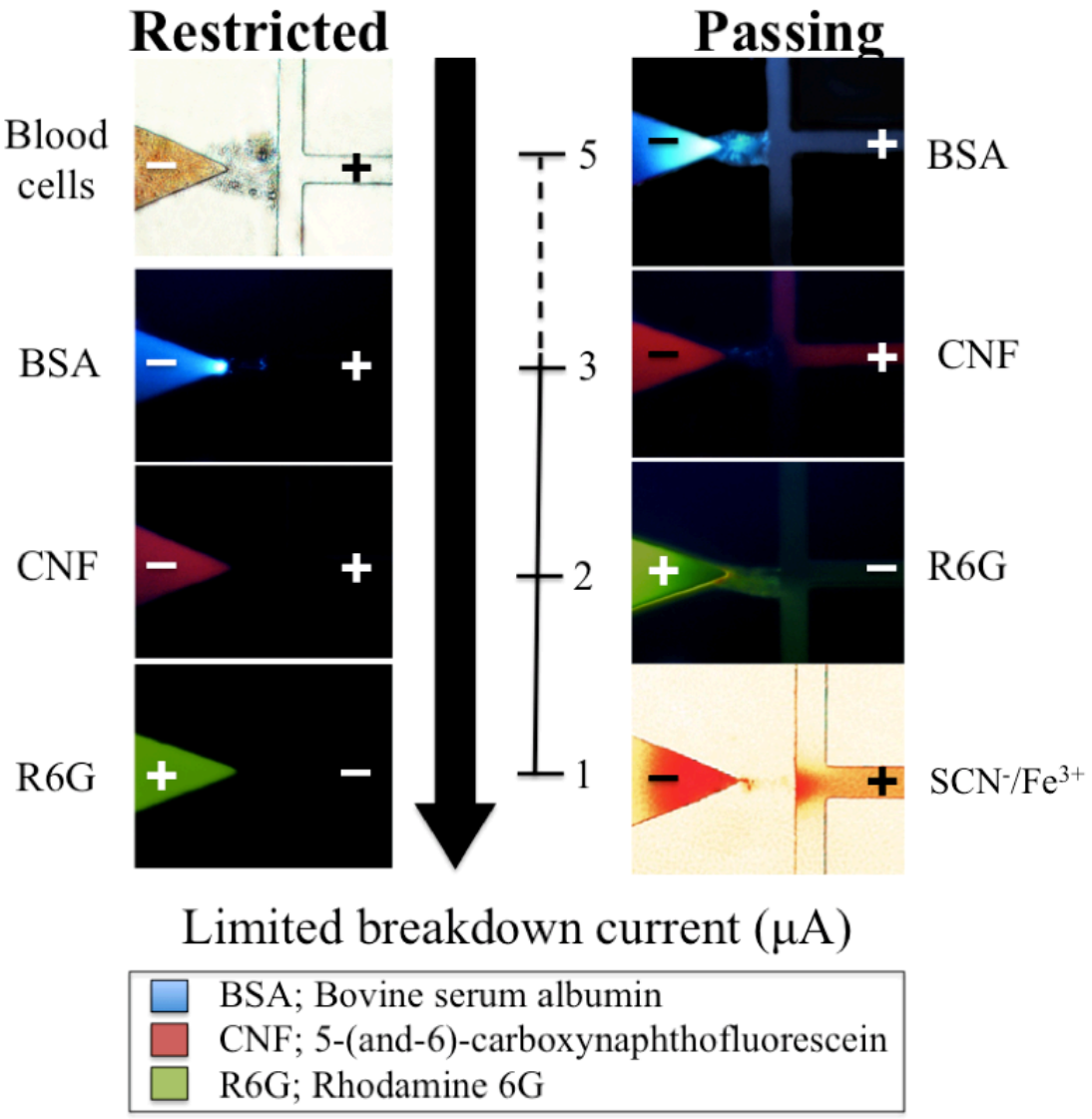

Figure 1.5 Screen shots from the movies recorded by the CCD camera of the fluorescence microscope showing the permeability of nanochannels created with decreasing current limits for red blood cells, labelled BSA (blue), CNF (red), R6G (green) and the inorganic ions, iron (III) and thiocyanate. Images on the left show blocked transport while those on the right show permeability.

As can be seen from the screen shots in Figure 1.5, the nanochannels in the nanojunction were formed as a bundle of irregular interconnected structure also known as ‘‘Lichtenberg’’ structure. The shape resembles a lightening, which is the dielectric breakdown of air.

1.2.2 Double Dielectric Breakdown

1.2.2.1 Microfluidic Device

The microfluidic device is hybrid PDMS/glass with the design shown in Figure 1.6. All microchannels were 30 μm deep. The separation channel was 50 μm wide while the V-channels were 500 μm wide. The tip of each V-channel was separated from the separation channel by a 100 μm gap and offset from each other by 500 μm. This offset distance allowed the two nanojunctions to communicate and form the size/mobility trap (SMT). The total length of the separation channel was 60 mm and the effective length from the injection point (first nanojunction) to the detection point was 40.0 mm.

The device was fabricated and irreversibly bound using the same procedure described under 1.2.1 Single Dielectric Breakdown (section 1.2.1.1 Microfluidic Device).

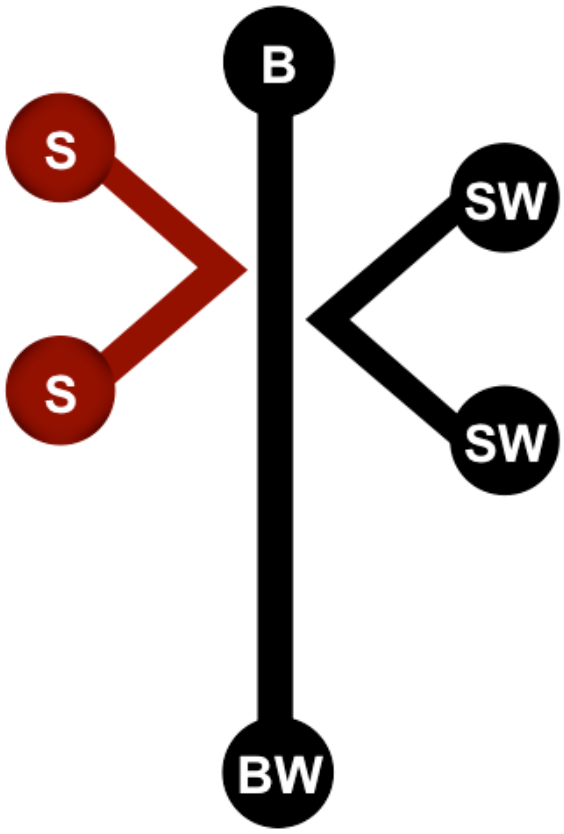

Figure 1.6 Schematic diagram of the microfluidic design (dimensions not to scale) showing the two V-channels and the main separation channel. All channels were 30 μm deep. Each reservoir is 20 μL capacity; Sample (S), Buffer (B), Sample Waste (SW) and Buffer Waste (BW).

1.2.2.2 Dielectric Breakdown Conditions

Just before use, all channels were filled with the breakdown electrolyte; 10 mM phosphate buffer, pH 11. The extraction nanojunction was formed by applying a breakdown voltage of 2200 V to the sample V-channel (S) while keeping the separation channel grounded and setting the current limit to 5 μA using an in-house regulated power supply. To form the concentration nanojunction, the electrode was placed in the waste V-channel (SW) and the current limit was set to 0.5 μA. The channels were then cleaned and refilled with the experimental solutions. For the first use after the breakdown, reversed polarity was applied through the extraction nanojunction at 1000 V till a current of 5 μA was reached then the proper voltage for the experiment was set. The current limits were selected to trap small molecular weight negatively charged organic molecules (200-1000 Da) and short ssDNA.

The breakdown voltage was supplied from a 2-channel power supply (0-3 kV) with a built-in current feedback made in the UTAS Central Science Laboratory Workshop. The voltage was terminated once the current limit was reached.

1.2.2.3 Extraction and Concentration Enhancement Studies

After nanojunction formation, the buffer was replaced by sample in the sample V-channel and the separation channel was filled with 100 mM phosphate buffer, pH 11.5, and 0.5% HPMC (unless stated otherwise) whilst the waste V-channel was filled with 10 mM phosphate buffer, pH 11.5.

The ion depletion/enrichment zones were visualized by tracking anionic fluorescent dyes added in the sample V-channel. All the flow motions and ion transport images were obtained using an inverted fluorescence microscope integrated with high-definition colour CCD camera as described before under 1.2.1 Single

Dielectric Breakdown (section 1.2.1.3 Permeability Studies). Quantitative measurements were performed using a photomultiplier tube (PMT) (Hamamatsu Photonics KK, Hamamatsu, Japan) connected to the microscope. Data acquisition was made using an Agilent interface (35900E) connected to a laptop and operated by Agilent ChemStation for LC software (Agilent Technologies, Waldbronn, Germany). Multiband emission and excitation filters were used. An in-house 4-channel (0-5 kV) dc power supply was used to apply an electrical potential to each reservoir through a custom-designed interface connected to 6 platinum electrodes. Platinum electrodes connected to a single V-channel shared the same voltage channel and hence provided the same voltage.

1.2.2.4 Results and discussion

The SMT is based on preferential electrokinetic transport of ions through nanochannels (Figure 1.7). The extraction nanojunction permits the transport of small ions (< 1000 Da) through the free transport region not occupied by the EDL whilst blocking the transport of cells and plasma proteins. The high ionic strength on both sides of the extraction nanojunction, the use of HPMC to shield the surface charge and the relatively large pore size delay the development of ICP and hence extend the injection for small anions. Fluorescein is negatively charged at this pH, co-ion to the negatively charged surface, and its transport through the extraction nanojunction into the separation channel indicates little or no EDL overlap in this junction (Figure 1.8). The applied voltage for injection was kept longer after the transport has stopped to sharpen the concentrated analyte zone because the developing depletion zone from the concentration nanojunction will prevent the collected analyte from moving beyond that point.

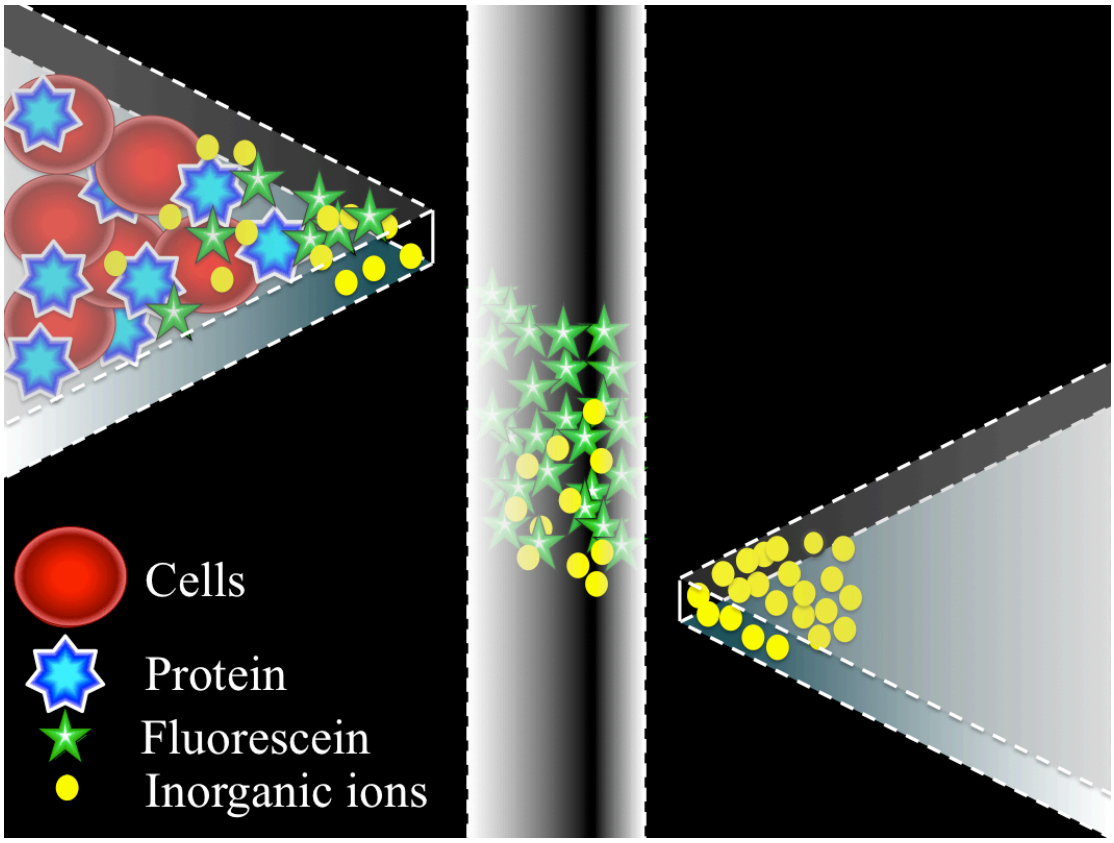

Figure 1.7 The concept of electrokinetic SMTs. Nanojunctions were formed by controlled PDMS dielectric breakdown of the 100-μm wide barriers between the tip of the V-channels and the separation channel under preset current limit. The extraction nanojunction (left) has larger pore size than the desalting nanojunction (right). Current limits were chosen to achieve pore size that enables trapping of small molecules like fluorescein.

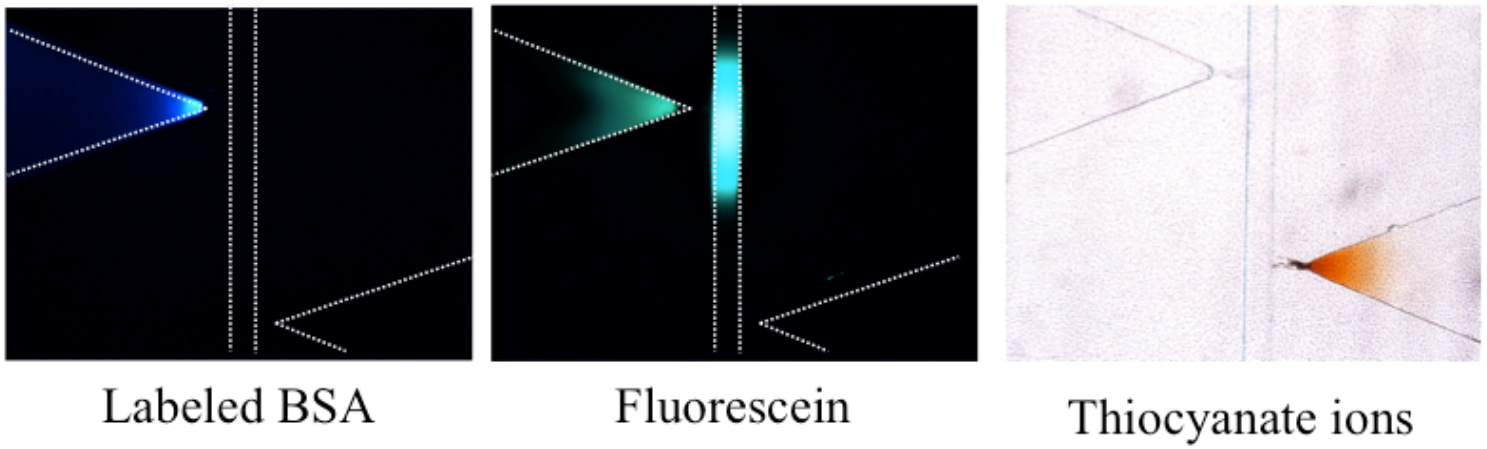

Figure 1.8 Screen shots showing selective extraction and trapping of small molecules (fluorescein) while labelled protein was filtered out and small ions (thiocyanate) passed from one side to the other as indicated by the formation of red coloured complex with iron (III). Current limit was set at 5 μA for the left side and 0.5 μA for the right side. BGE in the middle channel is 100 mM phosphate buffer, pH 11.5, with 0.25% HPMC to suppress the EOF while 10 mM phosphate buffer, pH 11.5, was used in the right V-channel without HPMC. Applied voltage was set at -200, -500, -300, and +500 V for reservoirs B, S, BW and SW, respectively.

The concentration nanojunction between the waste V-channel and the separation channel was created with a 0.5 μA current limit selected to block the transport of target analytes, modelled by fluorescein (332 Da), but allow the transport of small inorganic ions in order to desalt the sample. A lower ionic strength, 10 mM phosphate buffer, pH 11.5, was used to allow the application of higher voltages without the risk of secondary breakdown. The EOF in the waste V-channel was not suppressed as it was beneficial to prevent the small molecular weight anions from passing through the nanochannels until the ICP is developed. Together the extraction and concentration nanojunctions create the SMT in which molecules with a defined size/mobility range can be extracted, concentrated, and desalted.

Figure 1.8 shows the efficacy of the SMTs using molecules of different molecular weights. In the first panel, negatively charged BSA (MW ~66.5 kDa) labelled with fluorescamine concentrates at the tip of the sample V-channel because its size exceeds that of the free transport region within the extraction nanojunction. The second panel shows the trapping of fluorescein, a small anion similar to many pharmaceuticals, in the separation channel. The injected plug is trapped between the two nanojunctions. The third panel illustrates the transport of a small inorganic anion, thiocyanate, which migrates from the sample V-channel, through the extraction nanojunction into the separation channel, then through the concentration nanojunction into the waste V-channel filled with iron (III) where it forms a red complex, establishing the directional transport of the thiocyanate ions. Whilst migration of iron into the sample V-channel is also expected, the red colour was not observed in the sample V-channel due to the high pH in this channel, which prevents the complex formation. Together the data from these 3 panels illustrate the ability of the trap to

selectively concentrate and desalt small organic molecules from both larger and smaller ions.

The matrix ionic strength and viscosity were found to affect the amount of transported ions (Figure 1.9). As the ionic strength and viscosity of the sample increases, ion transport quickly decreases. The Nernst-Planck equation describes the direct relation between the ion transport through the channel and the electric potential gradient.

$$J(x) = -D\frac{\partial C(x)}{\partial x} - \frac{zF}{RT}DC\frac{\partial \varphi(x)}{\partial x} + Cv_{eo}(x) \quad \text{Equation 1-13}$$

where D, z, and C are the diffusion coefficient, charge of the permeation species, and concentration, respectively. $\frac{\partial C(x)}{\partial x}$ is the concentration gradient at distance x, $\frac{\partial \varphi(x)}{\partial x}$ is the potential gradient and v_{eo} is the electroosmotic velocity. The three terms on the right-hand side of Equation 1-13 represent the contributions of diffusion, electromigration and EOF, respectively.

The increased viscosity decreases the ion mobility and consequently lowers the junction conductivity, which can be observed as decreased transport. But a different effect of the viscosity modifier, HPMC, was observed when it was used in the separation channel to suppress the bulk EOF. A concentrated fluorescein zone was only formed when the EOF in the separation channel was suppressed using 0.25% or more of HPMC.

Increasing the ionic strength of the BGE in the separation channel resulted in corresponding increase in the fluorescein amount extracted. In the waste V-channel, a lower ionic strength of 10 mM was used to allow the application of high voltage during extraction for up to 200 s without significantly changing the junction pore size.

The extent of the EOF through the concentration junction was controlled by its pore size without using an EOF suppressor. If the pore size is larger than the optimum, strong EOF will disturb the extracted zone. Without having the concentrating junction, the extracted analyte zone will continue to diffuse and broaden along the separation channel without effective concentration. Using the SMTs, 100-fold enhancement factor of fluorescent dyes was achieved compared to standard pinched injection in a conventional cross-channel with the same width and depth and using the same applied voltages. Experiments using a mixture of fluorescein and eosin showed that these dyes do not interfere with each other and separation can be achieved without compromising the efficiency (peak width) of the separation. This is illustrated in Figure 1.10, with the comparison of the electropherograms obtained following a conventional pinched injection and the SMT injection.

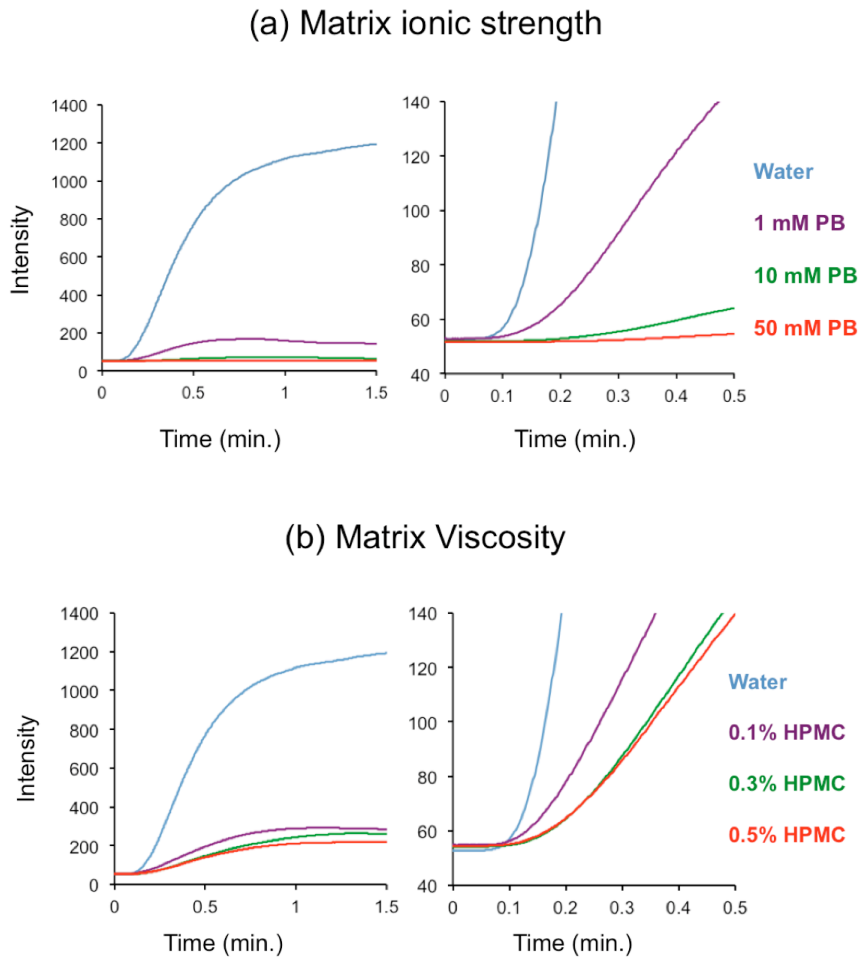

Figure 1.9 Evolution of the enrichment fluorescein zones at the anodic side of the extraction nanojunction as a function of injection time. Panels on the left traces the enrichment till steady state while panels on the right only focus on the early stages of enrichment. (a) Effect of matrix ionic strength (0, 1, 10, and 50 mM phosphate buffer, pH 11.5). (b) Effect of matrix viscosity (0, 0.1, 0.3, and 0.5% HPMC). The viscosity range for HPMC used is 2,600-5,600 cP, 2% in water at 20^{o}C. Boltzmann Unless stated otherwise, the sample was 0.2 ppm fluorescein in water with no HPMC and the BGE had a concentration of 10 mM phosphate buffer, pH 11.5 with 0.5% HPMC. Electric potential of -100, -500, -100, and +300 V were applied to reservoirs B, S, BW and SW, respectively.

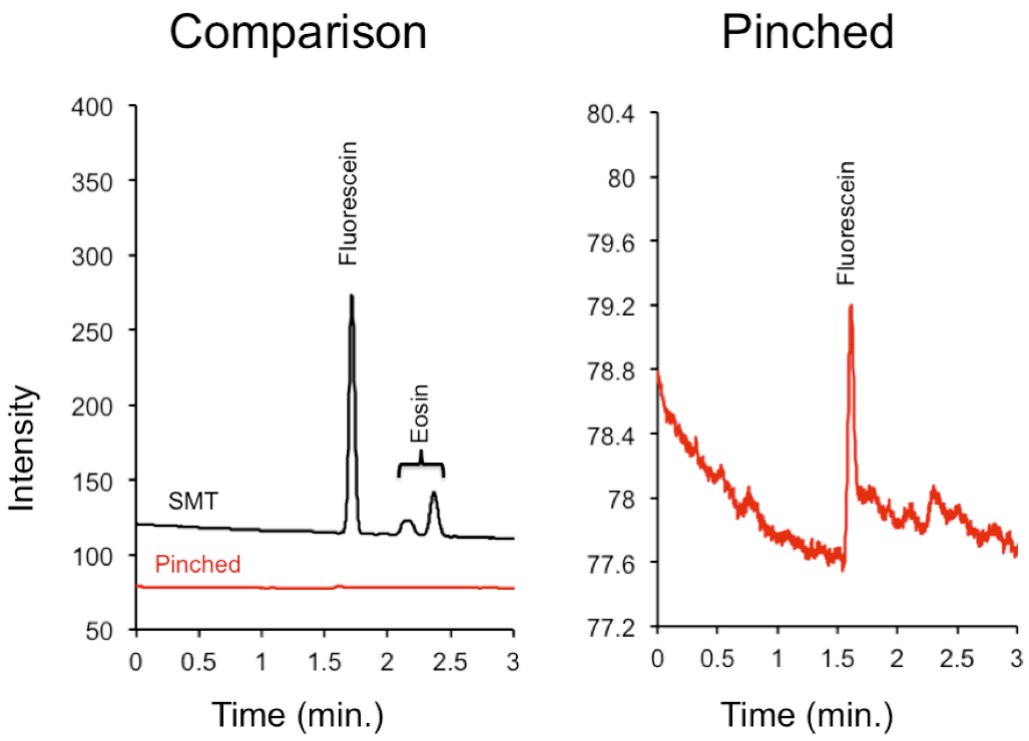

Figure 1.10 Electropherograms comparing SMT (black trace) with pinched injection (red trace and magnified right image) under the same conditions of 0.05 ppm fluorescein and eosin in water. The signal for fluorescein was enhanced by 100-fold. The BGE in the separation channel was 100 mM phosphate buffer, pH 11.5, with 0.5% HPMC and in the waste V-channel was 10 mM phosphate buffer, pH 11.5. Applied voltages for SMT were -100, -300, -100, and +500 V for 60 s and for separation was -200, +100, +1500, and +100 V at reservoirs B, S, BW and SW, respectively. For pinched injection, all channels were filled with 100 mM phosphate buffer, pH 11.5, with 0.5% HPMC. Applied voltage for injection was -60, -240, -100, and +400 V at B, S, BW and SW reservoirs, respectively, and separation voltage was the same as that of the SMT.

1.3 Conclusions

Control of the dielectric breakdown of PDMS was achieved by limiting the current during the breakdown process. This enabled tuning of the nanojunction pore size and hence their permeability for molecules of different molecular weights. The breakdown can be conducted up to 2 months after the chip fabrication without compromising assay results. This elegant approach does not require instrumentation other than the HV supplies also used for electrophoretic separations, and can be tuned to accommodate target analytes ranging from macromolecules to small molecule pharmaceuticals. Experimental data shows adequate control over permeability. This presents a low cost, easy and potentially a commercially viable method for nanojunction formation immediately prior to sample analysis as further discussed in Chapters 3 and 5.

1.4 References

1. (a) Schoch, R. B.; Han, J.; Renaud, P., Transport phenomena in nanofluidics. *Reviews of Modern Physics* **2008,** *80* (3), 839-883; (b) Stein, D.; Kruithof, M.; Dekker, C., Surface-charge-governed ion transport in nanofluidic channels. *Physical Review Letters* **2004,** *93* (3), 035901.
2. Bocquet, L.; Charlaix, E., Nanofluidics, from bulk to interfaces. *Chemical Society Reviews* **2010,** *39* (3), 1073-1095.
3. Abgrall, P.; Nguyen, N. T., Nanofluidic devices and their applications. *Analytical Chemistry* **2008,** *80* (7), 2326-2341.
4. Baldessari, F.; Santiago, J. G., Electrophoresis in nanochannels: brief review and speculation. *Journal of Nanobiotechnology* **2006,** *4* (12), doi:10.1186/1477-3155-4-12.
5. (a) Cervera, J.; Ramírez, P.; Manzanares, J.; Mafé, S., Incorporating ionic size in the transport equations for charged nanopores. *Microfluid Nanofluid* **2010,** *9* (1), 41-53; (b) Chang, C.-C.; Yeh, C.-P.; Yang, R.-J., Ion concentration polarization near microchannel–nanochannel interfaces: Effect of pH value. *Electrophoresis* **2012,** *33* (5), 758-764.
6. Bouzigues, C. I.; Tabeling, P.; Bocquet, L., Nanofluidics in the Debye layer at hydrophilic and hydrophobic surfaces. *Physical Review Letters* **2008,** *101* (11), 114503.
7. Pennathur, S.; Santiago, J. G., Electrokinetic transport in nanochannels. 1. Theory. *Analytical Chemistry* **2005,** *77* (21), 6772-6781.
8. Plecis, A.; Schoch, R. B.; Renaud, P., Ionic transport phenomena in nanofluidics: Experimental and theoretical study of the exclusion-enrichment effect on a chip. *Nano Letters* **2005,** *5* (6), 1147-1155.

9. (a) Kim, S. J.; Wang, Y.-C.; Lee, J. H.; Jang, H.; Han, J., Concentration polarization and nonlinear electrokinetic flow near a nanofluidic channel. *Physical Review Letters* **2007,** *99* (4), 044501; (b) Yossifon, G.; Mushenheim, P.; Chang, Y.-C.; Chang, H.-C., Nonlinear current-voltage characteristics of nanochannels. *Physical Review E* **2009,** *79* (4), 046305.

10. Pennathur, S.; Santiago, J. G., Electrokinetic transport in nanochannels. 2. Experiments. *Analytical Chemistry* **2005,** *77* (21), 6782-6789.

11. Garcia, A. L.; Ista, L. K.; Petsev, D. N.; O'Brien, M. J.; Bisong, P.; Mammoli, A. A.; Brueck, S. R. J.; Lopez, G. P., Electrokinetic molecular separation in nanoscale fluidic channels. *Lab on a Chip* **2005,** *5* (11), 1271-1276.

12. (a) McDonald, J. C.; Metallo, S. J.; Whitesides, G. M., Fabrication of a configurable, single-use microfluidic device. *Analytical Chemistry* **2001,** *73* (23), 5645-5650; (b) Kim, S. M.; Burns, M. A.; Hasselbrink, E. F., Electrokinetic protein preconcentration using a simple glass/poly(dimethylsiloxane) microfluidic chip. *Analytical Chemistry* **2006,** *78* (14), 4779-4785; (c) Lee, J. H.; Chung, S.; Kim, S. J.; Han, J., Poly(dimethylsiloxane)-based protein preconcentration using a nanogap generated by junction gap breakdown. *Analytical Chemistry* **2007,** *79* (17), 6868-6873; (d) Anwar, K.; Han, T.; Yu, S.; Kim, S., Integrated micro/nano-fluidic system for mixing and preconcentration of dissolved proteins. *Microchim Acta* **2011,** *173* (3-4), 331-335; (e) Yu, S.; Jeon, T.-J.; Kim, S. M., Active micromixer using electrokinetic effects in the micro/nanochannel junction. *Chemical Engineering Journal* **2012,** *197* (0), 289-294.

13. (a) Guijt, R. M.; Lichtenberg, J.; de Rooij, N. F.; Verpoorte, E.; Baltussen, E.; van Dedem, G. W. K., Indirect electro-osmotic pumping. *Journal of the Association for Laboratory Automation* **2002,** *7* (3), 62-64; (b) Mao, X.; Reschke,

B. R.; Timperman, A. T., Analyte transport past a nanofluidic intermediate electrode junction in a microfluidic device. *Electrophoresis* **2010,** *31* (15), 2686-2694.

14. Yu, H.; Lu, Y.; Zhou, Y.-g.; Wang, F.-b.; He, F.-y.; Xia, X.-h., A simple, disposable microfluidic device for rapid protein concentration and purificationvia direct-printing. *Lab on a Chip* **2008,** *8* (9), 1496-1501.

15. Kwok, H.; Briggs, K.; Tabard-Cossa, V., Nanopore Fabrication by Controlled Dielectric Breakdown. *PLOS one* **2014,** *9* (3), e92880.

16. Haubert, K.; Drier, T.; Beebe, D., PDMS bonding by means of a portable, low-cost corona system. *Lab on a Chip* **2006,** *6* (12), 1548-1549.

17. Mills, K. L.; Huh, D.; Takayama, S.; Thouless, M. D. In *Adjustable nanofluidic channels by tunnel cracking of a constrained brittle layer*, ASME 2008 6th International Conference on Nanochannels, Microchannels, and Minichannels, Darmstadt, Germany, June 23–25; Darmstadt, Germany, 2008; pp 1597-1602.

18. Kuo, T.-C.; Cannon Jr, D. M.; Shannon, M. A.; Bohn, P. W.; Sweedler, J. V., Hybrid three-dimensional nanofluidic/microfluidic devices using molecular gates. *Sensors and Actuators A: Physical* **2003,** *102* (3), 223-233.

This chapter has been removed for copyright or proprietary reasons.

Shallan, A. I.; Guijt, R. M.; Breadmore, M. C., Chapter 4. Microfluidic devices for the analysis of drugs and their metabolites in biological fluids in “Microfluidics, Nanotechnology and Disease Biomarkers for Personalized Medicine Applications”, NOVA Science Publishers, Shiddiky, M. J. A.; Wee, E. J. H.; Rauf, S.; Trau, M., (ed), United States, pp. 73-98. ISBN 978-1628080209 (2013).

3 Analysis of Small Molecules in Biological Samples - Nanojunctions

The methods described in this chapter demonstrate the use of controlled dielectric breakdown as an affordable alternative for fabricating defined nanochannels. Three examples are presented.

The first example, based on single electric breakdown, combines the extraction, separation and detection of the antimalarial drug quinine sulphate in blood, as a model for positively charged drugs. Analysis of quinine in blood was published in; **Shallan, A. I.; Gaudry, A. J.; Guijt, R. M.; Breadmore, M. C., Tuneable nanochannel formation for sample-in/answer-out devices. *Chemical Communications* 2013, 49 (27), 2816-2818.**

The second example, also based on single electric breakdown, integrates the extraction of small organic acids from blood with ITP and indirect fluorescence detection.

The third example employs SMTs for seamless extraction, concentration, desalting and separation of ampicillin in blood, as a model for negatively charged drug. Analysis of ampicillin in blood was published in; **Shallan, A. I.; Guijt, R. M.; Breadmore, M. C., Electrokinetic size and mobility traps for on-site therapeutic drug monitoring. *Angewandte Chemie International Edition* 2015, 54, 7359-7362. DOI: 10.1002/anie.201501794.**

3.1.1 Extraction and Analysis of Quinine in Blood

Quinine monitoring is essential to understand the epidemiology of *Falciparum malaria* and differentiate between lack of response due to inadequate dosing or drug

resistance.[1] Conventional analytical methods like HPLC offer high sensitivity and high resolution between the parent drug and its metabolites and commercial impurities but the sample pre-treatment is complex and lengthy (~30 min) and the separation itself takes 20 min employing high percentage of acetonitrile (58%) in the mobile phase.[2] Facilities in which malaria patients are hospitalized often lack sophisticated equipment and the transport of samples to a central laboratory may take too long for results to become available.

3.1.1.1 Microfluidic Device and Nanojunction Formation

The microfluidic device is a hybrid PDMS/glass with the single nanojunction design previously described in Chapter One. All microchannels were 30 μm deep.

All microchannels were filled with 1 mM disodium hydrogen phosphate ($Na_2HPO_4.2H_2O$) from Sigma-Aldrich (Steinheim, Germany) then an electric field was applied across the 100 μm PDMS barrier between the sample V-channel and the separation channel using a power supply controlled by Labview 8.6 program. The PDMS breakdown was done at 2200 V while setting the current limit at 3.0 μA.

3.1.1.2 Extraction and Analysis

After the nanojunction was formed, the breakdown buffer was replaced with the sample and the ITP electrolytes then injection and separation voltages were applied sequentially as indicated in Figure 3.1.

Quinine solutions: Quinine sulphate monohydrate (from Aldrich, Milwaukee, USA) was used to prepare 100 mg/mL stock solution in 3 mM sulphuric acid. This solution was used to spike blood samples to obtain 1 mg/mL. Different concentrations (0.5, 1.0, 2.5, 10.0, and 25.0 μg/mL) were obtained by serial dilution with whole blood. Whole blood samples from a healthy volunteer were treated with disodium salt

of ethylene diamine tetraacetic acid (EDTA) to prevent coagulation and divided into small volumes (200 μL) then stored in the freezer at -4^{o}C.

ITP electrolytes: The ITP system is similar to that reported by Mikus *et al.*[3] with LE of 10 mM sodium acetate (BDH, VIC, Australia), 20 mM acetic acid, 1 mM NaH_2PO_4, (pH 4.3) in presence of 0.1% (w/v) HPMC and terminating electrolyte (TE) of 10 mM β-alanine (Sigma-Aldrich, Steinheim, Germany) and 10 mM acetic acid (pH 4.2).

Applied electric field: An in-house, 4-channel power supply (0-5 kV) was used to apply electric field to the microfluidic device through 5 platinum electrodes. The 2 electrodes connected to reservoirs (S) share the same applied voltage. Electrokinetic extraction of quinine was done from whole blood for 100 s. After extraction, the high voltage was switched to perform peak mode ITP in the main channel, with the quinine peak passing the detector at 90 s.

Detection: Experiments were visually recorded with a high-definition colour CCD camera head mounted on an inverted fluorescence microscope. Quantitative measurements were done using a PMT. More details can be found in Chapter One and in the Appendix under Detection.

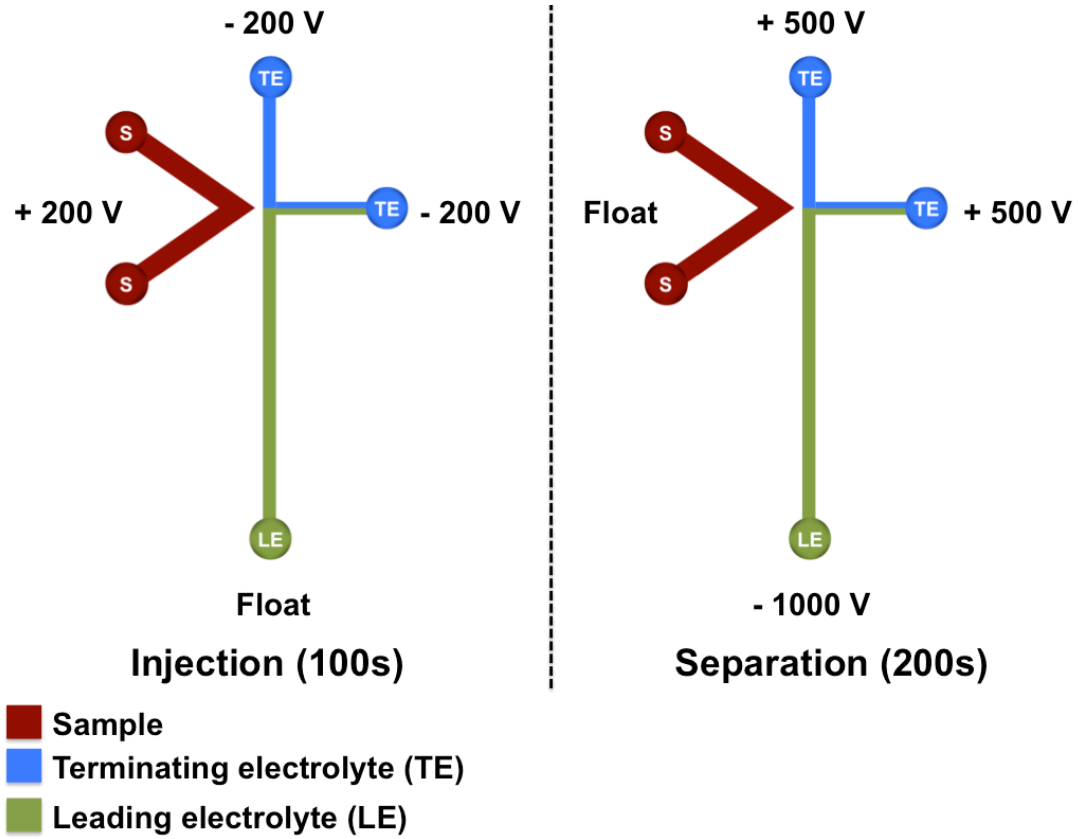

Figure 3.1 Experimental conditions for quinine analysis. Injection voltage was applied for 100 s to extract quinine from blood then the voltage was switched to perform peak mode ITP with fluorescence detection. The LE was 10 mM sodium acetate, 20 mM acetic acid, 1 mM NaH_2PO_4, (pH 4.3) in presence of 0.1% (w/v) HPMC. The TE was 10 mM β-alanine and 10 mM acetic acid (pH 4.2).

3.1.1.3 Results and Discussion

The nanojunction, fabricated with PDMS dielectric breakdown at 3 μA current limit, permits the transport of quinine (Mwt 324 Da) but excludes blood cells and plasma proteins. Quinine, positively charged at physiological pH, can be transported through the nanojunction because its hydrodynamic size is smaller than the physical size of the pores irrespective to EDL thickness. The nanojunction's preferential transport of cations and the cathodic EOF mean that a large amount of quinine can be transported across the junction. An advantage of the electrokinetic extraction of quinine is that chloride was not injected under the applied voltage settings of the experiment, eliminating a known quencher for quinine fluorescence.[4] The natively fluorescent R-phycoerythrin (at pH < pI) was used to confirm that the formed nanochannels would also block positively charged proteins, which indicates that the physical size of the pores is smaller than the hydrodynamic size of this model protein.

The ITP system used selectively concentrates quinine between a high mobility LE and a low mobility TE,[3] eliminating interferences based on size and mobility. Using ITP, the quinine was doubled in comparison with that in the sample chamber.

The linear range was 0.5-25 μg/mL (Figure 3.3 and Figure 3.2) with a regression coefficient (R^2) of 0.999 and a relative standard deviation (RSD%) between different devices of 15 (n = 5), extending beyond the recommended therapeutic range of 5-10 μg/mL.[5] This is one of the few non-immunoassay microdevices with sample-in/answer-out for drugs in blood.

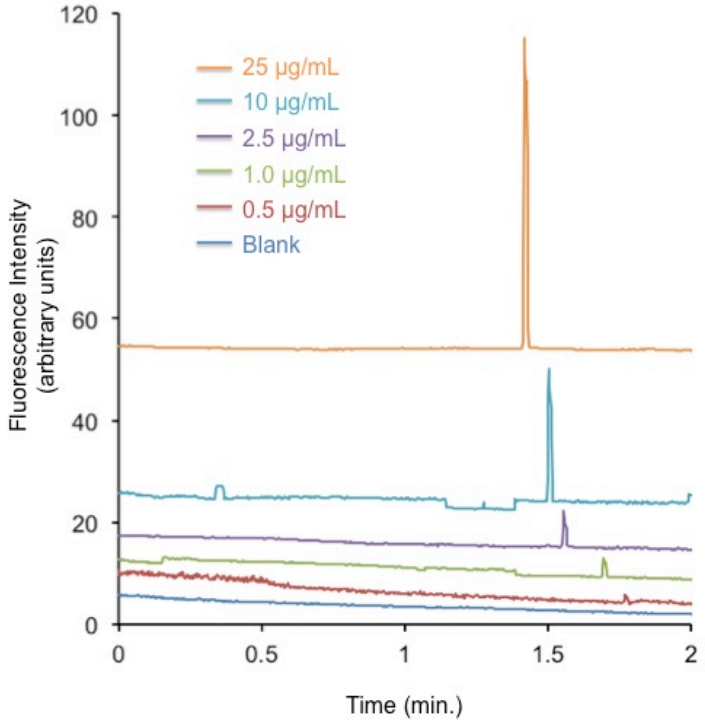

Figure 3.2 Isotachopherograms for blood sample spiked with 0, 1.0, 2.5, 10 and 25 µg/mL quinine sulphate. ITP conditions were LE of 10 mM sodium acetate, 20 mM acetic acid, 1 mM NaH_2PO_4 (pH 4.3), and 0.1% (w/v) HPMC and TE of 10 mM β-alanine and 10 mM acetic acid (pH 4.2). Injection and separation times were 100 and 90 s, respectively.[3]

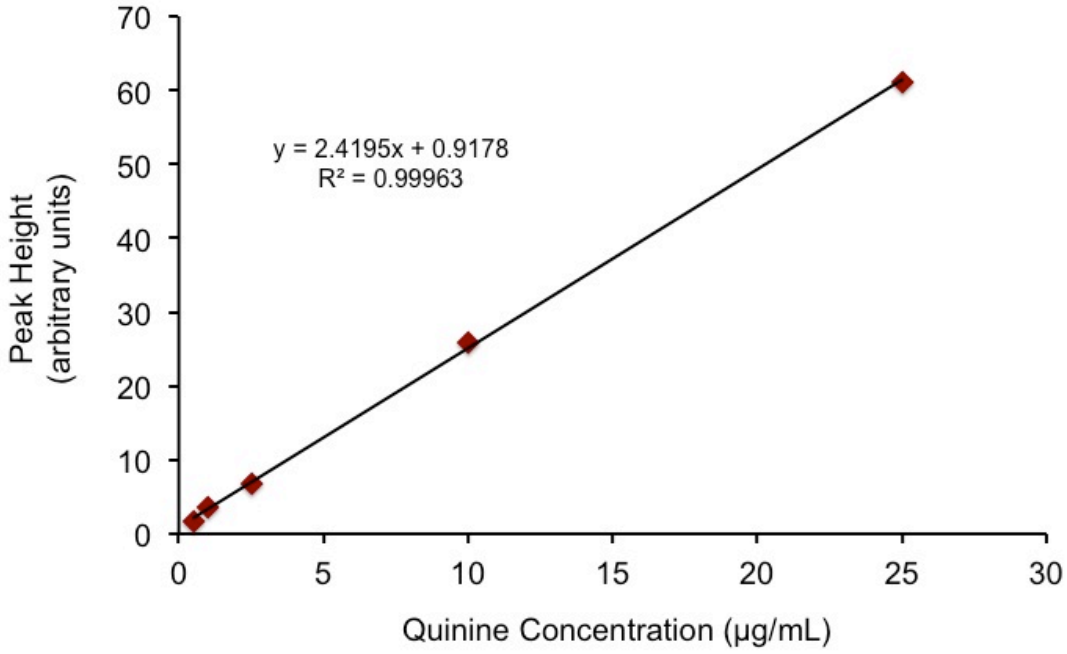

Figure 3.3 Linear calibration curve 0.5-25 µg/mL for quinine in blood.

3.1.2 Extraction and Analysis of Small Organic Acids in Blood

Quick and accurate diagnosis in emergencies may save lives, as management of each case requires different actions. Increased blood or saliva levels of small molecular weight biomarkers, such as organic acids, are indicative of metabolic disorders that may require patient admission to the intensive care unit (ICU). Monitoring the levels of these biomarkers while treating the cause, can be used to obtain better insight on the efficacy of the treatment.[6] Currently, the high cost of analysis and long waiting times hinder the wide spread implementation of POC diagnostics in emergency room, ICU and even at home.

In this section, 3 organic acids related to diabetes diagnosis were extracted from blood using the single breakdown device format described in Chapter One. Levels of beta-hydroxybutyrate (βOHB) in blood allow the clinician to differentiate between hyperglycaemia and potentially life threatening diabetic ketoacidosis (DKA), with blood levels of 3.5 mM βOHB or above considered indicative of DKA.[7] Here, the use of a nanojunction for the extraction of organic acids from whole blood was coupled with ITP with indirect fluorescence detection for their analysis.

3.1.2.1 Microfluidic Device and Nanojunction Formation

The microfluidic device is hybrid PDMS/glass with the single nanojunction design. The PDMS breakdown was done in two steps; first, 2200 V was applied while setting the current limit at 1.0 μA, then 2000 V was applied with a higher current limit at 2.0 μA. The two-step breakdown helped to form reproducible nanojunction pore size between devices and minimized the collapse of the formed nanochannels. All five devices tested showed a current of 70-100 nA when a 400 V was applied across the nanojunction. Permeability experiments verified that labelled BSA was blocked in all

devices while negatively charged fluorescent dye (CNF) was transported through the nanojunction except for one device, which also did not permit small ions like iron and thiocyanate.

3.1.2.2 Extraction and Analysis

After the nanojunction was formed, the breakdown buffer was replaced with the sample and the ITP electrolytes then injection and separation voltages were applied sequentially as indicated in Figure 3.4.

Organic acid solutions: The organic acids chosen for this study were pyruvate, lactate, and βOHB. Stock solutions (25 mM) of the acids in 100 mM NaCl were prepared from their sodium salts and stored in the fridge. Blood samples, with EDTA to prevent coagulation, were taken from a healthy volunteer and stored in the freezer at -4^{o}C.

ITP electrolytes: The LE was 20 mM HCl titrated with β-alanine to pH 3.3, 1% polyvinyl pyrrolidone (PVP) to suppress the EOF, and 250 μM R6G. The TE was 50 mM propionic acid. Stock solutions with double the concentrations were stored in the fridge and the LE was prepared daily by mixing equal amounts of the buffer-PVP and R6G.

Applied electric field: The electric field was applied to the microfluidic device using the in-house 4-channel power supply described under quinine analysis 3.1.1.2 Extraction and Analysis. Injection voltage was applied for 60 s to extract the acids from the sample then the voltage was switched to perform ITP with indirect detection.

Detection: Indirect fluorescence detection was done at 40.0 mm from the injection point. Blue LED was employed as the excitation source. Fluorescence

intensity was measured using a photon counter. Data acquisition was made by computer using a LabView program with 100 ms gate time.

Analytes were detected as steps in fluorescence intensity, which length can be related to the analyte concentration. The first derivative of the isotachopherograms enabled accurate measurements.

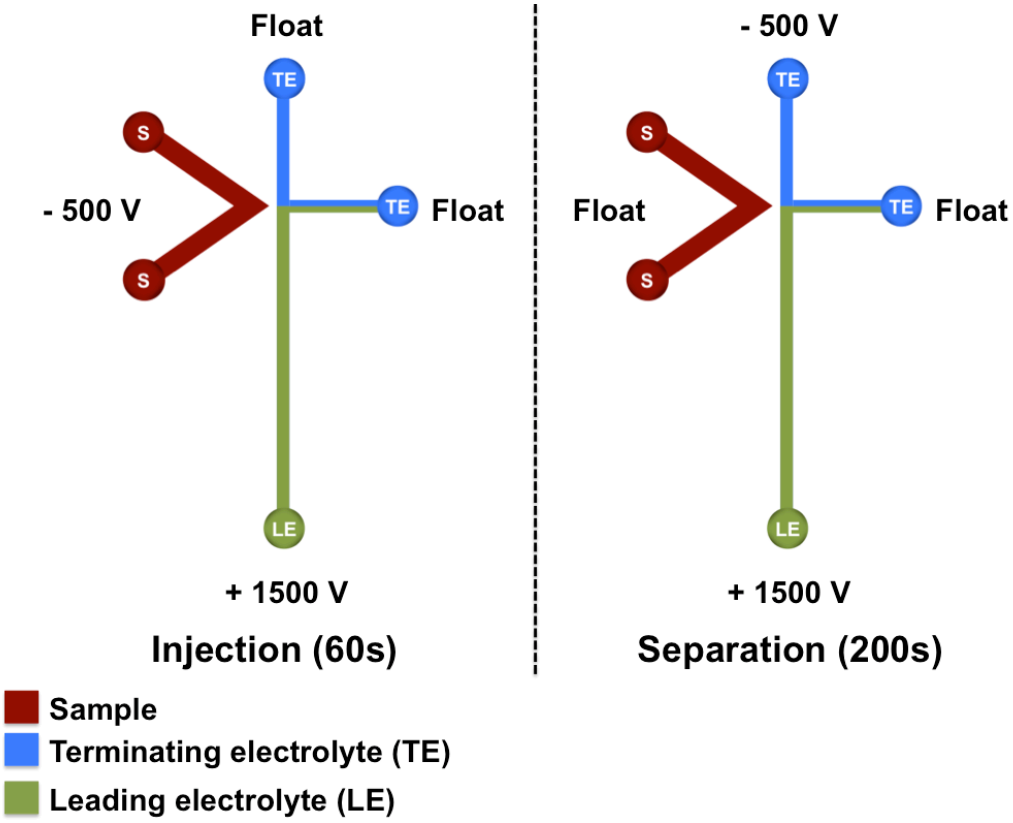

Figure 3.4 Experimental conditions for organic acids determination. Injection voltage was applied for 60 s to extract the acids from the sample then the voltage was switched to perform ITP with indirect detection. The LE was 20 mM HCl titrated with β-alanine to pH 3.3, 1% PVP to suppress the EOF, and 250 μM R6G. The TE was 50 mM propionic acid.

3.1.2.3 Results and Discussion

The organic acids chosen in this study were pyruvate, lactate and βOHB, which have pk_a values of 2.4, 3.9 and 4.7, respectively. At physiological pH, these acids will carry a negative charge. As discussed in Chapter One, ion transport of co-ions, anions in this case, is restricted through the nanojunctions. Anions can be transported if they are smaller than the free transport region in absence of EDL overlap. However, injection times are limited by the onset of ICP. The high ionic strength of blood may delay this onset, but the injected amount will be less than what can be detected unless a concentrating step is coupled to the extraction.

ITP is a powerful electrokinetic method allowing for the on-line concentration of analytes and separation. The main advantage is that enhancement factors are not compromised by high salt content in the sample matrix. The analytes are bracketed between the LE, which has the highest electrophoretic mobility, and the TE, which has the lowest electrophoretic mobility in the system. At steady state, the analytes will stack in zones according to their respective mobility. Analyte concentration can be measured from the zone length as opposed to peak height in CZE. The ITP electrolytes employed were chosen based on the work done by Krivankova and Bocek[8] and Dolnik and Bocek.[9] The leading ion is chloride and the terminating ion is propionic acid. The difference in their mobilities defines the mobility window within which different analytes can be stacked. Optimum separation of organic acids in serum was reported to be at pH 3.3.[9] ITP performs better under suppressed EOF conditions which was achieved using 1% PVP. Indirect fluorescence detection was enabled by using R6G as a non-focusing tracer, which is a ‘counter speeder’ as it is positively charged at pH 3.3 and migrates in the opposite direction to the analytes. The concept of non-focusing tracer for indirect fluorescence detection in ITP systems

was first introduced by Chambers and Santiago.[10] A fluorescent counterionic dye was added to the LE. During the ITP, the dye concentration will reflect local variations in the concentration of non-fluorescent analytes. The TE was 50 mM propionic acid, which has lower mobility than any of the acids chosen for this study.

The black trace in Figure 3.5 shows 2 steps corresponding to the LE and TE. The theoretical peak capacity can be calculated using the following formula;

$$Theoretical\ capacity = \frac{Step\ height}{Noise \times 3}$$

The step height is 67,000 and the noise is 2,000, which gives a theoretical peak capacity of 11 peaks. However, experimental results often show a lower number. ITP of a mixture of organic acids (Figure 3.5 blue trace) shows adequate separation of the 3 acids. Pyruvate, having the highest mobility, directly migrated after the LE, followed by lactate, βOHB, then TE. The first derivative of the isotachopherogram converts minor changes in the slope into sharp peaks. The distance between the peak maxima in the first derivative corresponds to step length in the isotachopherogram. The acids were dissolved in 100 mM NaCl to mimic the high ionic strength of blood samples.

Extraction from blood was demonstrated using spiked samples (Figure 3.6). Pyruvate suffered interference from other anions in the sample matrix like phosphate, citrate and acetoacetate. These ions were also observed by Dolnik and Bocek[9] in human serum. The blood samples were provided by a healthy volunteer and lactate levels were determined above their normal range. Further investigation revealed that the samples were withdrawn shortly after physical exercise, which may have lead to elevated lactate levels.[11]

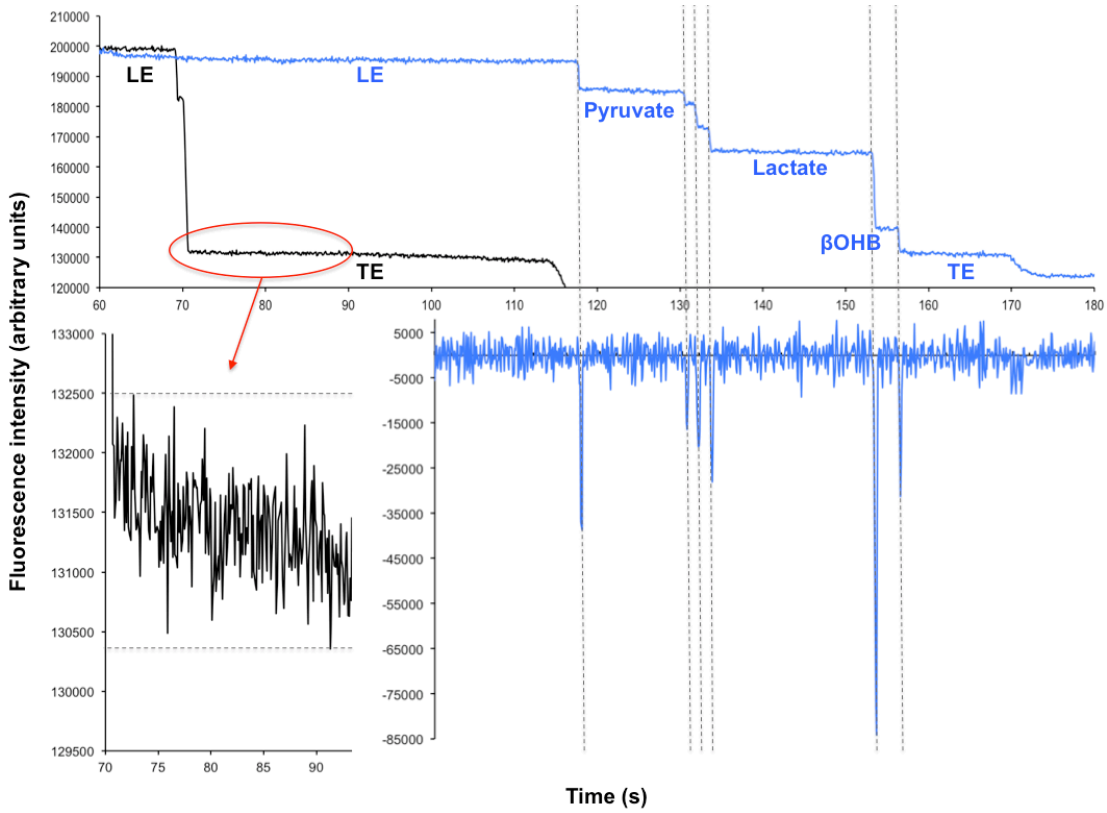

Figure 3.5 Isotachopherograms for organic acids. Black trace; blank and zoom in to measure the baseline noise. Blue trace; separation of a mixture of 25 mM of each organic acid in 100 mM NaCl and the corresponding first derivative.

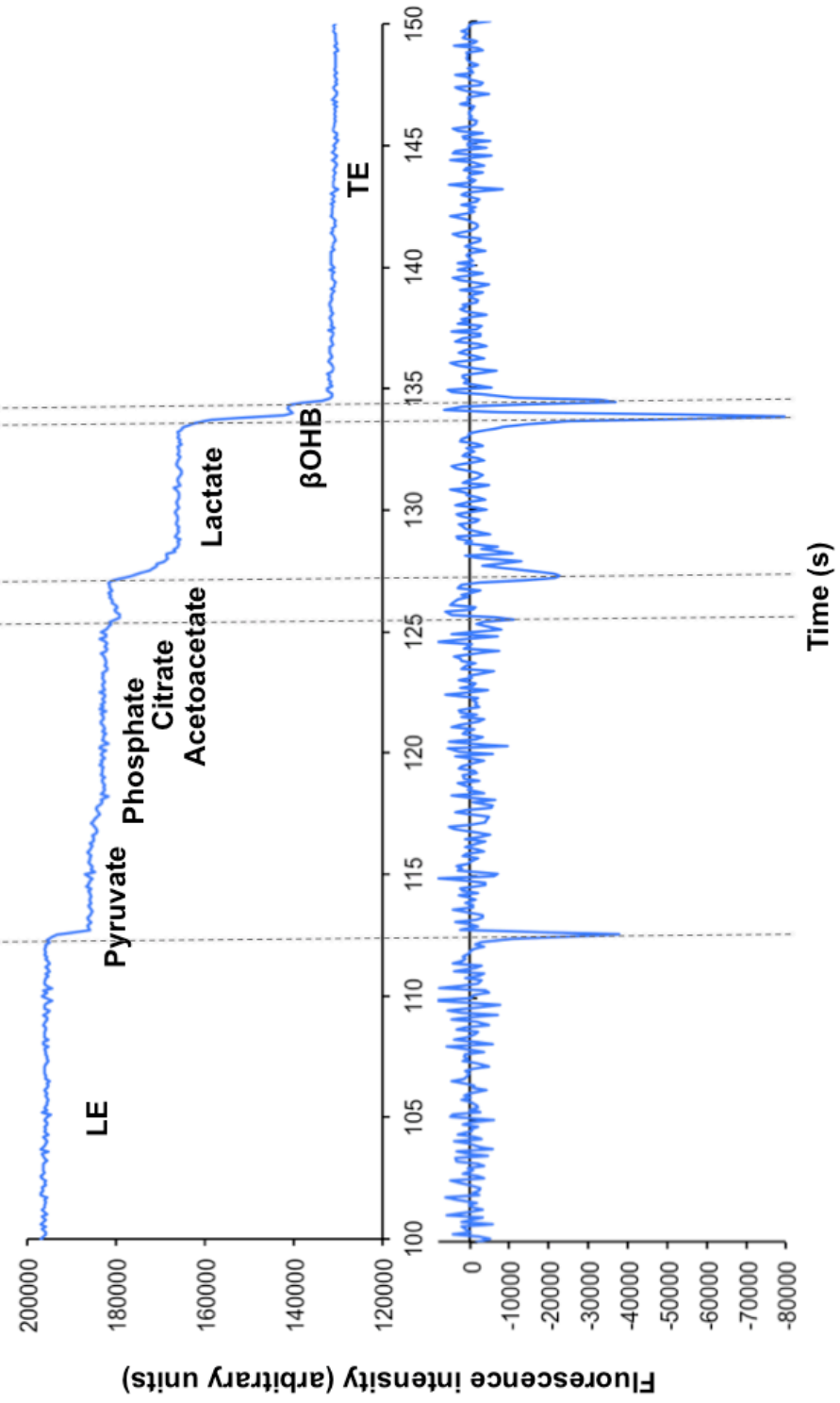

Figure 3.6 Isotachopherogram and its respective first derivative for blood sample spiked with 2.5 mM of each organic acid.

3.1.3 Extraction and Analysis of Ampicillin in Blood

A challenging case where TDM can be a valuable tool is dosage tailoring for critically ill septic patients treated with antimicrobials. The general inflammatory response associated with sepsis leads to increased volume of distribution and hence lower blood levels of hydrophilic drugs but when other organs start to fail, like the kidneys, decreased clearance leads to accumulation and toxic levels of the drug.[12] Sepsis is fatal for 30 to 50% of all patients. At such high mortality rates, treatment approaches include attempts to clean the blood regardless of the pathogen,[13] prediction of the outcomes by measuring cell-free DNA[14] and dose modulation guided by pharmacokinetic and pharmacodynamics studies.[15] Early diagnosis and quick optimization of the dosing are crucial for the patient's survival.[16] The selection of the dosage is the most critical and perhaps most difficult to determine[16b] due to significant alterations in the pharmacokinetic behaviour of drugs caused by unpredicted changes in the patient's hemodynamic state. It is particularly challenging in neonatal samples, where it is one of the major causes of death of newborns[17] and both sample volume and time are critical. TDM of antimicrobials for managing sepsis is currently done in a few hospitals using mainly HPLC[18] and can determine the free form for highly protein bound antimicrobials.[19] The method is highly accurate but requires the transfer of samples to the central laboratory. Ampicillin is a first line antibiotic in treating sepsis, in combination with gentamicin or a third generation cephalosporin, and exhibit negligible binding to plasma protein[20] but have low stability in biological fluids.[21] The time between sample withdrawal and analysis may introduce errors in the results as well as delay any corrective dosage adjustment.

The extraction of the target analytes from biological samples is a bottleneck in analysis. In this section I present SMTs described before in Chapter One for on-site TDM of ampicillin in blood. SMTs offer a simple and new alternative for the on-chip extraction, concentration and desalting of pharmaceuticals from whole blood. Seamless integration with an electrophoretic separation allows quantitative analysis within minutes and without the need for pumps, complex device fabrication or use of solvents.

The trap consists of two nanojunctions of different pore size to govern ionic transport based on the ion charge and hydrodynamic size. Ampicillin in blood was determined within 5 min with linear response over 2.5-20 μg/mL, which covers the recommended levels for treating sepsis. This simple approach to integrated sample treatment provides a new way to advance the field of personalized drug monitoring.

3.1.3.1 Microfluidic Device and Nanojunction Formation

The device is a hybrid PDMS/glass with the SMT design previously described in Chapter One. The breakdown electrolyte was 10 mM phosphate buffer.

3.1.3.2 Extraction and Analysis

After the nanojunction was formed, the breakdown buffer was replaced with the sample and the buffers then injection and separation voltages were applied sequentially as indicated in Figure 3.7.

Ampicillin stock and blood samples: Ampicillin (from Sigma-Aldrich) was used to prepare 1 mg/mL stock solution. This solution was used to spike blood samples to obtain different concentrations (2.5, 5.0, 10.0, 15.0, and 20.0 μg/mL). Whole blood samples from a healthy volunteer were treated with disodium EDTA to

prevent coagulation and divided into small volumes (200 μL) then stored in the freezer at -4^{o}C.

BGE system: The separation channel was filled with 100 mM phosphate buffer, pH 11.5, and 0.5% HPMC whilst the waste V-channel was filled with 10 mM phosphate buffer, pH 11.5.

Applied electric field: An in-house, 4-channel power supply (0-5 kV) was used to apply electric field to the microfluidic device through 6 platinum electrodes. The two electrodes connected to each V-channel share the same applied voltage. Electrokinetic extraction of ampicillin was done from whole blood for 200 s. After extraction, the high voltage was switched to perform electrophoretic separation in the separation channel, with the ampicillin peak passing the detector at 135 s.

Detection: Quantitative measurements were done using a PMT connected to the fluorescence microscope as described in the Appendix under Detection.

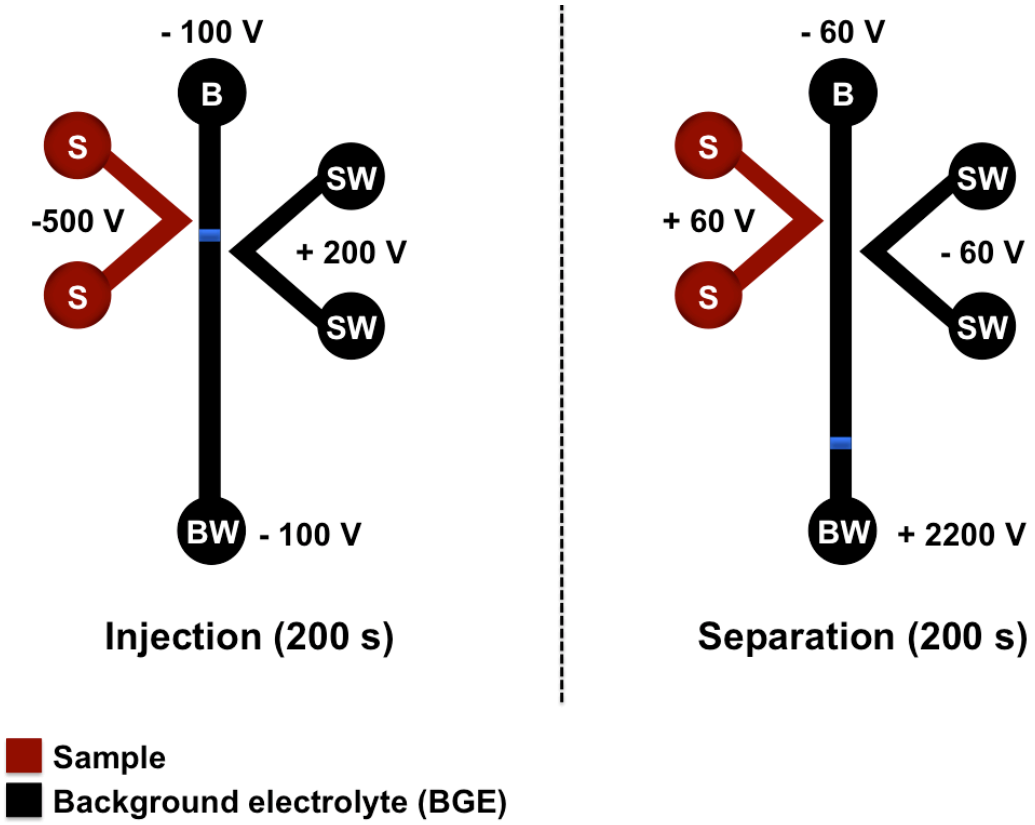

Figure 3.7 Experimental conditions for ampicillin analysis. Injection voltage was applied for 200 s to extract ampicillin from blood then the voltage was switched to perform electrophoretic separation with fluorescence detection. The separation channel was filled with 100 mM phosphate buffer, pH 11.5, and 0.5% HPMC whilst the waste V-channel was filled with 10 mM phosphate buffer, pH 11.5.

3.1.3.3 Results and discussion

The SMT is based on the combination of two nanojunctions with different pore size connected in series to form a one-way trap, which selectively extracts and concentrates low molecular weight anions (200-1000 Da) from biological fluids like whole blood.

The SMT was used for the analysis of ampicillin in blood to demonstrate its potential for on-site TDM. Spiked whole blood samples from a healthy volunteer were labelled with fluorescamine to facilitate fluorescence detection and negative pressure was used to fill the sample V-channel. Fluorescamine reacts with primary amines to produce fluorescent compounds within seconds whilst the excess reagent hydrolyses into a non-fluorescent product. Labelled ampicillin was trapped in the SMT before electrophoretic separation (Figure 3.8a). The linear range of 2.5-20 μg/mL ampicillin (RSD = 17%, n = 4 devices, 10 μg/mL ampicillin) covers the recommended blood level for treating sepsis of 10 μg/mL ampicillin (Figure 3.8b). The LOQ offered by HPLC methods can be as low as 0.1 μg/mL using 200 μL of plasma.[19] Such low levels are not necessary considering the minimum inhibitory concentration of ampicillin. It is more beneficial to use smaller sample volumes especially when monitoring preterm infants, sample volume should not exceed 75 μL.[22] The proposed assay requires only 40 μL of blood to provide results within 5 min.

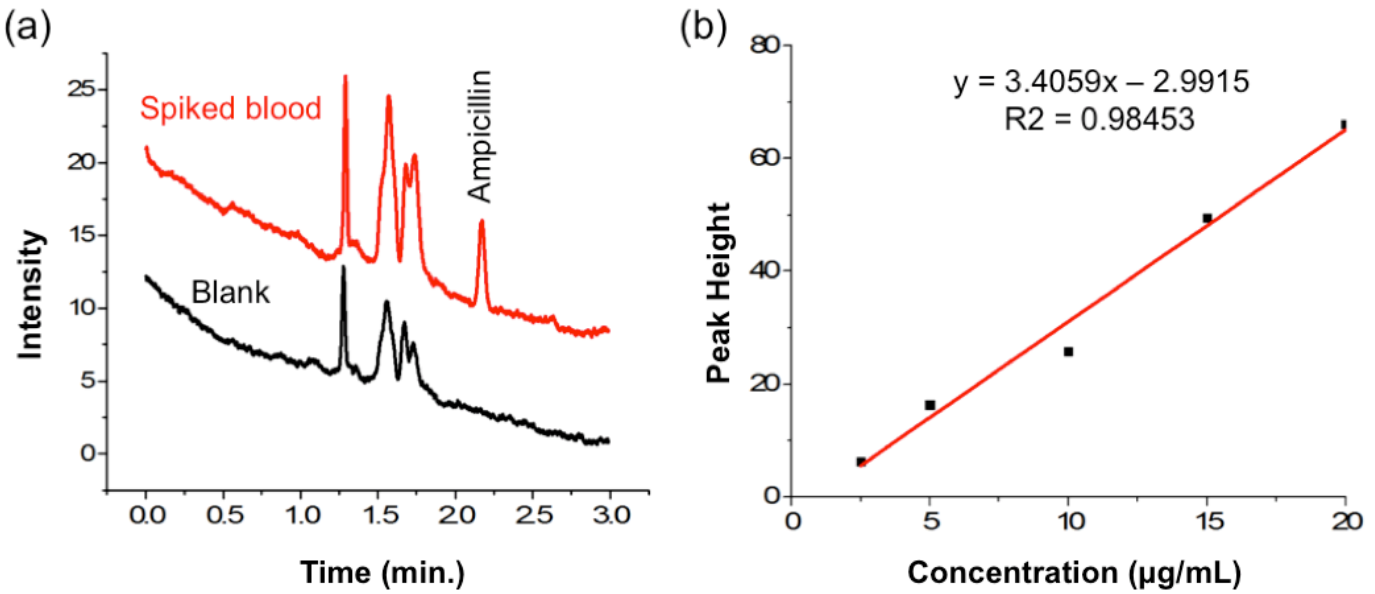

Figure 3.8 Electropherograms showing the analysis of ampicillin from whole blood. (a) Extraction through the nanojunction made with optimized current limit of 5 µA and concentration using the purification nanojunction created with a current limit of 0.5 µA. Blank whole blood (black) and whole blood spiked with 2.5 µg/mL ampicillin (red). (b) The linear calibration curve for ampicillin from whole blood. Applied voltage for extraction was -100, -500, -100, and +200 (100 s) and for separation was -60, +60, +2200, and -60 for reservoirs B, S, BW and SW, respectively.

3.2 Conclusions

Controlled dielectric breakdown of PDMS enabled tuning of the nanojunctions' pore size and hence their permeability for molecules of different molecular weights. This method enabled the analysis of the drug quinine in 3 min and ampicillin in less than 5 min directly from whole blood, using a disposable microfluidic device. Simple electric field application was required to form the filtration element directly before analysis. This approach is generic and can be applied to a wide range of pharmaceutical compounds for TDM or POC diagnostics. Quinine was used as a model positively charged drug due to its inherent fluorescence. Small organic acids as an example of non-fluorescent anions were extracted from blood and analysed by ITP with indirect detection. Ampicillin as a model for negatively charged drug was labelled off-chip with fluorescamine, within few seconds, to enable fluorescence detection. This approach can be used for a wide range of pharmaceutical compounds and metabolites. Fabrication of the nanojunctions by dielectric breakdown is fast, simple, and the electronic control over pore size allows for their incorporation without significantly adding to the cost of fabrication of the microchip. The device does not rely on pumps or valves, allowing for simple operation. Upon further engineering of the peripherals; power supply, light source, detector, etc., the device can be portable and would offer great potential for application in POC devices and portable screening devices.

3.3 References

1. Vieira, J. L. F.; Borges, L. M. G.; Nascimento, M. T. S.; Gomes, A. d. L. S., Quinine levels in patients with uncomplicated falciparum malaria in the Amazon region of Brazil. *Brazilian Journal of Infectious Diseases* **2008,** *12*, 353-354.
2. Kolawole, J. A.; Mustapha, A., Improved RP-HPLC determination of quinine in plasma and whole blood stored on filter paper. *Biopharmaceutics & Drug Disposition* **2000,** *21* (9), 345-352.
3. Mikuš, P.; Maráková, K.; Veizerová, L.; Piešťanský, J., Determination of quinine in beverages by online coupling capillary isotachophoresis to capillary zone electrophoresis with UV spectrophotometric detection. *Journal of Separation Science* **2011,** *34* (23), 3392-3398.
4. Verity, B.; Bigger, S. W., The dependence of quinine fluorescence quenching on ionic strength. *International Journal of Chemical Kinetics* **1996,** *28* (12), 919-923.
5. Franke, U.; Proksch, B.; Muller , M.; Risler, T.; Ehninger, G., Drug monitoring of quinine by HPLC in cerebral malaria with acute renal failure treated by haemofiltration. *European Journal of Clinical Pharmacology* **1987,** *33*, 293-296.
6. Wallace, T. M.; Matthews, D. R., Recent advances in the monitoring and management of diabetic ketoacidosis. *QJM* **2004,** *97* (12), 773-780.
7. (a) Charles, R.; Bee, Y.; Eng, P.; Goh, S., Point-of-care blood ketone testing: screening for diabetic ketoacidosis at the emergency department. *Singapore Medical Journal* **2007,** *48* (11), 986-989; (b) Sheikh-Ali, M.; Karon, B. S.; Basu, A.; Kudva, Y. C.; Muller, L. A.; Xu, J.; Schwenk, W. F.; Miles, J. M., Can serum β-hydroxybutyrate be used to diagnose diabetic ketoacidosis? *Diabetes Care* **2008,** *31* (4), 643-647; (c) Stojanovic, V.; Ihle, S., Role of beta-hydroxybutyric acid in

diabetic ketoacidosis: A review. *The Canadian Veterinary Journal* **2011,** *52* (4), 426-430.

8. Křivánková, L.; Boček, P., Determination of pyruvate, acetoacetate, lactate, and 3-hydroxybutyrate in plasma of patients with diabetes mellitus by capillary isotachophoresis. *Journal of Microcolumn Separations* **1990,** *2* (2), 80-83.
9. Dolník, V.; Boček, P., Determination of pyruvate, lactate, acetoacetate, and 3-hydroxybutyrate in serum by capillary isotachophoresis. *Journal of Chromatography B: Biomedical Sciences and Applications* **1981,** *225* (2), 455-458.
10. Chambers, R. D.; Santiago, J. G., Imaging and quantification of isotachophoresis zones using nonfocusing fluorescent tracers. *Analytical Chemistry* **2009,** *81* (8), 3022-3028.
11. Goodwin, M. L.; Harris, J. E.; Hernández, A.; Gladden, L. B., Blood lactate measurements and analysis during exercise: A guide for clinicians. *Journal of diabetes science and technology (Online)* **2007,** *1* (4), 558-569.
12. Blot, S.; Lipman, J.; Roberts, D. M.; Roberts, J. A., The influence of acute kidney injury on antimicrobial dosing in critically ill patients: are dose reductions always necessary? *Diagnostic Microbiology and Infectious Disease* **2014,** *79* (1), 77-84.
13. Kang, J. H.; Super, M.; Yung, C. W.; Cooper, R. M.; Domansky, K.; Graveline, A. R.; Mammoto, T.; Berthet, J. B.; Tobin, H.; Cartwright, M. J.; Watters, A. L.; Rottman, M.; Waterhouse, A.; Mammoto, A.; Gamini, N.; Rodas, M. J.; Kole, A.; Jiang, A.; Valentin, T. M.; Diaz, A.; Takahashi, K.; Ingber, D. E., An extracorporeal blood-cleansing device for sepsis therapy. *Nature Medicine* **2014,** *20* (10), 1211-1216.

14. Forsblom, E.; Aittoniemi, J.; Ruotsalainen, E.; Helmijoki, V.; Huttunen, R.; Jylhava, J.; Hurme, M.; Jarvinen, A., High cell-free DNA predicts fatal outcome among Staphylococcus aureus bacteraemia patients with intensive care unit treatment. *PLOS one* **2014,** *9* (2), e87741.

15. Goncalves-Pereira, J.; Paiva, J.-A., Dose modulation: A new concept of antibiotic therapy in the critically ill patient? *Journal of Critical Care* **2013,** *28* (4), 341-346.

16. (a) Kumar, A.; Roberts, D.; Wood, K. E.; Light, B.; Parrillo, J. E.; Sharma, S.; Suppes, R.; Feinstein, D.; Zanotti, S.; Taiberg, L.; Gurka, D.; Kumar, A.; Cheang, M., Duration of hypotension before initiation of effective antimicrobial therapy is the critical determinant of survival in human septic shock*. *Critical Care Medicine* **2006,** *34* (6); (b) McKenzie, C., Antibiotic dosing in critical illness. *Journal of Antimicrobial Chemotherapy* **2011,** *66* (suppl 2), ii25-ii31.

17. Requejo, J. H.; Bryce, J.; Barros, A. J. D.; Berman, P.; Bhutta, Z.; Chopra, M.; Daelmans, B.; de Francisco, A.; Lawn, J.; Maliqi, B.; Mason, E.; Newby, H.; Presern, C.; Starrs, A.; Victora, C. G., Countdown to 2015 and beyond: fulfilling the health agenda for women and children. *The Lancet* **2014,** (0).

18. Wong, G.; Brinkman, A.; Benefield, R. J.; Carlier, M.; De Waele, J. J.; El Helali, N.; Frey, O.; Harbarth, S.; Huttner, A.; McWhinney, B.; Misset, B.; Pea, F.; Preisenberger, J.; Roberts, M. S.; Robertson, T. A.; Roehr, A.; Sime, F. B.; Taccone, F. S.; Ungerer, J. P. J.; Lipman, J.; Roberts, J. A., An international, multicentre survey of β-lactam antibiotic therapeutic drug monitoring practice in intensive care units. *Journal of Antimicrobial Chemotherapy* **2014,** *69* (5), 1416-1423.

19. Briscoe, S. E.; McWhinney, B. C.; Lipman, J.; Roberts, J. A.; Ungerer, J. P. J., A method for determining the free (unbound) concentration of ten beta-lactam antibiotics in human plasma using high performance liquid chromatography with ultraviolet detection. *Journal of Chromatography B* **2012,** *907* (0), 178-184.

20. Wong, G.; Briscoe, S.; Adnan, S.; McWhinney, B.; Ungerer, J.; Lipman, J.; Roberts, J. A., Protein binding of β-lactam antibiotics in critically ill patients: Can we successfully predict unbound concentrations? *Antimicrobial Agents and Chemotherapy* **2013,** *57* (12), 6165-6170.

21. do Nascimento, T. G.; de Jesus Oliveira, E.; Basílio Júnior, I. D.; de Araújo-Júnior, J. X.; Macêdo, R. O., Short-term stability studies of ampicillin and cephalexin in aqueous solution and human plasma: Application of least squares method in Arrhenius equation. *Journal of Pharmaceutical and Biomedical Analysis* **2013,** *73* (0), 59-64.

22. Koren, G., Therapeutic drug monitoring principles in the neonate. *Clinical Chemistry* **1997,** *43* (1), 222-227.

4 Sample Preparation for Biopolymers - Introduction

This chapter was published as a review paper; **Shallan, A.; Guijt, R.; Breadmore, M., Electrokinetics for sample preparation of biological molecules in biological samples using microfluidic systems. *Bioanalysis* 2014, 6 (14), 1961-1974.** Little changes were made to update the literature.

4.1 Introduction

The challenge for personalized medicine and POC devices is to be able to provide a laboratory-based measurement within minutes using exceptionally small and highly integrated instrumentation that can be used by an unskilled and minimally trained operator. The targets are diverse, ranging from small molecule drugs and their metabolites, through to large macromolecules such as proteins and DNA, each of which present different analytical challenges that need to be overcome. Common to all is the need to deal directly with crude, unprocessed biological samples, and the need to integrate a simple and effective strategy to manipulate the sample into a form such that the target can be measured.

There is no single strategy that is universally applicable; a unique approach is required for each application and depends upon the sample type, target molecule, timeframe, cost and detection limit. Genetic targets such as mutations in *BRCA1* and *BRAC2*, which indicate a higher susceptibility to breast cancer, require that the DNA be isolated and purified, the relevant regions amplified through polymerase chain reaction (PCR) and the fragments detected to confirm the presence of the gene. The nature of PCR is highly beneficial for providing both selectivity and sensitivity. However, PCR is only applicable for DNA/RNA. For other biomarkers, such as the prostate-specific antigen,[1] a biomarker for prostate cancer, and proteins like cardiac

troponin I, which is a marker for cardiac myocyte injury,[2] a different approach is required. The challenge in detecting protein biomarkers is that the upper reference limit is 0.1 ng/mL, which is 10^8 times less than the highly abundant plasma proteins such as albumin and IgG (>1 mg/mL).

While it is possible to simply integrate existing laboratory strategies seamlessly in a completely integrated microfluidic device, the question must be asked as to whether this is the right approach and whether there are alternative ways to deal with crude samples that, by their very nature, are amenable to miniaturization. Electrokinetic methods are the perfect approach to realize this. They involve the manipulation of fluid and ion movement with electric fields and were the preferred separation method for implementation in microfluidic devices from the early 1990s because only a high voltage power supply is required to transport and separate analytes, avoiding the need to use pumps. The last two decades have seen the development of a number of simple and powerful electrokinetic approaches for sample treatment, particularly for target concentration to enhance sensitivity. A number of these have been implemented in a microfluidic device to great effect (e.g., the million-fold enhancement factors achieved by ITP[3] or the enrichment at nano-/micro-channel interfaces.[4] The limitation, however, is that the majority of these are not applicable to a crude sample and require some other form of sample preparation. In some instances, there is potential for this to be performed in an integrated chip, such as extractions through droplets[5] or laminar in H-filters®;[6] however, these have yet to be coupled with a microfluidic separation. It is worth noting that the greater the complexity of the processes that need to occur in the microfluidic device, the more complex the instrumentation required to operate it and the less likely it is to be robust and reliable.

This chapter focuses on electrokinetics in microchips for sample treatment of a crude, unprocessed biological sample, the first step in the analytical chain, because this is the most challenging part of the process from a point-of-collection perspective. The approaches discussed need not be specific to POC device, in some instances, they are attractive for implementation in laboratory based instrumentation to service more routine analyses, but this is the hardest application environment and is the area where electrokinetics has significant advantages over current alternative approaches.

4.1.1 Electrokinetics – the basics.

The premise of electrokinetic sample preparation is to isolate and perhaps concentrate the target molecule(s) through the application of electric fields. Electrodialysis through a membrane was reported for the extraction of peptides from synovial fluid samples.[7] 27 new peptides were identified using nano-LC-MS after 10 min electrodialysis into acceptor solution of 25 mM ammonium acetate (pH 3.8) containing 20% v/v DMSO and an applied electric field of 150 V/cm (300 V).

The most widespread use of electrokinetics for sample preparation is for stacking; the concentration of the target species at the sample/electrolyte interface. Stacking is particularly effective when the conductivity of the injected sample is at least 10 times lower than that of the BGE, which is called field amplified sample stacking (FASS). If ions are injected under field amplified conditions (called field amplified sample injection, FASI), then even greater concentration factors can be obtained. This can be explained by the fact that ions are injected at a rate according to the sum of their electrophoretic mobility and the EOF, while the amount of solvent injected is determined only by the EOF. Thus, when the same physical volume of sample is injected, more analyte ions can be injected when compared with a

hydrodynamic injection with the same matrix volume, so the sensitivity can be improved. One of the limitations of FASI is that there is a bias; higher mobility ions will be injected at a higher rate than ions with lower mobility. While powerful, FASI is reliant on a low ionic strength sample and is therefore not directly applicable to the relatively high salt content of biological samples.

A simple and elegant way to deal with high salt samples is by pH-mediated sample stacking, introduced by Lunte and co-workers.[8] This overcomes the problem of high conductivity matrix by neutralizing the weak counter ions in the sample by strong acids or bases injected electrokinetically after the sample. The weak acid/base is neutralized, creating a low conductivity zone. Following careful optimization of the injection times for the acid/base, the detection limits of PCR amplified DNA in microchip gel electrophoresis were decreased by a factor of 8 by neutralizing the Tris ions from the run buffer by electrokinetically injected hydroxide ions, thereby forming a low conductivity zone.[9]

Shiddiky and Shim[10] reached 25,000-fold increase in sensitivity within 125 s using microchip electrophoresis of DNA with electrochemical detection. They combined FASI with gold nanoparticle modified buffers and electrodes. The modified electrodes resulted in 10 times the peak current compared with bare electrodes and a 450-fold enhancement due to the stacking step alone. It is suspected that the low ionic strength of the sample (10 mM Tris-HCl at pH 8.0) contributed to the high concentration factor achieved, making this approach not directly applicable to biological samples.

4.1.2 Electrophoretic separations for sample pretreatment

One of the main purposes of sample pretreatment is to isolate and concentrate the target species. This is typically performed with low resolution techniques; all compounds of interest are isolated and then introduced collectively for analysis. A high-resolution separation can be equally as powerful for sample pretreatment, and is in fact one of the most powerful methods for altering a sample composition prior to a second analytical separation. This is the basis of 2D electrophoresis, in which proteins are first separated by IEF before a second separation by SDS-polyacrylamide gel electrophoresis (SDS-PAGE). IEF focuses zwitter ionic compounds into very narrow zones according to their isoelectric point (pI). A mixture of amphoteric buffer ions, carrier ampholytes, is used to establish a pH gradient along the channel length. When a protein hits a zone where it becomes neutral, it stops moving and focuses as a sharp zone. A whole column-imaging detector eliminates the need for mobilization and helps to keep the zones sharp. Separation in miniaturized IEF is more efficient as higher electric fields can be applied while Joule heating is kept to minimum as a result of the larger surface area to volume. IEF was coupled with CZE for the separation of standard proteins.[11] The IEF step formed separated zones in less than 1 min and offered a 73-fold concentration enhancement. The system achieved a total peak capacity of approximately 1300. Microchip SDS-PAGE/IEF separation of a fluorescently labelled protein standard containing proteins with a molecular weight range of 20,000–200,000 Da was achieved in less than 30 s using the high sieving power of a photopatterned polyacrylamide gel in ultrashort channels.[12]

ITP is one of the oldest electrokinetic techniques, and unlike IEF, which is only applicable to zwitter ionic analytes, ITP is applicable to all charged species. Analytes are detected as steps which length is proportional to the analyte

concentration. The use of non-uniform microchannels in which the cross-section area becomes smaller causes the zones to become longer, thereby conserve mass and charge according to the Kohlrausch regulating function. This was demonstrated for indirect fluorescence detection of BisTris as a model analyte.[13] Subsequently, an enhancement of 10,000-fold for fluorescent proteins was achieved through a 100 times reduction in channel dimensions,[14] which was then applied for the determination of the biomarker cardiac troponin I[15] and its phosphorylated forms[16] in the presence of serum proteins and direct fluorescence detection with a similar concentration factor.

One of the unique aspects of ITP is that ions are equalized to a concentration defined by their mobility and the leading ion concentration. Ions with an initial concentration higher than the leader are diluted, while ions with a concentration lower than the leader are concentrated. This makes it suitable for high conductivity samples as the concentrations of the matrix ions are adjusted down, while the trace ions are concentrated. Biological samples are also ideal because sodium and chloride are typically in high abundance and have a sufficiently high electrophoretic mobility to allow them function as leading ions for a large number of target analytes. One of the consequences of the separation mechanism is that the migration time depends on the concentrations of the species, rather than on their ionic mobilities, and hence any variations in the concentrations of ions with a mobility between the leader and target cause the time of detection to change. Thus, ITP has predominantly been used coupled with another separation, such as zone electrophoresis (ITP-ZE), in order to allow for analyte identification based on migration time. This can be performed by coupling two separate microchannels such that zones from the ITP channel are separated in a second electrophoresis channel, or in a single channel in a transient

(tITP) manner. This is where an initial ITP separation is induced to equalize the concentrations of all ions in the sample prior to the ITP being dissipated, transitioning to a normal ZE separation. Applications include concentrating small RNAs from cell lysate samples,[17] coupled with gel electrophoresis for analysis of DNA in PCR samples,[18] and coupled with CE for analysis of proteins in infant milk formula[19] and urinary proteins in clinical samples.[20]

Because ITP-ZE is compatible with high salinity samples, a direct live cell assay from high ionic strength (>140 mM NaCl) media was possible. In a microchip containing 5 ports for loading of the different BGEs, the switch from ITP to ZE was done by introducing LE behind the concentrated plug without additional sample pretreatment.[21] The same principle was applied for DNA genotyping of hepatitis B virus in serum samples after one PCR amplification round and 10 times dilution of the product.[22]

For an analyte to reach the steady state and form a plateau in an ITP system, it has to exceed a limiting concentration determined by its electrophoretic mobility and LE concentration according to Kohlrausch regulating function. Trace analytes will pass the detection point as sharp peaks squeezed between concentrated zones of more abundant analytes. This has recently been called ‘peak-mode ITP’. The most significant application of this mode of ITP in recent years was demonstrated by the Santiago group, who concentrated and purified DNA.[23] Proteins are removed through digestion with Proteinase K, with the nucleic acids concentrated from the mixture and collected in the end reservoir for PCR. This process is a quick and powerful alternative to SPE – the only other DNA purification method that has been routinely implemented in microchips. Subsequent to this work, the same group has also demonstrated the ability to purify and concentrate ribonucleic acid (RNA). Extraction

of RNA with adequate RNase control and RNA integrity was achieved from whole human blood infected with *Pseudomonas putida* within 5 min.[23a] The TE chemistry was chosen to protect the RNA from exogenous and endogenous RNase degradation.

Building on this further, Santiago's group demonstrated the power of ITP for derivatization by forcing target nucleic acid and a fluorescent hybridization probe with complimentary sequence into the same space in peak-mode ITP to achieve simultaneous purification, concentration and hybridization.[23b-d] The most significant outcome is an increase in hybridization kinetics, approximately 2-3 orders of magnitude, such that hybridizations that took hours were completed in seconds. A number of approaches were presented based upon this to improve the ability to detect specific fragments of target DNA. The first was the use of molecular beacons which fluoresce only after binding with a complimentary sequence, but self-quench in free state (Figure 4.1).[23b] The second approach was to use a hybridization probe and to remove the excess probe on photopatterned hydrogel functionalized with complimentary DNA, which enabled the use of higher probe concentrations (Figure 4.2).[23c] Later, a spacer ion in conjunction with a sieving matrix was used to separate the hybridized DNA from the free-probe.[23d] The spacer ion was chosen such that it had a lower ionic mobility than the LE, probe, target, and probe-target complexes, enabling mixing and hybridization. When the zones entered the sieving matrix, the mobility of the probe-target complex was reduced to below that of the spacer, thus facilitating separation from the free-probe while still allowing the probe-target to separate in an ITP zone in order to preserve sensitivity. This work is undoubtedly the most exciting in the field of electrokinetic sample preparation as it provides a solid basis upon which it is entirely feasible to developed sub-minute genetic diagnostics for quite complex analyses.

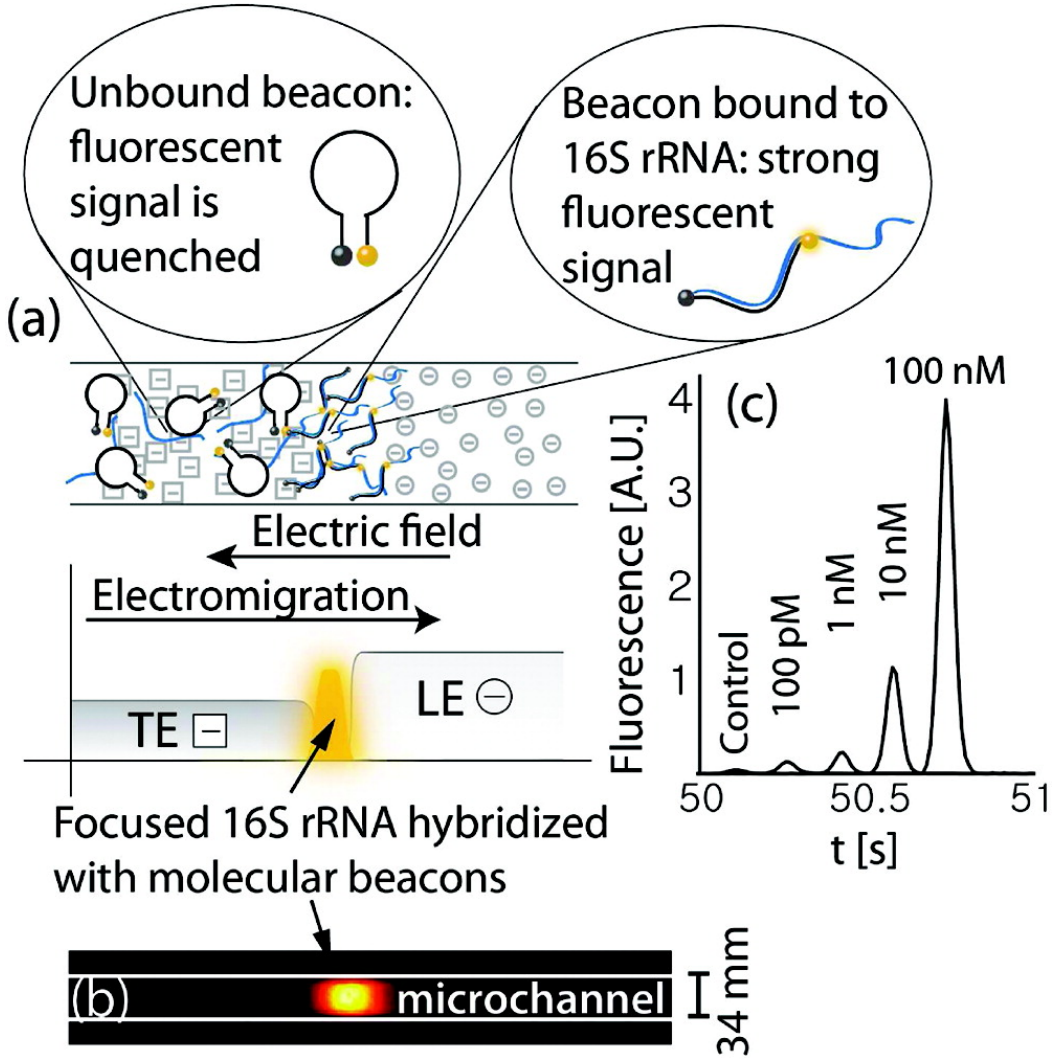

Figure 4.1 (a) Schematic showing simultaneous ITP extraction, focusing, hybridization (with molecular beacons), and detection of 16S rRNA bound to a molecular beacon. (b) Raw experimental image showing fluorescence intensity of molecular beacons hybridized to synthetic oligonucleotides using ITP. (c) Detection of oligonucleotides having the same sequence as the target segment of 16S rRNA. Adopted with permission from M. Bercovici, G. V. Kaigala, K. E. MacH, C. M. Han, J. C. Liao and J. G. Santiago, Analytical Chemistry **83** (11), 4110-4117 (2011). Copyright 2011 American Chemical Society.

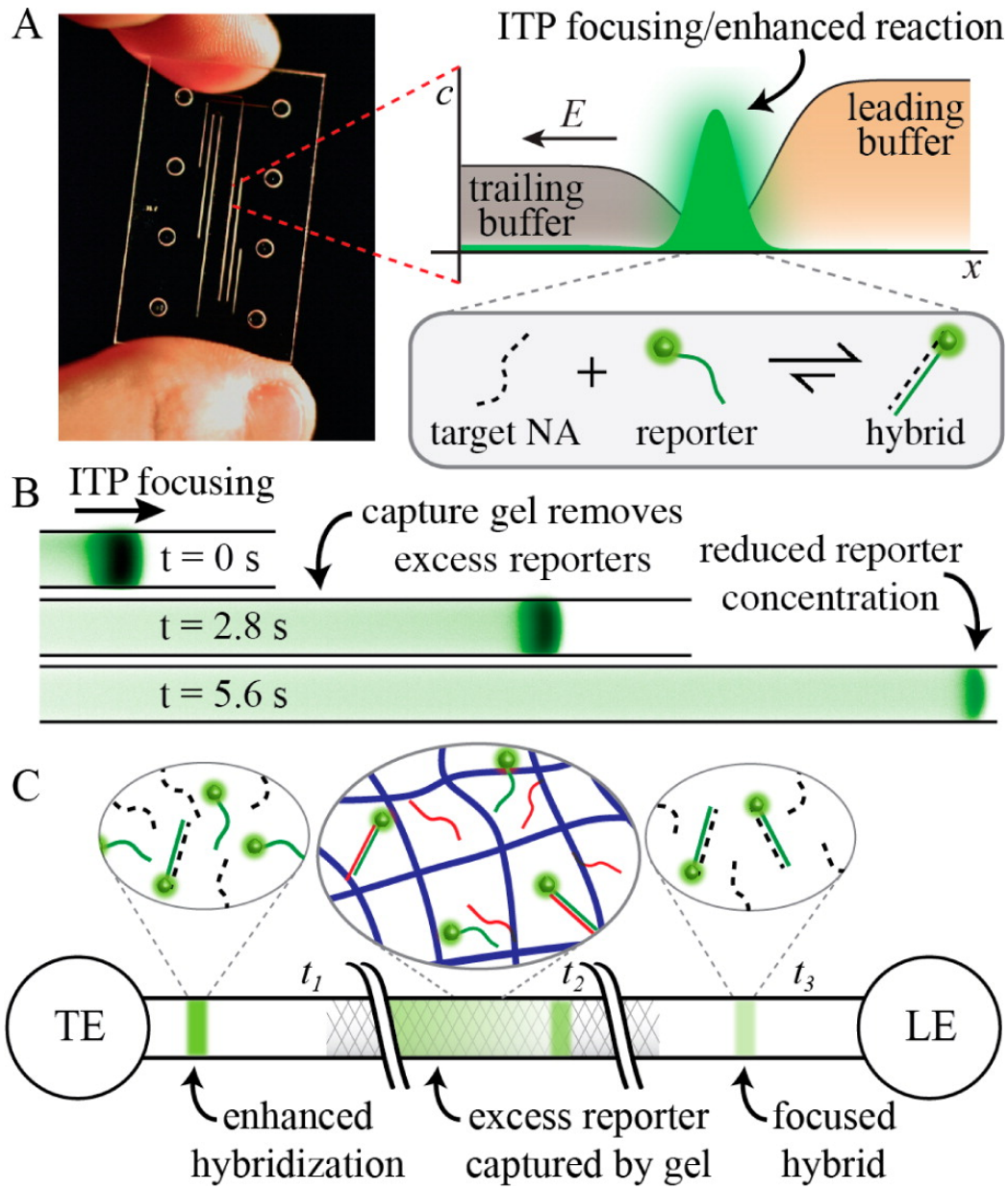

Figure 4.2 Integration of on-chip ITP and affinity hydrogel enables sensitive NA detection. (A) Schematic of ITP-based hybridization enhancement. (B) Experimental images demonstrating ITP hydrogel capture. (C) Schematic of microRNA detection assay. Adopted with permission from G. Garcia-Schwarz and J. G. Santiago, Analytical Chemistry **84** (15), 6366-6369 (2012). Copyright 2012 American Chemical Society.

4.1.3 Electrokinetics with chemical and/or physical selectivity

The approaches discussed above exploit only differences in electrophoretic mobility in order to perform change in the sample in some way. Superimposable on these are a number of ways in which to alter the mobility of the target species through chemical interactions. Historically, the oldest is the use of pH to alter the ionization of weak acids, bases and ampholytes. Akin to IEF (which uses a shallow pH gradient to cause ampholytes to focus at discrete points), a 'dynamic pH junction', also called a moving neutralization boundary (MNB), is a step pH gradient to concentrate all target analytes at the boundary. In order to create the pH boundary, the sample should have a pH that is different from that of the separation electrolyte, so that the analytes of interest will slow down when reaching the BGE. Dynamic pH junction is very useful for on-line sample pretreatment of weakly ionized analytes in biological samples because it is tolerant of the salt concentration. Although the technique is often used for the analysis of complex samples in CE, its uptake at the microchip format has been limited.[24] More developments on this in the future are expected, as dynamic pH junction can benefit from the flexibility in microchip design and automation.

4.1.4 Nano-/micro-channel interfaces

Unique properties at nano-/micro-channel interfaces have created an array of options based on electrokinetic trapping. The mechanism is not fully understood but is expected to balance the electrophoretic, hydrodynamic, and EOF forces acting on the analyte (Figure 4.3). Through the combination of size exclusion and charge perm-selectivity, ions are selectively transported through the nanopore creating a charge imbalance, which is a phenomena known as ion concentration polarization (ICP). In order to preserve the electroneutrality on either side of the nanochannel, the transport

of cations is affected, resulting in the anions and cations being depleted on the anodic side of the nanopores while being enriched on the cathodic side. Factors including the applied field strength, surface charge and charge density, and fluid viscosity will affect the extent and rate of enrichment. The use of nanopores is of great interest because of the ease with which it can be integrated into a microdevice and its immense potential for sample preparation. For example, a concentration enhancement of more than a million-fold for fluorescent dyes from water has been reported using ICP.[4]

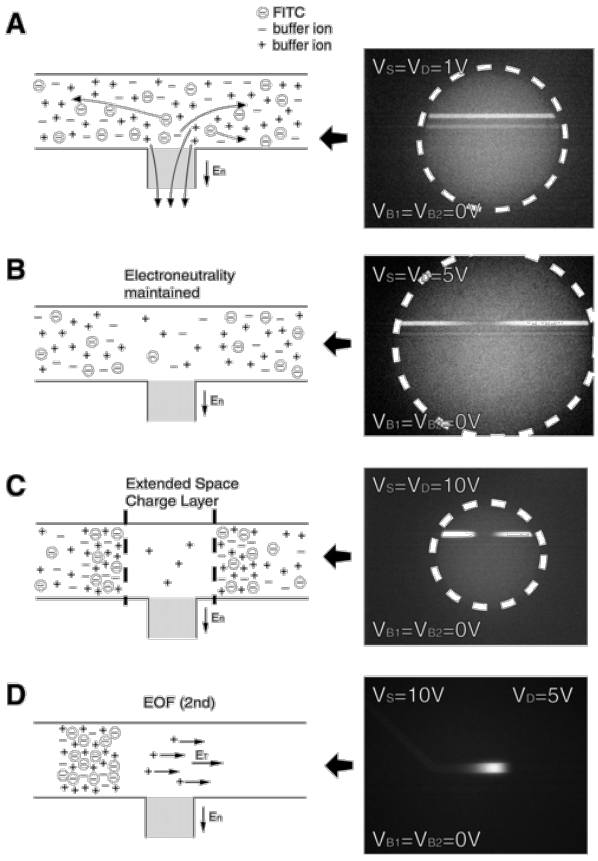

Figure 4.3 Mechanism of preconcentration in the nanofilter device (A) No concentration polarization is observed when a small electrical field (En) is applied across the nanofilter. (B) As the En increases, the transport of ions becomes diffusion-limited and generates the ion- depletion zone. However, the region maintains its electroneutrality. (C) Once a strong field (En) is applied; the nanochannel will develop an induced space charge layer, where electroneutrality is no longer maintained. (D) By applying an additional field (ET) along the microfluidic channel in the anodic side (from VS to VD), a nonlinear electrokinetic flow (called electroosmosis of the second kind) is induced, which results in fast accumulation of biomolecules in front of the induced space charge layer. Reprinted with permission from Y. C. Wang, A. L. Stevens and J. Han, Analytical Chemistry **77** (14), 4293-4299 (2005). Copyright 2005 American Chemical Society.

There are a number of ways in which nanopores can be incorporated into a microfluidic device. The first, and most obvious is through direct fabrication using e-beam lithography, which provides a great level of control of the size and shape of the nanochannels. Simultaneous concentration and separation of two proteins was achieved in a microfluidic device with a nanochannel of varying width by establishing low and high salt concentration at the nanochannel ends and creating a conductivity gradient.[25] Proteins were concentrated in different locations where their electrophoretic mobility was balanced with the EOF, reaching enhancements of 1000-fold within 17 min. The technique does not require EDL overlap and hence can tolerate high ionic strength samples. Another variation is depletion zone ITP, which combines ITP with ICP and the EOF in the microchannel balances the depletion zone created at the interface with the nanochannels.[26] Small fluorescent dyes and labelled amino acids were enriched within 100 s and the specific elution of analyte zones was achieved using non-fluorescent spacers. Because this mechanism relies on the extent of overlap of the double layer in the pores, this technique depends upon the ionic strength and the size of the nanopores. Protein trapping with nano/microchannel interface while continuously injecting the sample was achieved in 85-nm-deep nanochannels connecting two microchannels with different pH and filled with protein-buffer solution pumped at 1000 nL/min flow rate.[27] The low-pH microchannel was connected to the positive electrodes and the high-pH microchannels to the negative electrodes. Enhancements were 385-fold for R-Phycoerythrin within 10 min and 107-fold for Dylight-labelled streptavidin within 3 min. The selective enhancement factor for Dylight-labelled streptavidin was due to saturation of focusing as both proteins reach the same concentration in milligram per millilitres.

Widespread use of direct nanochannel fabrication is not common because of the expense of the infrastructure required to pattern the nanochannels and the difficulty in bonding. Another low cost approach uses HF etching of fused silica in order to create nanoporous junctions that can be used as filters or an ionic trap for concentration enhancement.[28] Over a billion-fold enhancement was reported for fluorescein using LIF detection. The etching process was stopped once a sudden current increase was observed across the junction, which prevents over-etching. Enrichment factors decrease significantly by increasing the ionic strength of the BGE due to thinner EDL. Only 50-fold enhancement was achieved for unlabelled DNA in 80 mM 2-(4-morpholino) ethanesulfonic acid (MES) - tris(hydroxymethyl)-aminomethane (Tris) buffer (pH 6.18) using UV detection. In addition, when using a fused silica capillary, labelled DNA was concentrated by 10^5-fold from a low ionic strength buffer after introducing a fracture in the capillary wall.[29]

The second way in which nanopores have been integrated into microfluidic devices is through the incorporation of a photopolymerized hydrogel, allowing the use of lithographic principles in order to accurately control the position of the hydrogel. The chemistry can be used to define the physical and chemical nature of the pores – the functional monomer(s) determine(s) the charge and surface charge density, while the pore size is controlled by the type and amount of cross-linker. For example, a hydrophilic hydrogel with sulfonic acid groups ($pK_a < 1$) was used to enrich fluorescein and tetramethylrhodamine isothiocyanate (TRITC)-tagged albumin by up to 1000-fold within 20 min from a sample matrix composed of 20 mM phosphate buffer and 45 mM KCl.[30] While relatively easy to make, the pore size within the hydrogel is not uniform, with a smaller pore size in the centre of the material than near the edge, which can lower their ability to offer high enhancement factors. In

addition, shrinking and swelling in response to changes in buffer ionic strength, temperature and other environmental factors may disrupt the ICP and diminish the achievable concentration enhancement factors, as these are usually accompanied with pore size changes. However, these phenomena may also be exploited, as shown by Li *et al*., who demonstrated the concentration and then elution of small molecules using a thermo-switchable hydrogel.[31] The hydrogel swells and becomes hydrophilic below approximately 32^{o}C, thereby forming nanopores, but shrinks and becomes hydrophobic above this temperature, allowing the transport of small molecules, such as fluorescein isothiocyanate (FITC) and labelled amino acids, through the hydrogel. These were concentrated 17- to 22-fold in 50 μM sodium tetraborate buffer within 3 min. Considering the dramatic deterioration of performance by increasing ionic strength to just 10 mM and the fact that physiological ionic strength is higher than 100 mM, it is clear that significant work is required on this approach for it to be widely applicable to biological fluids.

The third approach (the integration of a nanoporous membrane) allows for the incorporation of more defined nanopores, and has been realized by sandwiching a suitable membrane (such as a Nafion® membrane) between two microchips halves during bonding. Channel geometry has a similar effect to what was observed with ITP. Better enhancement can be achieved in convergent channels compared with straight channels and the concentration rate was significantly faster, 400-fold after 360 s as opposed to the 200-fold after 1200 s in straight channels.[32] The experiments were done using 10^{-7} M FITC-labelled BSA as model analyte.

Track-etched polycarbonate membrane was reported for the analysis of reduced glutathione directly from human plasma, without any off-chip deproteinization. By allowing the glutathione to diffuse through the membrane, it

could then be analysed by CE with fluorescence detection. The same chip was used to achieve 80-fold enhancement of DNA in less than 1 min by restricting DNA from passing through the membrane and concentrating on one side of the membrane.[33] In another approach, purification, desalting and concentration of DNA were simultaneously achieved in microchips using a capillary with two notches in the wall covered with conductive Nafion® membranes permeable to small ions, but not DNA.[34] The purified DNA was then released by switching off or reversing the electric field. A recovery of 95% was obtained from crude DNA sample. However, at the high ionic strengths of most biological samples, the membrane deforms and can rupture, which limits the achievable enhancement factors for biological samples. When cleaning and desalting the sample is a priority, as in MS detection, electrokinetic traps near a cation selective membrane could be more efficient than SPE in removing surfactants from trypticpeptides.[35] A poly- (tetrafluoroethylensulfonate) membrane was employed to desalt and clean positively charged peptides and proteins from surfactant before introducing them to MS detector. The membrane pore size was small enough to prevent the peptides and proteins that were trapped in the electric field from passing through, but allowed passage of salts and the surfactant 3-[(3-cholamidopropyl) dimethylammonio]-1-propanesulfonate (CHAPS).

The fourth alternative to create nanopores is through electric breakdown, forming microfissures and cracks by applying an electric field higher than the dielectric breakdown of the material. These microfissures and cracks were used to concentrate proteins by up to a million-fold;[4b] however, the lack of control over the resulting pore size limits the reproducibility of this approach. Recently, a method was developed to overcome this by monitoring the current during breakdown and down regulating the voltage when a specific current was reached. Setting a low threshold

current produced smaller pores, while larger pores could be achieved with higher thresholds.[36]

Sample desalting is especially important when MS detection is used and to improve the signal-to-noise ratio. Capacitive deionization using two porous electrodes on a chip enabled removal of 23% of sodium and chloride ions in the sample using low applied voltage (0.5 V).[37] Small ions migrated towards either electrode and participate in the EDL within the pores, while larger molecules such as FITC-dextran did not and remained in solution.

4.1.5 Conclusions

The increased interest in being able to perform laboratory quality measurements of biological samples on-site for POC personalized medicine has created a great need for efficient on-line sample pretreatment of complex samples. There is currently no universally applicable approach that can be used for all applications but there are many approaches that show great promise for specific applications. High sensitivity, high throughput, and high selectivity are the key points to consider but there are additional requirements of cost, simplicity and reliability. Research towards the development of new simple, sample preparation methods that can be easily integrated into a microchip is expected to grow exponentially, and because of the immense flexibility and simple hardware required electrokinetic methods will become increasingly prominent in future devices.

4.2 References

1. Llanes, L.; Ferruelo, A.; Lujan, M.; Pascual, C.; Garcia-Mediero, J. M.; Berenguer, A., Quantitative real-time reverse transcription: polymerase chain reaction of prostate-specific antigen (PSA) for detection of circulating prostatic cells in patients with clinically localized prostate cancer. *Prostate Cancer Prostatic Disease* **2005,** *8* (3), 248-252.
2. Potluri, S.; Ventura, H. O.; Mulumudi, M.; Mehra, M. R., Cardiac troponin levels in heart failure. *Cardiology in Review* **2004,** *12* (1), 21-25.
3. Jung, B.; Bharadwaj, R.; Santiago, J. G., On-chip millionfold sample stacking using transient isotachophoresis. *Analytical Chemistry* **2006,** *78* (7), 2319-2327.
4. (a) Wang, Y.-C.; Stevens, A. L.; Han, J., Million-fold preconcentration of proteins and peptides by nanofluidic filter. *Analytical Chemistry* **2005,** *77* (14), 4293-4299; (b) Kim, S. M.; Burns, M. A.; Hasselbrink, E. F., Electrokinetic protein preconcentration using a simple glass/poly(dimethylsiloxane) microfluidic chip. *Analytical Chemistry* **2006,** *78* (14), 4779-4785.
5. Wagli, P.; Chang, Y.-C.; Homsy, A.; Hvozdara, L.; Herzig, H. P.; de Rooij, N. F., Microfluidic droplet-based liquid−liquid extraction and on-chip IR spectroscopy detection of cocaine in human saliva. *Analytical Chemistry* **2013,** *85* (15), 7558-7565.
6. Helton, K. L.; Nelson, K. E.; Fu, E.; Yager, P., Conditioning saliva for use in a microfluidic biosensor. *Lab on a Chip* **2008,** *8* (11), 1847-1851.
7. Kamphorst, J. J.; Tjaden, U. R.; van der Heijden, R.; DeGroot, J.; van der Greef, J.; Hankemeier, T., Feasibility of electrodialysis as a fast and selective sample preparation method for the profiling of low-abundant peptides in biofluids. *Electrophoresis* **2009,** *30* (13), 2284-2292.

8. Weiss, D. J.; Saunders, K.; Lunte, C. E., pH-Mediated field-amplified sample stacking of pharmaceutical cations in high-ionic strength samples. *Electrophoresis* **2001,** *22* (1), 59-65.
9. Kim, D. K.; Kang, S. H., On-channel base stacking in microchip capillary gel electrophoresis for high-sensitivity DNA fragment analysis. *Journal of Chromatography A* **2005,** *1064* (1), 121-127.
10. Shiddiky, M. J. A.; Shim, Y. B., Trace analysis of DNA: Preconcentration, separation, and electrochemical detection in microchip electrophoresis using Au nanoparticles. *Analytical Chemistry* **2007,** *79* (10), 3724-3733.
11. Herr, A. E.; Molho, J. I.; Drouvalakis, K. A.; Mikkelsen, J. C.; Utz, P. J.; Santiago, J. G.; Kenny, T. W., On-chip coupling of isoelectric focusing and free solution electrophoresis for multidimensional separations. *Analytical Chemistry* **2003,** *75* (5), 1180-1187.
12. Han, J.; Singh, A. K., Rapid protein separations in ultra-short microchannels: Microchip sodium dodecyl sulfate-polyacrylamide gel electrophoresis and isoelectric focusing. *Journal of Chromatography A* **2004,** *1049* (1-2), 205-209.
13. Bahga, S. S.; Kaigala, G. V.; Bercovici, M.; Santiago, J. G., High-sensitivity detection using isotachophoresis with variable cross-section geometry. *Electrophoresis* **2011,** *32* (5), 563-572.
14. Bottenus, D.; Jubery, T. Z.; Dutta, P.; Ivory, C. F., 10000-fold concentration increase in proteins in a cascade microchip using anionic ITP by a 3-D numerical simulation with experimental results. *Electrophoresis* **2011,** *32* (5), 550-562.
15. Bottenus, D.; Jubery, T. Z.; Ouyang, Y.; Dong, W. J.; Dutta, P.; Ivory, C. F., 10000-fold concentration increase of the biomarker cardiac troponin I in a

reducing union microfluidic chip using cationic isotachophoresis. *Lab on a Chip* **2011,** *11* (5), 890-898.

16. Bottenus, D.; Hossan, M. R.; Ouyang, Y.; Dong, W. J.; Dutta, P.; Ivory, C. F., Preconcentration and detection of the phosphorylated forms of cardiac troponin i in a cascade microchip by cationic isotachophoresis. *Lab on a Chip* **2011,** *11* (22), 3793-3801.

17. Schoch, R. B.; Ronaghi, M.; Santiago, J. G., Rapid and selective extraction, isolation, preconcentration, and quantitation of small RNAs from cell lysate using on-chip isotachophoresis. *Lab on a Chip* **2009,** *9* (15), 2145-2152.

18. Liu, D.; Ou, Z.; Xu, M.; Wang, L., Simplified transient isotachophoresis/capillary gel electrophoresis method for highly sensitive analysis of polymerase chain reaction samples on a microchip with laser-induced fluorescence detection. *Journal of Chromatography A* **2008,** *1214* (1-2), 165-170.

19. Wu, R.; Wang, Z.; Zhao, W.; Yeung, W. S.-B.; Fung, Y. S., Multi-dimension microchip-capillary electrophoresis device for determination of functional proteins in infant milk formula. *Journal of Chromatography A* **2013,** *1304* (0), 220-226.

20. Wu, R.; Yeung, W. S. B.; Fung, Y. S., 2-D t-ITP/CZE determination of clinical urinary proteins using a microfluidic-chip capillary electrophoresis device. *Electrophoresis* **2011,** *32* (23), 3406-3414.

21. Wainright, A.; Williams, S. J.; Ciambrone, G.; Xue, Q.; Wei, J.; Harris, D., Sample pre-concentration by isotachophoresis in microfluidic devices. *Journal of Chromatography A* **2002,** *979* (1,Äì2), 69-80.

22. Liu, D.; Shi, M.; Huang, H.; Long, Z.; Zhou, X.; Qin, J.; Lin, B., Isotachophoresis preconcentration integrated microfluidic chip for highly sensitive

genotyping of the hepatitis B virus. *Journal of Chromatography B* **2006,** *844* (1), 32-38.

23. (a) Rogacs, A.; Qu, Y.; Santiago, J. G., Bacterial RNA extraction and purification from whole human blood using isotachophoresis. *Analytical Chemistry* **2012,** *84* (14), 5858-5863; (b) Bercovici, M.; Kaigala, G. V.; MacH, K. E.; Han, C. M.; Liao, J. C.; Santiago, J. G., Rapid detection of urinary tract infections using isotachophoresis and molecular beacons. *Analytical Chemistry* **2011,** *83* (11), 4110-4117; (c) Garcia-Schwarz, G.; Santiago, J. G., Integration of on-chip isotachophoresis and functionalized hydrogels for enhanced-sensitivity nucleic acid detection. *Analytical Chemistry* **2012,** *84* (15), 6366-6369; (d) Eid, C.; Garcia-Schwarz, G.; Santiago, J. G., Isotachophoresis with ionic spacer and two-stage separation for high sensitivity DNA hybridization assay. *Analyst* **2013,** *138* (11), 3117-3120.

24. Kazarian, A. A.; Hilder, E. F.; Breadmore, M. C., Online sample pre-concentration via dynamic pH junction in capillary and microchip electrophoresis. *Journal of Separation Science* **2011,** *34* (20), 2800-2821.

25. Inglis, D. W.; Goldys, E. M.; Calander, N. P., Simultaneous concentration and separation of proteins in a nanochannel. *Angewandte Chemie International Edition* **2011,** *50* (33), 7546-7550.

26. Quist, J.; Janssen, K. G. H.; Vulto, P.; Hankemeier, T.; Van Der Linden, H. J., Single-electrolyte isotachophoresis using a nanochannel-induced depletion zone. *Analytical Chemistry* **2011,** *83* (20), 7910-7915.

27. Startsev, M. A.; Inglis, D. W.; Baker, M. S.; Goldys, E. M., Nanochannel pH gradient electrofocusing of proteins. *Analytical Chemistry* **2013,** *85* (15), 7133-7138.

28. Wu, Z. Y.; Fang, F.; He, Y. Q.; Li, T. T.; Li, J. J.; Tian, L., Flexible and efficient eletrokinetic stacking of DNA and proteins at an HF etched porous junction on a fused silica capillary. *Analytical Chemistry* **2012,** *84* (16), 7085-7091.

29. Wu, Z. Y.; Li, C. Y.; Guo, X. L.; Li, B.; Zhang, D. W.; Xu, Y.; Fang, F., Nanofracture on fused silica microchannel for Donnan exclusion based electrokinetic stacking of biomolecules. *Lab on a Chip* **2012,** *12* (18), 3408-3412.

30. Chun, H.; Chung, T. D.; Ramsey, J. M., High yield sample preconcentration using a highly ion-conductive charge-selective polymer. *Analytical Chemistry* **2010,** *82* (14), 6287-6292.

31. Li, Z.; He, Q.; Ma, D.; Chen, H.; Soper, S. A., Thermoswitchable electrokinetic ion-enrichment/elution based on a poly(N-isopropylacrylamide) hydrogel plug in a microchannel. *Analytical Chemistry* **2010,** *82* (24), 10030-10036.

32. Chao, C.-C.; Chiu, P.-H.; Yang, R.-J., Preconcentration of diluted biochemical samples using microchannel with integrated nanoscale Nafion membrane. *Biomedical Microdevices* **2015,** *17* (2), 1-9.

33. Long, Z.; Liu, D.; Ye, N.; Qin, J.; Lin, B., Integration of nanoporous membranes for sample filtration/preconcentration in microchip electrophoresis. *Electrophoresis* **2006,** *27* (24), 4927-4934.

34. Park, S.-R.; Swerdlow, H., Concentration of DNA in a flowing stream for high-sensitivity capillary electrophoresis. *Analytical Chemistry* **2003,** *75* (17), 4467-4474.

35. Astorga-Wells, J.; Jörnvall, H.; Bergman, T., A Microfluidic electrocapture device in sample preparation for protein analysis by MALDI mass spectrometry. *Analytical Chemistry* **2003,** *75* (19), 5213-5219.

36. Shallan, A. I.; Gaudry, A. J.; Guijt, R. M.; Breadmore, M. C., Tuneable nanochannel formation for sample-in/answer-out devices. *Chemical Communications* **2013,** *49* (27), 2816-2818.

37. Roelofs, S. H.; Kim, B.; Eijkel, J. C. T.; Han, J.; van den Berg, A.; Odijk, M., Capacitive deionization on-chip as a method for microfluidic sample preparation. *Lab on a Chip* **2015,** *15* (6), 1458-1464.

5 Sample Preparation for Biopolymers - Nanojunctions

5.1 Concentrating SDS-proteins from High Ionic Strength Solutions

Protein biomarkers for early diagnosis and management of different disease states are the target analyte for many POC devices currently available on the market. Proteins can reveal information that cannot be predicted from DNA sequence, shifting the interest from genomics to proteomics and metabolomics. The majority of these devices are based on immunoassays to detect very low concentrations of a specific protein. In this section, nanojunctions for concentrating SDS-proteins from high ionic strength buffers by up to 80-fold are presented.

5.1.1 Microfluidic Device and Nanojunction Formation

The microfluidic device is hybrid PDMS/glass with the single nanojunction design previously described in Chapter One. The breakdown electrolyte was 50 mM KCl and the dedicated power supply cuts the applied voltage once a pre-set current is reached through the formed nanojunction. The voltage was applied to the V-channel while keeping the separation channel ground. The PDMS breakdown was done in two steps; first, 2200 V was ramped for 10 s while setting the current limit at 3.0 μA, then the polarity was reversed. All five devices tested showed a current of 30-40 nA when a 100 V was applied across the nanojunction.

5.1.2 Enrichment and Separation

After the formation of the nanojunction, the breakdown electrolyte was replaced with the appropriate buffers and sample as shown in Figure 5.1.

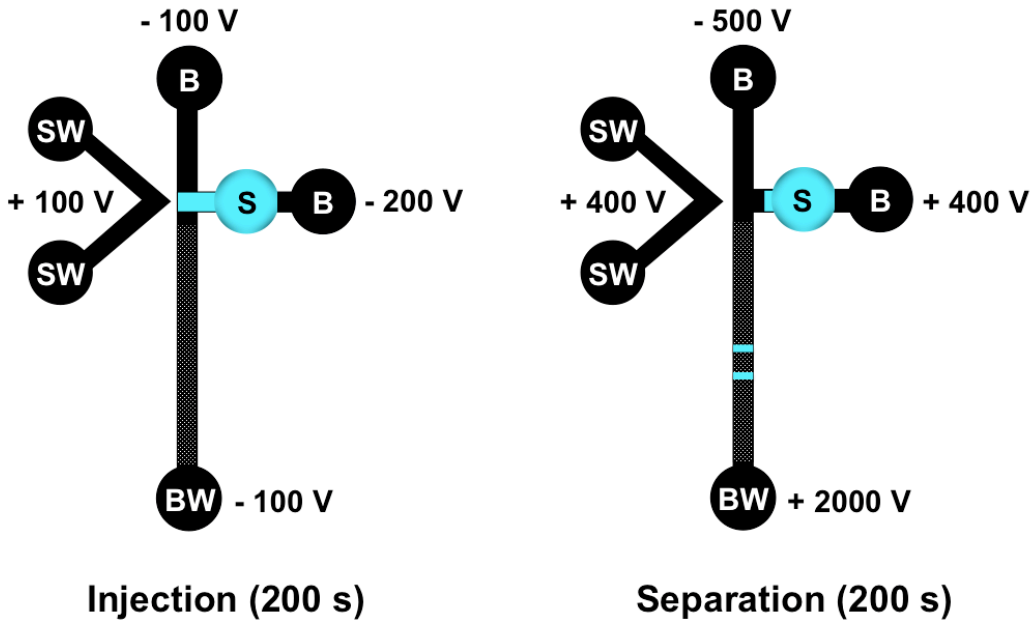

Figure 5.1 Experimental conditions for SDS-protein concentration and separation. Buffer (B) was 100 mM Tris-phosphate (pH 8.3), 0.1% SDS and 10% glycerol. Sieving matrix, POP^{TM}, was added to the buffer (1:3) in the separation channel connecting the injection point to the buffer waste (BW). The sample waste (SW) V-channel was filled with 50 mM Tris-HCl (pH 6.8) with 2.5% HPMC. An extra reservoir (S) was filled with fluorescamine labelled SDS-protein.

Protein labelling and denaturing: Individual protein solutions were prepared: Insulin (5.8 kDa, pI = 5.3) at 5 mg/mL in 50 mM $NaHCO_3$, Apotransferrin (78 kDa, pI = 6.1) at 10 mg/mL in water, β-lactoglobulin (18.4 kDa, pI = 5.1) at 10 mg/mL in water, ovalbumin (44.3 kDa, pI = 4.54, 4.9) at 20 mg/mL in water, and BSA (66.4 kDa, pI = 4.7, 4.9) at 20 mg/mL in water.

In individual vials, 20 μL of each protein solution (40 μL for insulin) were mixed with 120 μL (60 μL for insulin) of 100 mM $NaHCO_3$, and then labelled with 60 μL (30 μL for insulin) freshly prepared fluorescamine (3 mg/mL in acetone).

Equal volumes of the labelled protein and SDS sample buffer were mixed then heated to 100^{o}C using a heating block for 6 min. The SDS sample buffer was 100 mM Tris, 2% SDS, 4% Dithioerythritol (DTT), and pH adjusted to 6.8 with HCl.

Each solution was diluted to the desired concentration with buffer (100 mM Tris-phosphate, pH 8.3, 0.1% SDS and 10% glycerol).

Applied electric field: Injection voltage was maintained for 200 s to extract and concentrate the SDS-protein then the power supply was switched to apply the separation voltage.

Detection: Experiments were visually recorded with a high-definition colour CCD camera head mounted on an inverted fluorescence microscope fitted with excitation and emission filters (λ_{ex} at 380-420 nm and λ_{em} at 450 nm). Quantitative measurements were done using a PMT. More details can be found in Chapter One and in the Appendix under Detection.

5.1.3 Results and Discussion

Labelled proteins were denatured with DTT and SDS. The running buffer also contained DTT and SDS at lower concentration than the SDS sample buffer to ensure that the proteins are in micelle form. POP^{TM} is a linear polyacrylamide polymer and was employed as a sieving matrix for size-based separation of the proteins. It also suppresses the EOF in order to achieve a stable stacking at the nanojunction.

The nanojunction was created with pore size that will allow current and small molecules through but not the proteins. Being negatively charged, the proteins migrate towards the anode till they are stopped by the nanojunction. Figure 5.2 shows the stacking of insulin during the injection phase. Insulin is excluded from entering the pores of the nanojunction because of its large size compared to the free transport region inside the pores and its negative charge.

The highest enrichment was achieved after applying the injection voltage for 200 s (Figure 5.3). In this case, SDS-insulin required 100 s to migrate from the reservoir and reach the nanojunction interface. Enrichment increases with time till a certain point when ICP evolves and the associated instability disperses the concentrated plug. The formation of depletion zones on the anodic side of the nanojunction displaced the concentrated plug. Also, for longer injection times, chaotic mixing was observed.

An enhancement factor of 80-fold for SDS-insulin was achieved as compared with standard pinched injection (Figure 5.4). SDS-apotransferrin showed only a 7-fold enhancement and the broadening of its peak and shift in migration time indicate its analysis was compromised by non-specific adsorption to PDMS (Figure 5.5).

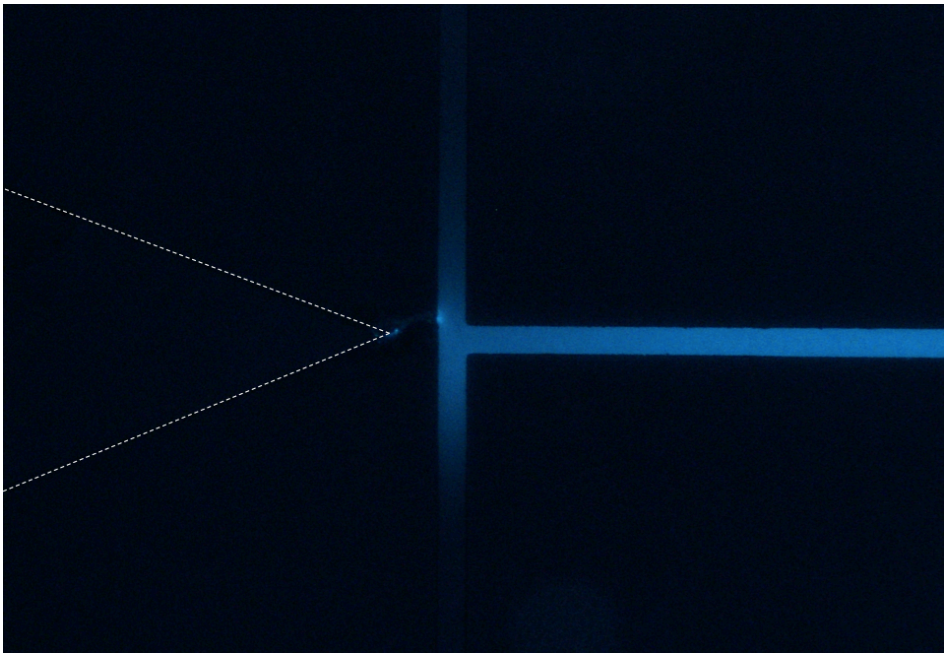

Figure 5.2 Stacking of fluorescamine-labelled SDS-insulin at the nanojunction interface during the injection phase.

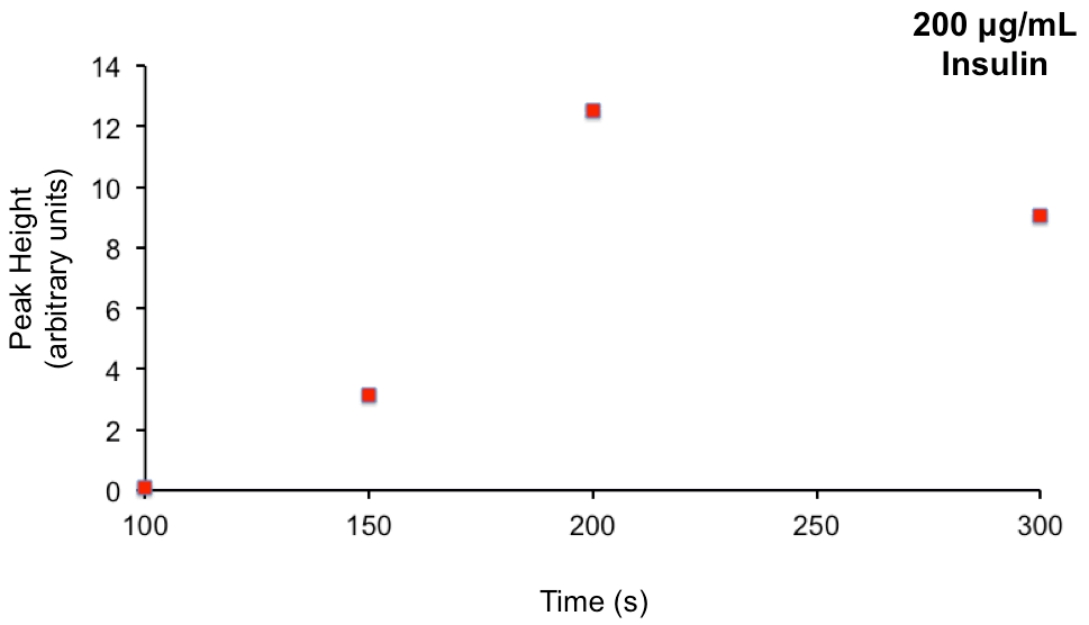

Figure 5.3 Effect of injection time on the peak height of the concentrated protein.

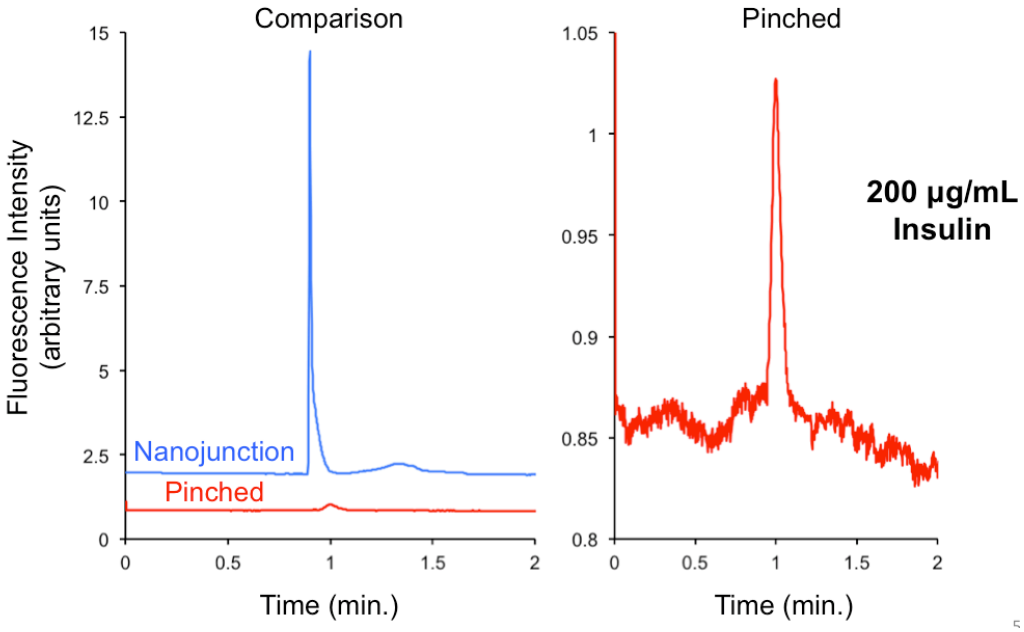

Figure 5.4 80-fold enrichment of SDS-insulin at the nanojunction (blue trace) as compared with standard pinched injection (red trace, zoom-in on the right).

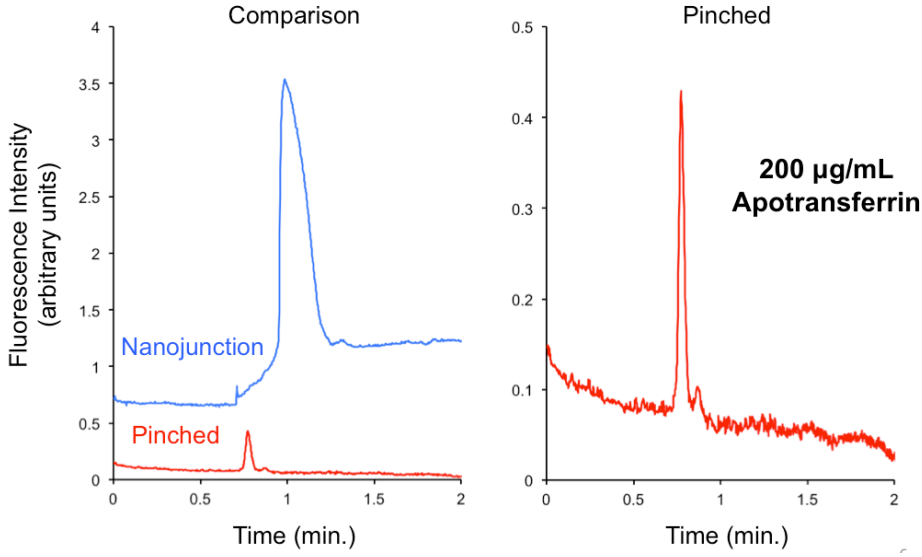

Figure 5.5 7-fold enrichment of SDS-apotransferrin at the nanojunction (blue trace) as compared with standard pinched injection (red trace, zoom-in on the right).

Non-specific adsorption of macromolecules can be minimized by surface coating. Diethoxy (3-glycidyloxy propyl) methyl silane (DGPMS) was employed for permanent coating of PDMS/glass channels after cleaning with air plasma. The coating procedure is very simple; the reagent is mixed with acetone in 1:1 ratio and used to flush the plasma-cleaned channels for 30 minutes.

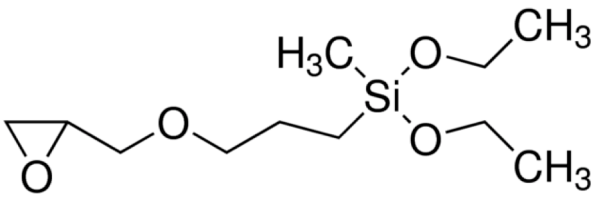

Diethoxy (3-glycidyloxy propyl) methyl silane

Size-based separation of 4 proteins was achieved using pinched injection on the coated chip with no apparent adsorption (Figure 5.6). For this separation, the buffer concentration was decreased to 50 mM Tris-phospahte to enable a higher SDS concentration of 30 mM and ensure that all the proteins will be included within micelles. Unfortunately, the coating procedure modified the PDMS and compromised the formation of the nanojunction. Alternative coating methods without solvents that swell PDMS will not affect the binding to the glass and may solve this problem.

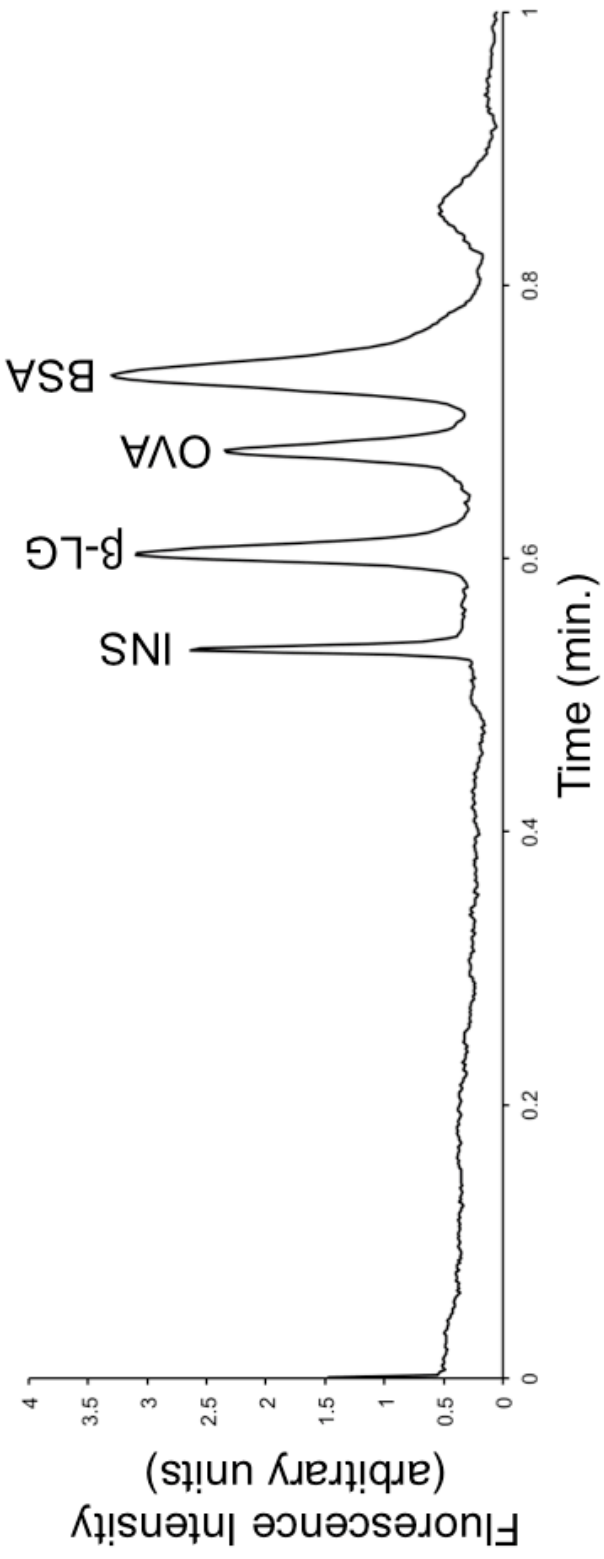

Figure 5.6 Electropherogram of the size-based separation of 4 SDS-proteins; insulin (INS), β-lactoglobulin (β-LG), ovalbumin (OVA) and bovine serum albumin (BSA) at concentrations of 9.4, 12.5, 12.5 and 50 µg/mL.

5.2 Extraction, Enrichment and Desalting of Short ssDNA from Blood

Certain gene mutations are linked to susceptibility to certain types of cancer. Women carrying genetic mutations in BRCA1 and BRCA2 are at high risk of ovarian and breast cancer and early intervention will greatly increase their survival chances. Short DNA and microRNA are increasingly reported as valuable diagnostic tools for different types of cancer. In this study, the SMTs were used to extract, concentrate and desalt DNA from blood followed by electrophoretic separation. The method is simpler and faster than SPE methods commonly used for extracting DNA from biological samples.

5.2.1 Microfluidic Device and Nanojunction Formation

The device is a hybrid PDMS/glass with the SMT design and the breakdown conditions are the same as described before in Chapter One for SMTs except that the breakdown electrolyte used here was 50 mM KCl.

5.2.2 Extraction, Enrichment and Desalting

After the formation of the nanojunctions, the breakdown electrolyte was replaced with the appropriate buffers and sample as shown in Figure 5.7.

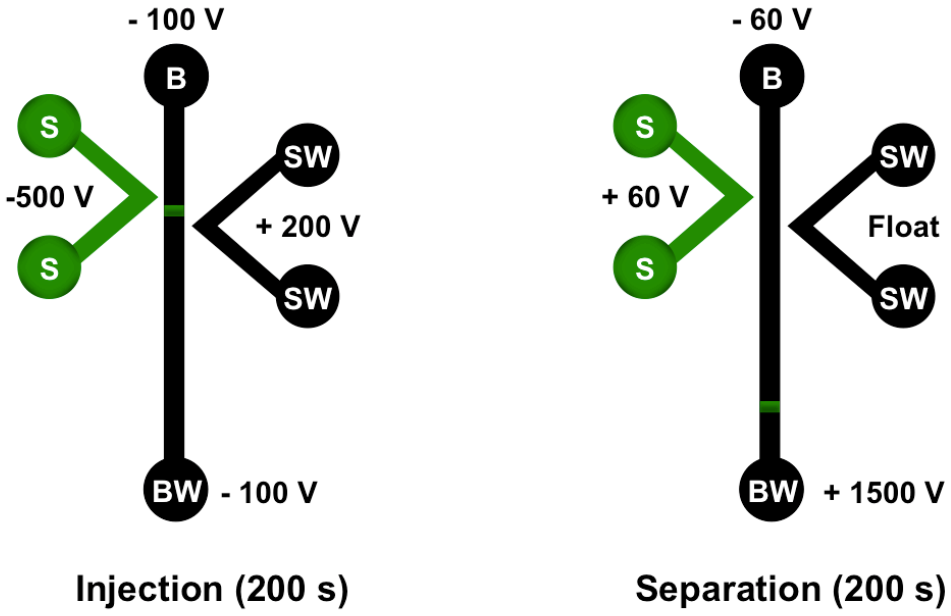

Figure 5.7 Experimental conditions for DNA extraction, concentration and desalting. The sample V-channel (S) capacity is 40 μL. Buffer (B) was 100 mM phosphate buffer (pH 6.8) with 0.5% HPMC to suppress the EOF. The sample waste (SW) V-channel was filled with 10 mM phosphate buffer (pH 6.8). Injection voltage was applied for 200 s to extract, concentrate and desalt the injected plug then the voltage was switched to separation.

Short ssDNA: Stock solution of 5 μM fluorescein-labelled ssDNA, in 10 mM Tris-HCl buffer (pH 8.0), was diluted as necessary for each experiment.

BGE system: The separation channel was filled with 100 mM phosphate buffer, pH 6.8, and 0.5% HPMC whilst the waste V-channel was filled with 10 mM phosphate buffer, pH 6.8.

Applied electric field: Injection voltage was maintained for 200 s to extract, concentrate and desalt the DNA then the voltage was switched for separation.

Detection: Experiments were visually recorded with a high-definition colour CCD camera head mounted on an inverted fluorescence microscope fitted with excitation and emission filters (λ_{ex} at 450-490 nm and λ_{em} at 520 nm). Quantitative measurements were done using a PMT. More details can be found in Chapter One and in the Appendix under Detection.

5.2.3 Results and Discussion

Despite the high molecular weight of DNA relative to small molecules, its unique ability to unfold and migrate through nanochannels can be useful for its extraction from biological matrices. Using SMT described in Chapter One, fluorescein-labelled short ssDNA (20 bases) behaved similar to fluorescein. DNA could be transported through the extraction nanojunction into the separation channel while proteins and cells were excluded. The purification nanojunction blocked the transport of DNA, hence enriching and desalting the injected plug. The EOF from the purification nanojunction counteracts the electrophoretic mobility of DNA and the injected plug is trapped at a certain location between the two nanojunctions as shown in Figure 5.8.

As stated before, high ionic strength of the matrix will decrease the transport through the nanojunction as the concentration difference is decreased, as illustrated in Figure 5.8 and Figure 5.9. This will affect the sensitivity when extracting from biological samples like blood. A 10-fold increase of matrix ionic strength from 10 mM to 100 mM phosphate buffer resulted in at least a 30-fold decrease in the injected amount of ssDNA (Figure 5.10). The peak height for ssDNA extracted from a 100 mM phosphate buffer was similar to that extracted from blood assuming similar ionic strength, but the peak obtained for the buffer was sharper. The minimum concentration of ssDNA that could be directly extracted from blood and detected quantitatively using the described method (S/N = 10) was 12.5 nM equivalent to 83 ng/mL (Figure 5.11). These limits still need to be improved as the detection limits reported for diagnostic microRNA were 0.5 pM.[1] Bidirectional ITP reported by the Santiago group reached a detection limit of 5 pM within 3 min for 39 bases ssDNA.[2]

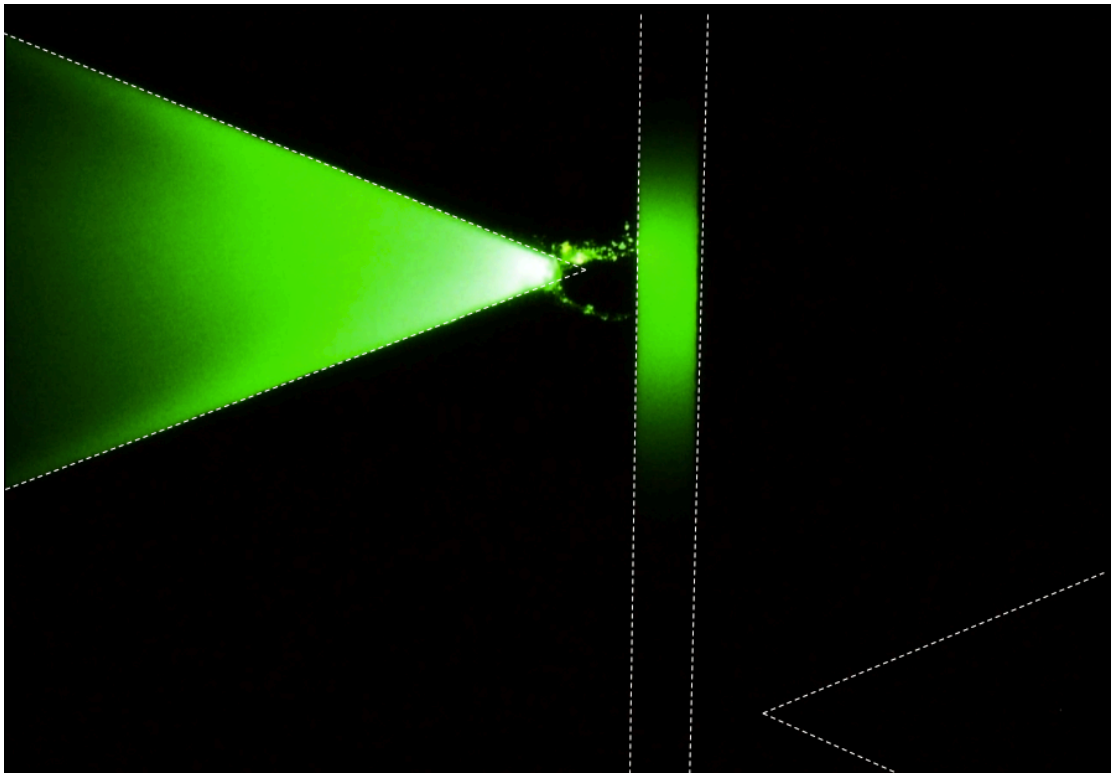

Figure 5.8 Fluorescence microscope screenshot of the injected fluorescein-labelled ssDNA plug. Initial concentration of the sample was 50 nM (by diluting the stock solution 100 times with water). BGE in the separation channel was 100 mM phosphate buffer, pH 6.5, with 0.5% HPMC to suppress the EOF. The sample waste V-channel on the right was filled with 10 mM phosphate buffer, pH 6.5.

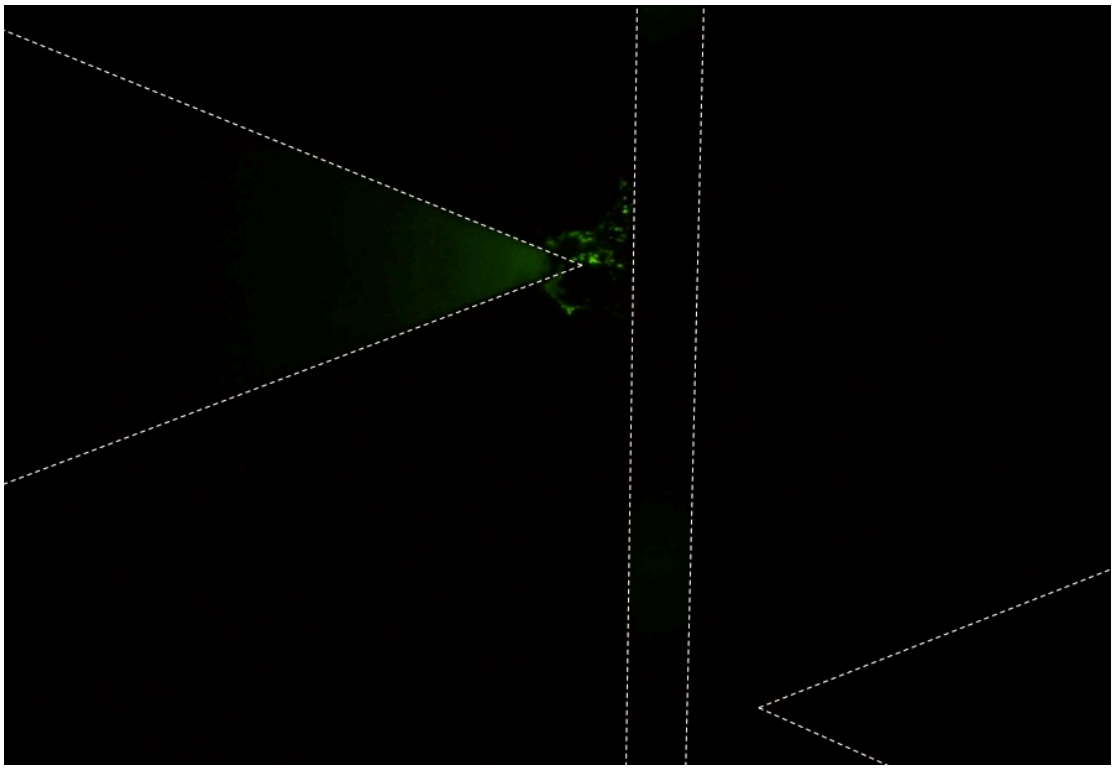

Figure 5.9 Fluorescence microscope screenshot of the injected fluorescein-labelled ssDNA plug. All conditions are similar to Figure 5.8 except that the stock dilution was made in 10 mM phosphate buffer, pH 6.5.

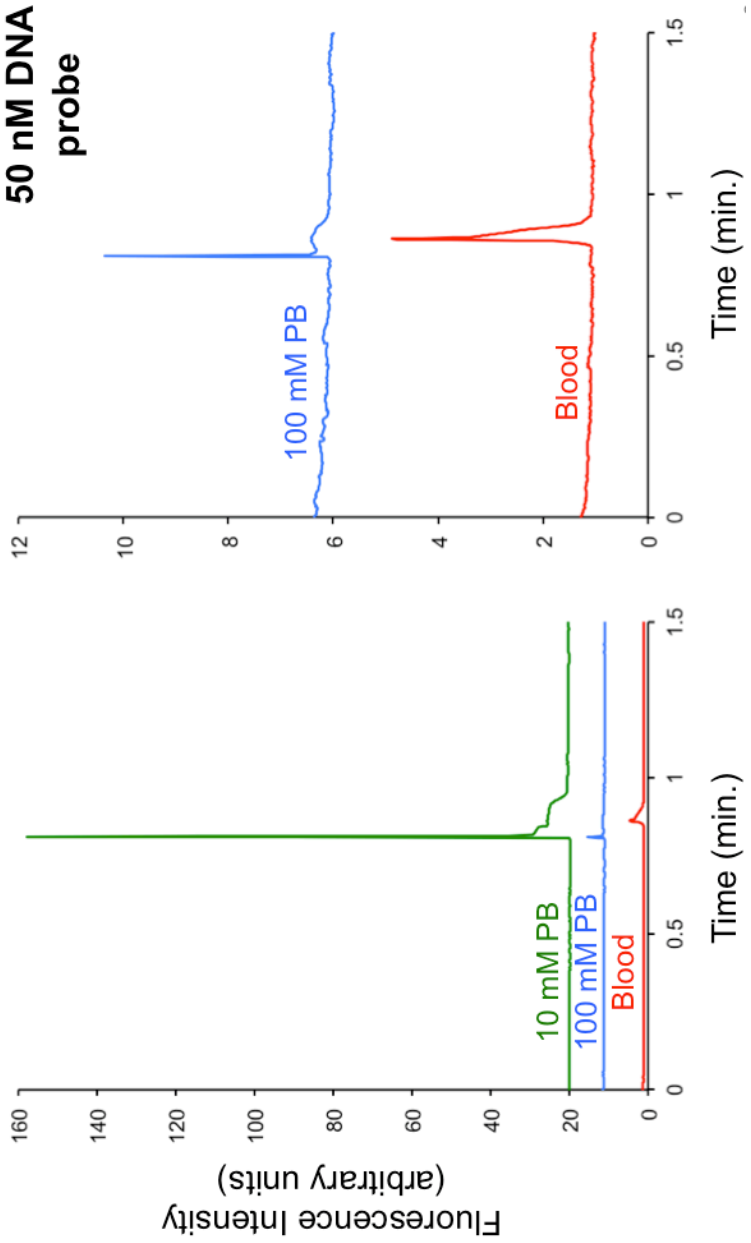

Figure 5.10 Effect of sample matrix. Electropherograms of 50 nM DNA injected from different sample matrices (10 mM phosphate buffer, 100 mM phosphate buffer and blood).

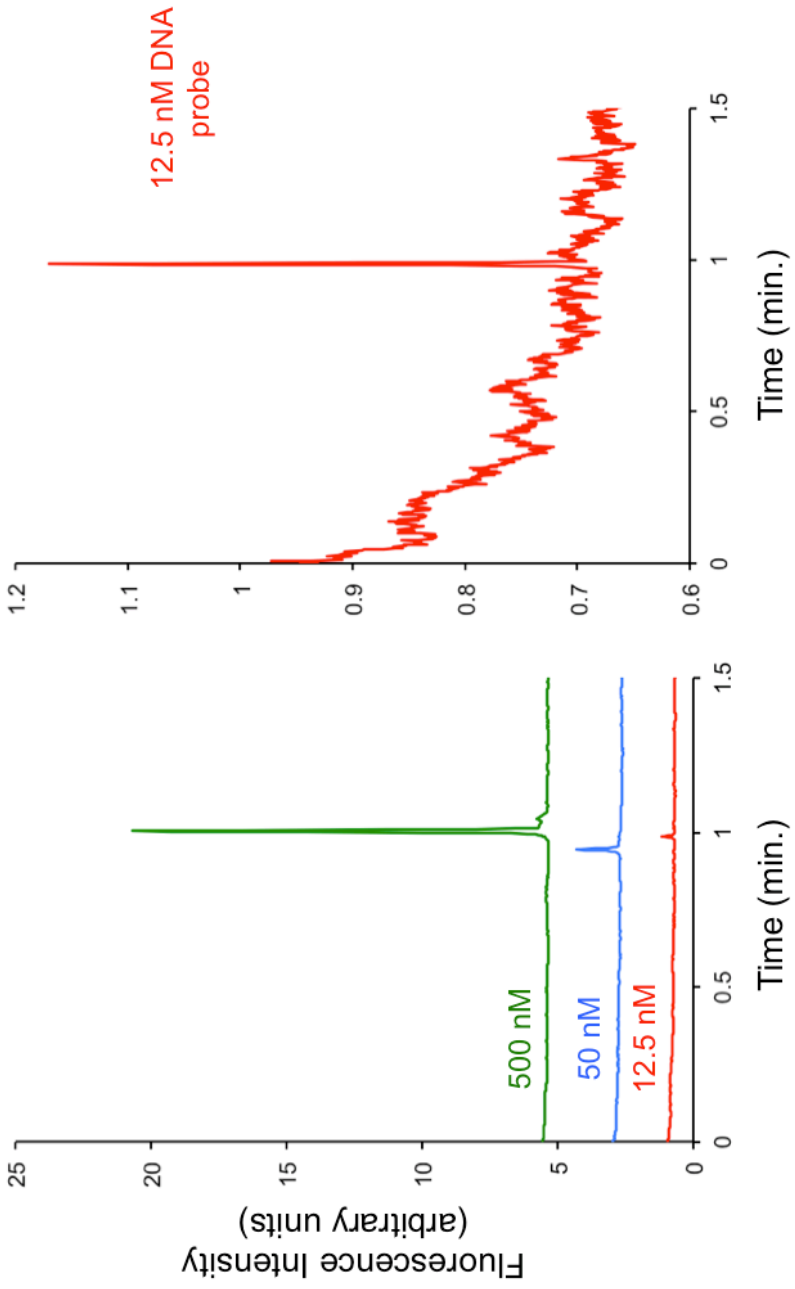

Figure 5.11 Electropherograms for DNA in blood at different concentrations (12.5, 50 and 500 nM). The scale for the electropherogram on the right was adjusted to focus on the lowest DNA concentration that can be detected quantitatively.

5.3 Conclusions

In this chapter, methods were presented for biological sample pretreatment based on nanojunctions made by dielectric breakdown of PDMS. Negatively charged analytes of different size were employed to demonstrate the wide range of applications that can be achieved using our method.

SDS-protein complexes were concentrated by up to 80-fold using a single nanojunction. The proteins were restricted from passing through the nanojunction because their size was larger than the free transport region within the pores of the nanojunction. Being negatively charged, they cannot participate in the EDL. The pore size of the nanojunction was small enough to physically block the proteins even at high ionic strength BGE where the EDL is compressed. The enriched proteins were subjected to size-based separation using a sieving matrix. Although non-specific binding compromised the separation efficiency, the use of coating procedures that does not cause PDMS to swell may solve the problem.

The SMTs enabled the seamless extraction, concentration and desalting of short ssDNA (20 bases). The sample pretreatment steps were done simultaneously and coupled with electrophoretic separation. The simple fabrication of the SMTs offers many advantages over the most common method, SPE. The SMTs do not require extra fabrication steps to incorporate the extraction bed and avoid the multiple washing steps.

The methods presented in this chapter offer simple and low cost nanofabrication options that enable on-chip sample pretreatment. This may open the way for the wide spread use of diagnostic POC devices.

5.4 References

1. Arata, H.; Komatsu, H.; Hosokawa, K.; Maeda, M., Rapid and sensitive microRNA detection with laminar flow-assisted dendritic amplification on power-free microfluidic chip. *PLOS one* **2012,** *7* (11), e48329.
2. Bahga, S. S.; Han, C. M.; Santiago, J. G., Integration of rapid DNA hybridization and capillary zone electrophoresis using bidirectional isotachophoresis. *Analyst* **2013,** *138* (1), 87-90.

Chapter Six

3D-Printing - Introduction and Its Potential for On-site Environmental Analysis

---

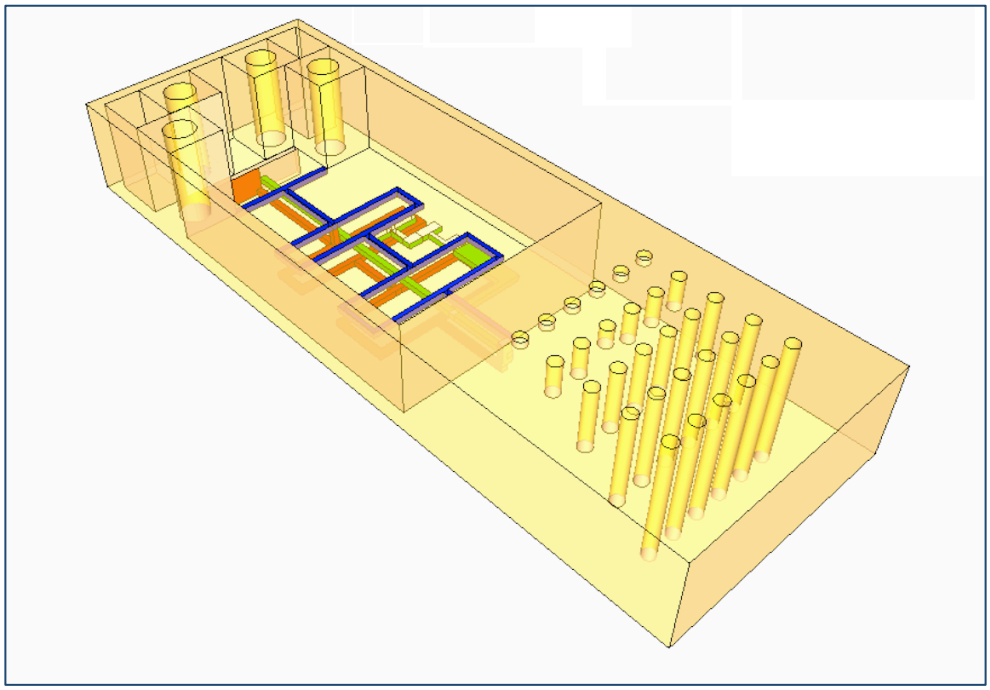

6 3D-Printing - Introduction and Its Potential for On-site Environmental Analysis

6.1 3D-Printing as Fast Prototyping Tool

Design and development of an environmental monitoring device is a dynamic process requiring integration of multiple analytical steps, testing and re-designing cycles. In this case, one-step manufacturing techniques are favoured over conventional approaches to shorten the time between these steps, accelerate the development and enhance the quality of the end product.[1]

Conventional photolithographic methods struggle with 3D designs, as accurate alignment and bonding of several layers are crucial to realize the 3D structure. The ability to transform digital designs directly into physical models, without the need for masks, will not only accelerate the fabrication process but also make practical evaluation of different designs faster and easier.

3D manufacturing techniques can be subtractive through removal of material with techniques such as femtosecond laser direct writing,[2] or additive through techniques such as fused deposition modelling (FDM)[3] or photofabrication.[4] Additive methods in particular have rapidly improved in performance and decreased in cost over the past decade making them more widely accessible, and there are now a number of different approaches and materials that can be used.[5] The resolution is still an issue especially that the stated resolution is usually better than the actual resolution of the printed object due to difficulties in removing the support material or the uncured resin. The following sections describe the most common methods of additive manufacturing and some chemical analysis applications using 3D printing.

6.1.1 Fused Deposition Modelling (FDM)

FDM employs a heated nozzle to extrude a thermoplastic polymer filament that solidifies forming structures (Figure 6.1). Surface defects and incomplete binding between the solidified filament parts are the main disadvantages. McDonald *et al*. were the first to print templates for casting polydimethylsiloxane (PDMS) and microchip interfaces using the FDM-based Thermojet printer.[3a] Also FDM-based, the Dimension SST 768 and 3DTouch were used for printing centrifugal devices with 254 μm × 254 μm capillary valves[3b] and reaction ware with 800 μm diameter channels,[3c, 3d] respectively. Because of the way it operates, fabrication of sealed monolithic reactors with different shapes and geometry was possible.[6] Printing could also be stopped halfway, the reactor filled with a solid reagent, then printing resumed to seal the reactor.

FDM resolution is defined by nozzle size, polymer properties upon extrusion and the speed at which the stage moves, currently resulting in a minimal feature size of 250 μm and a surface roughness of ≈8 μm. Printing closed channels is still limited to dimensions in the millimeter range as flushing the support material is more difficult in narrower channels. Printing without the supporting material is limited to designs devoid of large enclosed structures like fittings and accessory parts.[7]

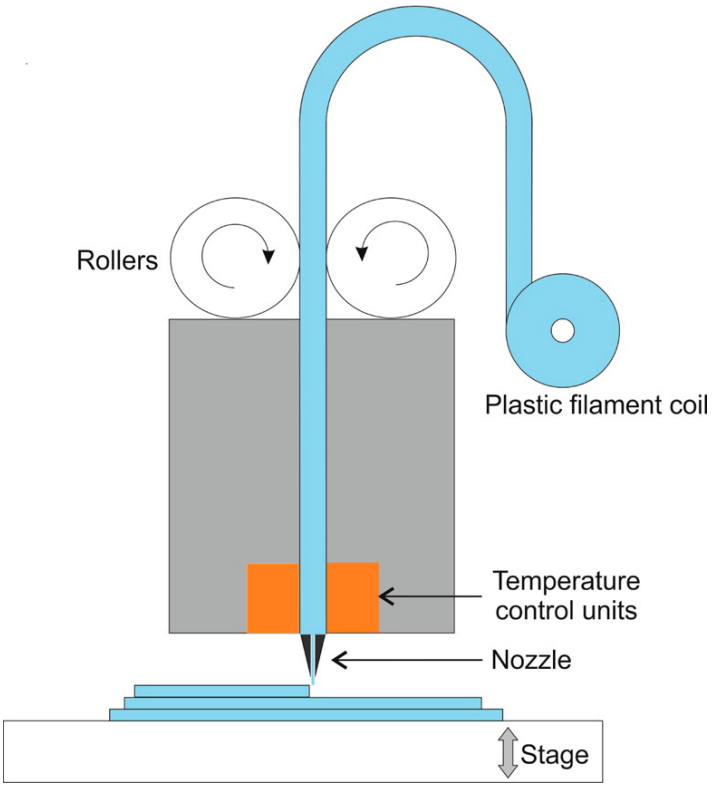

Figure 6.1 Schematic of an FDM 3D printer. In this method, plastic filament is directed into a heating block where it is heated to a semimolten state. The molten material can be printed onto an adjustable stage to form a layer of the desired object. The stage is adjusted (lowered) and another semimolten layer is printed. "Reprinted with permission from Gross, B. C.; Erkal, J. L.; Lockwood, S. Y.; Chen, C.; Spence, D. M., Evaluation of 3D Printing and Its Potential Impact on Biotechnology and the Chemical Sciences. *Analytical Chemistry* **2014,** *86* (7), 3240-3253. Copyright (2014) American Chemical Society."

6.1.2 Stereolithography (SL)

Photofabrication or "stereolithography" (SL) is perhaps the oldest and most well known additive fabrication method.[5c, 8] The first SL system used a computer-controlled focused laser beam to polymerize resin using the vector approach (point-to-point line drawn in three dimensions), and the stage moves down after one layer is traced by the laser (Figure 6.2A). This approach is sometimes referred to as the "bath configuration" and was first presented in 1986 and commercialized in 1988.[4a] Ikuta *et al.* employed focused laser to cure highly viscous UV photopolymer at pinpoint spot in the 3D space.[9] The cured resin did not sink due to the high viscosity of the resin alleviating the need to use supporting material and enabling the fabrication of freely moving 3D micro objects.

The work done by Nakamoto *et al.*[10] on mask-based photopolymerization of entire layers has inspired the development of printers employing dynamic digital masks for layer-by-layer projection, also referred to as the "layer configuration" (Figure 6.2B). This approach is faster, cheaper, and more robust than the vector-based printing, as only one translational stage (the Z axis) is required. Also, lasers can be substituted with less expensive components. Digital masks are currently generated using a liquid crystal display (LCD),[11] a digital micromirror device (DMD),[12] or a liquid crystal on silicon (LCoS).[13]

In the last few years, desktop SL printers became increasingly available from different manufacturers at relatively low prices and adequate resolution. Table 6.1 summarizes the different commercially available SL printers.[14]

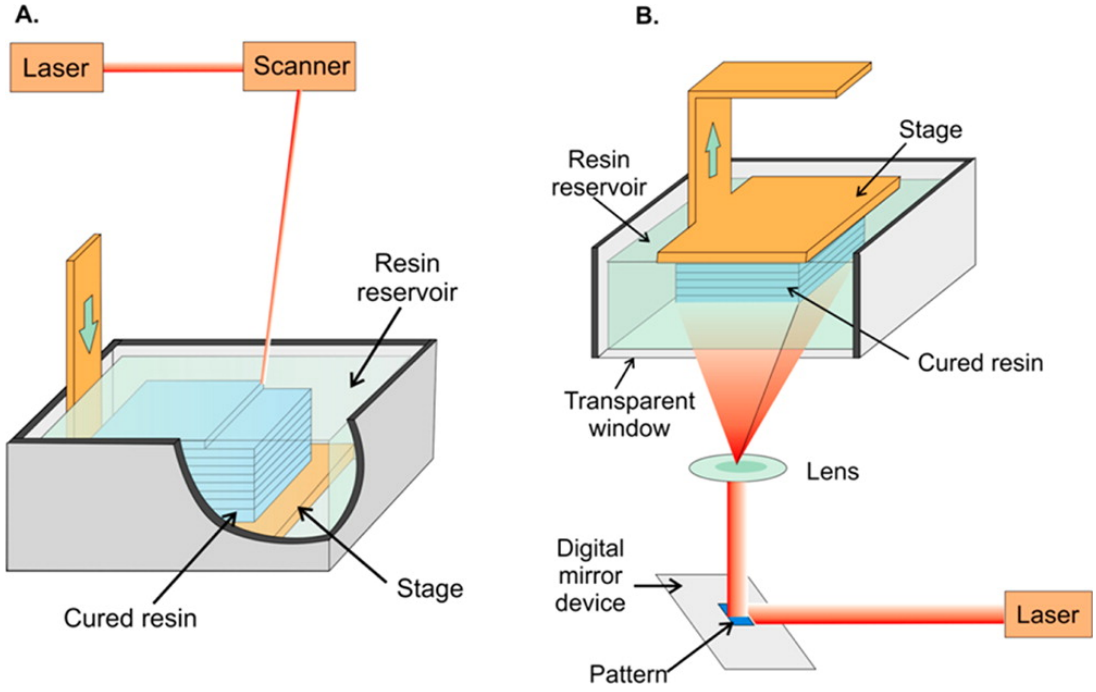

Figure 6.2 (A) Schematic of a bath configuration stereolithography (SLA) printer with a direct write curing process. A single laser moves along the surface of the resin, row by row, until completely curing the desired layer. (B) Schematic of a layer configuration SLA printer with a projection based curing method. In the projection based curing method, the digital mirror device allows for a whole layer to be cured simultaneously. "Adopted with permission from Gross, B. C.; Erkal, J. L.; Lockwood, S. Y.; Chen, C.; Spence, D. M., Evaluation of 3D Printing and Its Potential Impact on Biotechnology and the Chemical Sciences. *Analytical Chemistry* **2014,** *86* (7), 3240-3253. Copyright (2014) American Chemical Society."

Table 6.1 Commercially available SL systems, quoted specifications, and approximate prices. Adapted from Biomicrofluidics **8**, 052112 (2014); http://dx.doi.org/10.1063/1.4898632

Company	**Model**	**Resolution (μm)**		**Available resins**		**Price US$**
		XY	**Z**	**Transparent**	**Biocompatible**	
Formlabs	Form 1+	300	25	Y	N	1,088
MiiCraft	MiiCraft	56	50	Y	N	2,299
Smart3D	MiiCraft HR	Not stated	25	Y	N	6,674
Asiga	Freeform PRO	50–75	25	Y	Y (coming soon)	24,990
	Freeform pico	27–39	25	Y	Y (coming soon)	6,990–8,990
3D Systems	Projet 1200	56	30	N	N	4,900
Solidator	Solidator	270	30	N	N	4,950
FSL3D	Pegasus touch	80	25	Y	N	2,000
Old world laboratories	OWL Nano	Not stated	0.1	Y	N	2,000–5,000
LightForge	LightForge	150	25	Y	N	2,000–5,000
B9 Creator	v1.2	50	6.35	N	N	2,400
MakeX	M-One	140	20	N	N	2,000
mUVe	mUVe 1 3D	100	Not stated	N	N	5,99–1,699
Kudo 3D	Titan 1 HD	37	1	N	N	2,000
DigitalWax systems	Dental range*	Not stated	10	Y	Y	20,000–125,000
EnvisionTEC	Perfactory 3*	16	15	Y	Y	100,000

* Large scale (not desktop) printer

6.1.3 Inkjet Printing

Inkjet printing works in a way similar to common inkjet office printers. Early models used a jetting head to dispense a glue to bind an evenly distributed layer of fine powder, particle size 50-100 μm. A roller then applied pressure to flatten the surface and heat may be used to improve binding of the particles. Porosity and roughness were the main drawbacks and the polymer glues were not biologically compatible and swelled with solvents.

Recent models, like Objet's Eden 250, do not use powder but instead a photocurable resin. A roller still passes over the cured resin to flatten each layer as the printing proceeds. Bonyar *et al.* reported using this printer to make soft lithography templates (width, 4 mm; height, 300 μm) and microfluidic devices containing a mixer and homogenizer for gynaecological cervical sample preparation (channel height, 1 mm; width, 2 mm).[15] A similar printer, Objet Connex 350, was used to fabricate fluidic devices (3 mm wide and 1.5 mm deep channels) for drug transport studies.[16]

For environmental monitoring, Aritome *et al.* developed a monitoring device based on configurable modules fabricated with an inkjet 3D printer (Objet 24, Stratasys) and laser carving.[17] Although the printer offered a 28 μm layer thickness, the minimum channel width achieved for open channels was 200 μm. Laser carving of the printed chips enabled them to fabricate triangular channels that are 100 μm deep.

6.1.4 Selected 3D-microfluidic Applications

One of the strongest features of 3D printing is the ability to modify designs and test them within hours. Modular units were fabricated that can be connected to

perform different applications like mixing, gradient generation and droplet formation.[18]

The modular approach was also employed by Erkal *et al.* for electrochemical detection on printed devices using electrodes encased in polyetheretherketone (PEEK).[19] The electrodes could be easily fitted to the printed device then removed for wet polishing and reused. They used an Objet Connex 350 Multi-material 3D printer to print the device that featured 500 × 500 μm straight channel and threaded ports for easy connections. Dopamine was detected at LOD of 500 nM using Glassy carbon electrode coated with 0.05% Nafion.

Electrochemical detection is useful when printing with opaque materials. But for optical detection, a clear resin must be used. A lateral flow device printed with clear resin using Miicraft was reported for optical determination of glucose within the diagnostic range.[20] Cellulose powder paste functionalized for glucose sensing was used to fill the 3 channels, for control and 2 test concentrations. The assay was based on glucose oxidase enzyme catalysed oxidation of glucose into glucono delta-lactone and equivalent amount of hydrogen peroxide. The produced hydrogen peroxide was then utilised by horseradish peroxidase enzyme to catalyse oxidation of colourless iodide reagent into brown iodine. The average intensity of the yellow colour developed over 15 min after stabilization of the reaction can be correlated to the glucose concentration in the sample, measured through the green camera channel of a smart phone.

A chemiluminescence enzyme based assay for lactate in oral fluids and sweat was reported using a FDM printed device in black and transparent acrylonitrile-butadiene-styrene (ABS) polymers.[21] The two reaction chambers, for control and sample, contained nitrocellulose discs loaded with lactate oxidase and horseradish

peroxidase enzymes. LODs were 0.5 and 0.1 mM in oral fluids and sweat, respectively. A printed cell holder enabled signal detection with a smart phone camera. The same device was then modified for determination of total cholesterol in serum (LOD = 20 mg/dL) and total bile acid in serum and oral fluid (LOD = 0.5 μM).[22]

As discussed before under section 6.2.1.1, elimination of bulky parts like pumps and minimizing energy consumption are highly sought for portable devices. The ability to print in multiple materials with different mechanical strength, using Objet 260 printer (Stratasys), was utilized by Begolo *et al.* to design a device with equipment-free pumping lids that produce positive and negative pressures.[23] The method was based on the controlled compression or expansion of gas. The device can handle sample volumes up to few millilitres and provide stable flow ranging from few nanolitres to few microliters per second for hours.

Functionalities to control the fluid flow like valves are useful for certain applications. Printed microfluidic devices with integrated membrane-based valves were reported using a commercial low-cost SL printer and a custom resin formulation.[24] The resin was modified to give low non-specific protein adsorption. Up to 800 actuations were successfully performed. The Folch group employed a modular concept and mail ordered devices to demonstrate valves and pumps for fluidic control.[25] A control channel was pressurized with air to deflect a 100 μm thick membrane by a distance of 200 μm to stop fluid flow. Different arrangements were presented including 3 valves connected in series to perform as a pump and 4-valve switch for fluid control that was used to study the stimulant effect of different chemicals on cell culture. Also using an SL printer, Miicraft®, Su *et al.* used a sample load/inject valve with 5 μL capacity to connect a microdialysis system to an

inductively coupled plasma mass spectrometer (ICP-MS) for real time monitoring the extracellular levels of calcium and zinc ions in living rat brain.[26] The system was used to evaluate the toxic effects of N-methyl-D-aspartate perfusion at temporal resolution of 10 measurements per hour.

As printing closed channels is usually limited by the ability to remove the supporting material or uncured resin, some groups opted for printing templates for PDMS casting using the Miicraft® printer.[27] This approach is still faster than conventional photolithography to fabricate templates and offer different height structures that decrease the number of layers to be assembled. It is also noteworthy to mention that PDMS is still favoured for some biological applications due to its elasticity, gas permeability and biocompatibility.

6.1.5 Current Limitations

Although commercial 3D printers have been available since 1988, three limitations currently restrict their widespread uptake in microfluidics. First, except for few examples, the resolution is often incapable of producing a usable microchip because the printing process is always a compromise among resolution, processing time, and final print size. Very high-resolution systems are capable of printing only objects that are a few millimetres in dimension and therefore too small to be used as a microfluidic device. The second is the use of an appropriate resin that is cheap to use and has suitable mechanical, optical, electrical, and chemical properties. Most printers use opaque materials, which are not suitable when optical imaging is required, for example, for studying fluid dynamics. The third is the price of the printer. Most of the printers that meet the requirement of a print resolution of < 100 μm in all three dimensions cost close to US$ 20,000. A better resolution (16 μm in the z dimension)

can be achieved by a cutting-edge printer like the Connex 500 from Stratasys. It costs US$ 250,000 and allows for printing large models (400 mm × 500 mm × 200 mm) with different materials and colours, which may be useful for industrial applications but not necessarily for the field of microfluidics. The high cost of the printers hinders the flexibility to experiment with different non-proprietary resins, as this may violate the warranty conditions. Mail-order printing allows access to high-end printers at lower cost (US$ 200 per device compared to about US$ 2,000 to buy a desktop SL 3D printer) but this option may not be available in certain locations.[28] It is also important to note that the printer resolution is not equivalent to minimal structural dimensions because of other factors related to removing the uncured or supporting material and problems of overexposure when printing hanging structures.

6.2 Environmental Monitoring

Advantages of the industrial revolution cannot be denied but emissions and waste disposal represent a serious problem that may lead to catastrophic disruption of the eco system. Continuous monitoring is required to ensure that “safe” levels are maintained for soil, water and air. Regulatory guidelines are updated based on the long-term monitoring data as cumulative levels of some pollutants may take decades before serious effects are noticed and corrective actions are required to reverse or minimize the damage. Heavy metals, inorganic anions, chemical toxins, endocrine disrupting compounds (EDC), polyphenols and some pharmaceuticals are examples of the types of analytes that require monitoring.

Commercial kits are available for qualitative screening and are usually based on colour reactions and can be performed by following simple instructions. These low-cost tests are convenient for use at home to ensure drinking water quality or

swimming pools compliance, as daily or weekly check is considered adequate. Methods based on paper microfluidics are suitable for similar applications where continuous monitoring is not mandatory.

Environmental agencies sometimes demand high temporal and spatial resolution monitoring, in such case, manual sampling and analysis becomes time and labour intensive. The risk of contaminating the sample or physical and chemical changes during transport may compromise the integrity of the results and lead to false interpretation. *In-situ* or portable devices for environmental monitoring overcome these problems by performing analysis on-site. Preferably, sample pre-treatment is integrated onto the device.

Challenges for environmental monitoring differ from those of biological samples. For example, water samples vary considerably regarding matrix composition and ionic strength according to the source. Interferences can be minimized by using selective reagents and reaction conditions or performing a chromatographic separation. Subtraction of the matrix effect can be achieved through standard addition methods but this typically prolongs the analysis time and adds to the complexity of the assay. In contrast to biological samples, which are usually limited in volume, environmental samples are more abundant, in the range of tens to hundreds of millilitres.

Operational requirements for the "ideal" continuous monitoring device include low reagent and energy consumption and stability of performance for days to months under variable conditions of temperature, pressure, salinity or humidity if left unattended.[29] A high throughput assay will enable detection of temporal changes more accurately and if deployed on small vehicles or buoys, spatial changes can be easily mapped. Hence, the need for portability has directed research efforts towards

miniaturized flow injection analysis (μFIA) in the LOC format but sometimes at the cost of higher LOD. Electrophoretic LOC methods overcome problems due to small sample volume by on-chip electrokinetic sample preconcentration. Alternatively, third generation flow injection analysis (FIA) or lab-on-a-valve (LOV) systems have high sensitivity due to their ability to process larger volumes of sample. The following sections are representative discussion of some of these methods for environmental analysis.

6.2.1 Lab-on-a-Chip (LOC) Systems

Microfluidic systems for environmental monitoring can be classified into FIA methods employing pumps to drive the fluid flow and electrophoretic methods that use applied electric field as the main driving force. Excellent reviews cover the latest advances in microfluidics for environmental monitoring[29-30] and only few examples will be discussed here.

6.2.1.1 Miniaturized Flow Injection Analysis (μFIA)

FIA in its simplest form consists of a long reaction column and pumps to drive the flow of sample/standard and reagents. The sample is mixed with the reagents and a suitable detector is employed to measure the response, usually increased colour intensity, which can be related to the analyte concentration. Miniaturization efforts did not only aim to replace the reaction column with microchips but also to miniaturise other components such as the light source, detector and pumps to reduce energy consumption.

The high impact of nitrite levels on human and marine life and its high reactivity make a good case for on-site analysis. The Griess reaction is one of the most popular tests for nitrite determination and is frequently used to evaluate new

device performance. An intense pink coloured Azo dye is formed when the diazonium salt, from nitrite reaction with sulfanilamide hydrochloride in acid medium, is coupled with N-(1-Naphthyl) ethylenediamine dihydrochloride (NED). The colour intensity is linearly proportional to the nitrite concentration making the reaction suitable for quantitative purposes. One of the early miniaturized systems is the one developed by Greenway *et al*. for nitrite analysis based on Griess reaction and achieving 0.2 μM LOD.[31] Applied voltage was used to induce EOF in glass etched channels for reagent pumping instead of using pumps.

Different approaches have been reported to reduce the cost and size without compromising sensitivity. Nitrite was determined in the linear range 50 nM - 10 μM (14 nM LOD) by using a 25 mm path length to increase the absorbance and integrated LEDs as light source and photodiodes for detection at low cost.[32] This was subsequently developed into a more complex system featuring 3 syringes, 15 solenoid valves, and 3 absorption cells for in situ analysis of nitrite and nitrate in natural waters (Figure 6.3).[33] An off-chip cadmium reduction column was used to reduce nitrate into nitrite. One syringe offered the choice between injecting samples, blank, or one of 4 standards while buffer and Griess reagent were injected from syringes 2 and 3, respectively. To extend the linear range, a 25 mm long cell was used for low concentration (< 30 μM) and 2.5 mm long cell for high concentrations (> 30 μM). The device was able to operate continuously and provide high-resolution temporal data for more than 26 days when deployed in estuarine environment.

To avoid the use of pumps, a portable centrifugal microfluidic analysis system was developed, also for Griess test, featuring 7 analysis units on the microfluidic disc.[34] The device employs photosensitive ionogel valves to control the flow. The ionogel contracts upon excitation with white light which opens the valve and allow

flow through the selected channel under centrifugal force. Another group presented a proof-of-concept biomimetic fluid actuation using polypyrrole electroactive polymer.[35] The polymer swells upon reduction at low voltages (1 V) and shrinks by oxidation. By using soft polyurethane tubes coated with the polymer, redox cycles can be repeated to produce mechanical work that can drive solutions at 0.08 μL/s flow rate. While suitable for small-scale manufacturing, incorporation of ionogel valves may not be compatible with large-scale manufacturing and their stability for few months under fluctuating environmental conditions is yet to be proved.

FIA methods use mechanical force to achieve fluid flow. The presence of moving parts in the device complicates the manufacturing process and consumes more energy during operation. Frequent maintenance is required and can be a problem for devices deployed in not very accessible locations.

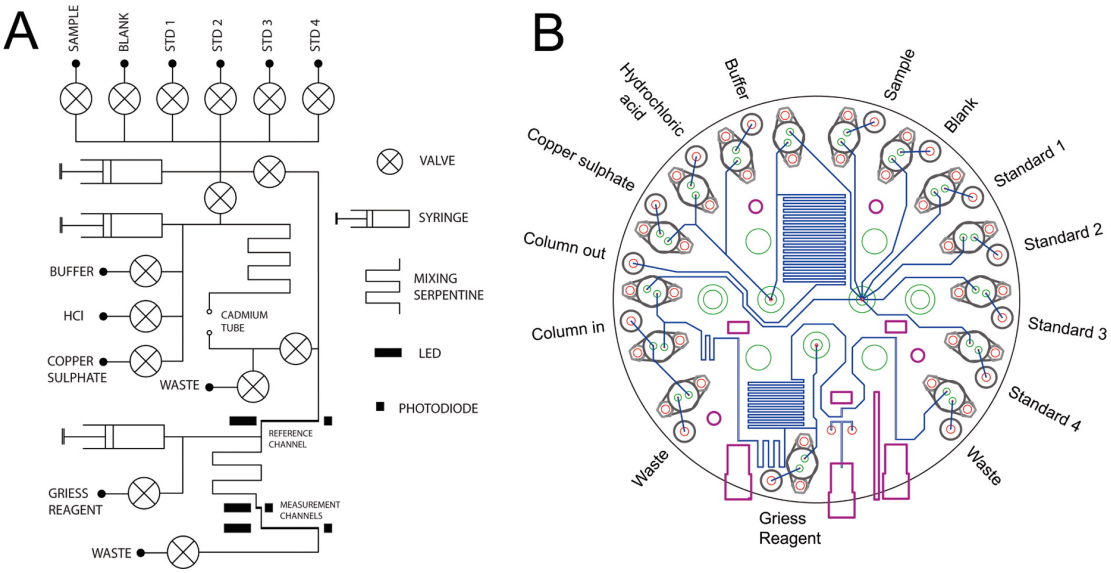

Figure 6.3 (A) Fluidic path diagram indicating the three syringes, fifteen valves, and three absorption cells. Inputs for standard solutions are indicated as STD. Hydrochloric acid (6%) is denoted as HCl. (B) CAD drawing of the microfluidic chip with fluidic connections labeled. "Reprinted with permission from Beaton, A. D.; Cardwell, C. L.; Thomas, R. S.; Sieben, V. J.; Legiret, F.-E.; Waugh, E. M.; Statham, P. J.; Mowlem, M. C.; Morgan, H., Lab-on-Chip Measurement of Nitrate and Nitrite for In Situ Analysis of Natural Waters. *Environmental Science & Technology* **2012,** *46* (17), 9548-9556. Copyright (2012) American Chemical Society."

6.2.1.2 Microchip Capillary Electrophoresis (MCE)

The use of MCE for portable monitoring devices is motivated by the ability to drive flow without the need for pumps. The separation power of electrophoresis allows the simultaneous determination of multiple analytes. Also, it overcomes the low sensitivity due to smaller dimensions by different electrokinetic approaches for on-line preconcentration mainly based on conductivity differences between the sample and BGE.

FASS was employed in portable CE system to achieve enhancement factors of 632- to 1078-fold for a mixture of 11 low-molecular-weight organic acids and 16 chlorinated acid herbicides.[36] LODs were 0.056-0.270 ppm. Polyvinyl alcohol (PVA) coated capillaries were used for separation to minimize analyte adsorption and suppress the EOF for better FASS performance. Organic acids, having higher conductivity, were detected as positive peaks while the herbicides were detected as negative peaks using contactless conductivity detection. This format is better than conventional conductivity as the electrodes are protected from surface fouling and no tedious alignment with the capillary is required.

When FASS and FASI were combined, 5200-fold enhancement was achieved enabling the determination of eight phenolic pollutants with amperometric detection.[37] Sensitivity was further enhanced by coating the screen-printed carbon electrodes with a cellulose-dsDNA mixture achieving LODs of 100-150 pM. The anionic surfactant, SDS, was employed for the MEKC separation. Later, the sensitivity was enhanced to achieve LODs between 7.1 and 11.1 fM by incorporating gold nanoparticles (AuNPs) in the preconcentration and separation buffers and using cellulose-dsDNA/AuNPs-modified carbon paste electrodes for electrochemical detection.[38]

While FASS and FASI are not suitable for high ionic strength samples, ITP can be used to enrich analytes by placing the sample between a high conductivity LE and low conductivity TE. Analytes within the sample will be stacked into zones defined by their mobility. A hand-held portable device was reported for monitoring chemical toxins in tap water.[39] The method was based on isotachophoresis with indirect fluorescence detection employing two mixtures of fluorescently labelled carrier ampholytes. The non-fluorescent 2-nitrophenol and 2,4,6-trichlorophenol, as examples for chemical toxins, displaced subsets of the ampholytes mixture possessing close electrophoretic mobility and were detected as non-fluorescent gaps in which the length was proportional to the analyte concentration. No sample pretreatment was required and the total analysis time was about 10 min.

Electrokinetic methods are easy to miniaturize. The absence of moving parts means that the devices are simpler and cheaper to manufacture. The main disadvantage however is the bias in sample injection due to matrix effects. The use of internal standards may be considered to solve this problem.

6.2.2 Other Platforms

For low frequency monitoring, paper-based assays are low cost and easy to operate. Integration of dual electrochemical and colorimetric detection on a paper microfluidic device was reported for the simultaneous determination of gold (III) and iron (III) in industrial wastewater.[40] Colorimetric determination of iron (III) was necessary as it interferes with the electrochemical detection of gold (III). Other methods like nucleic-acid based screening are also gaining attention for their ability to target a specific sequence, protein or chemicals.[41]

Efforts to make conventional capillary CE[42] and ion chromatography (IC)[43] portable are fuelled by the argument that more stable performance and better sensitivity can be achieved due to the material used to construct the separation column. A portable IC system using open capillary column coated with multilayers of stationary phase was reported for water environmental monitoring.[43] Gravity based fluid flow with maximum pressure of 20 kPa was employed to separate up to 7 alkali, alkaline earth and transition metals in water samples. A low cost capacitance sensor was used for detection and a built-in temperature sensor enabled baseline drift correction. Continuous operation was feasible for up to 8 h through a USB connection to a Netbook computer.

6.2.3 Conclusions

SL fabrication costs are expected to decline while higher resolution and resins with better physicochemical properties will be available. Biocompatible resins will benefit accelerate the research development in the biomedical field and clinical trial while resins that resist swelling with solvents and can handle high temperature and pressure will benefit research in the chemical synthesis area and long-term deployed environmental analytical devices. Development of prototypes with SL fabrication avoids a main commercialization hurdle that is associated with the transfer from conventional soft lithography into a more commercially viable technology like injection moulding or hot embossing, especially for low-volume production markets. This may lead to increasing number of start-up companies devoted for providing creative modules for microfluidic applications. Environmental analysis is a good example of low-volume market, as small modifications are often required to solve problems related to a specific sampling location and sample type.

6.3 References

1. Waldbaur, A.; Rapp, H.; Lange, K.; Rapp, B. E., Let there be chip-towards rapid prototyping of microfluidic devices: one-step manufacturing processes. *Analytical Methods* **2011,** *3* (12), 2681-2716.
2. Liao, Y.; Cheng, Y.; Liu, C.; Song, J.; He, F.; Shen, Y.; Chen, D.; Xu, Z.; Fan, Z.; Wei, X.; Sugioka, K.; Midorikawa, K., Direct laser writing of sub-50 nm nanofluidic channels buried in glass for three-dimensional micro-nanofluidic integration. *Lab on a Chip* **2013,** *13* (8), 1626-1631.
3. (a) McDonald, J. C.; Chabinyc, M. L.; Metallo, S. J.; Anderson, J. R.; Stroock, A. D.; Whitesides, G. M., Prototyping of microfluidic devices in poly(dimethylsiloxane) using solid-object printing. *Analytical Chemistry* **2002,** *74* (7), 1537-1545; (b) Moore, J.; McCuiston, A.; Mittendorf, I.; Ottway, R.; Johnson, R. D., Behavior of capillary valves in centrifugal microfluidic devices prepared by three-dimensional printing. *Microfluid Nanofluid* **2011,** *10* (4), 877-888; (c) Symes, M. D.; Kitson, P. J.; Yan, J.; Richmond, C. J.; Cooper, G. J. T.; Bowman, R. W.; Vilbrandt, T.; Cronin, L., Integrated 3D-printed reactionware for chemical synthesis and analysis. *Nature Chemistry* **2012,** *4* (5), 349-354; (d) Kitson, P. J.; Rosnes, M. H.; Sans, V.; Dragone, V.; Cronin, L., Configurable 3D-printed millifluidic and microfluidic 'lab on a chip' reactionware devices. *Lab on a Chip* **2012,** *12* (18), 3267-3271.
4. (a) Hull, C. W. Apparatus for production of three-dimensional objects by stereolithography. U.S. Patent 4,575,330, March 11, 1986; (b) Ikuta, K.; Hirowatari, K. In *Real three dimensional micro fabrication using stereo lithography and metal molding*, Micro Electro Mechanical Systems, 1993, MEMS

'93, Proceedings An Investigation of Micro Structures, Sensors, Actuators, Machines and Systems. IEEE., 7-10 Feb 1993; 1993; pp 42-47.

5. (a) Levy, G. N.; Schindel, R.; Kruth, J. P., Rapid manufacturing and rapid tooling with layer manufacturing (LM) technologies, state of the art and future perspectives. *CIRP Annals - Manufacturing Technology* **2003,** *52* (2), 589-609; (b) Vaezi, M.; Seitz, H.; Yang, S., A review on 3D micro-additive manufacturing technologies. *International Journal of Advanced Manufacturing Technology* **2013**, 1721-1754; (c) Gross, B. C.; Erkal, J. L.; Lockwood, S. Y.; Chen, C.; Spence, D. M., Evaluation of 3D printing and its potential impact on biotechnology and the chemical sciences. *Analytical Chemistry* **2014,** *86* (7), 3240-3253.
6. Kitson, P. J.; Marshall, R. J.; Long, D.; Forgan, R. S.; Cronin, L., 3D Printed high-throughput hydrothermal reactionware for discovery, optimization, and scale-up. *Angewandte Chemie International Edition* **2014,** *53* (47), 12723-12728.
7. (a) Hu, J.-B.; Chen, T.-R.; Chang, C.-H.; Cheng, J.-Y.; Chen, Y.-C.; Urban, P. L., A compact 3D-printed interface for coupling open digital microchips with Venturi easy ambient sonic-spray ionization mass spectrometry. *Analyst* **2015,** *140* (5), 1495-1501; (b) Prikryl, J.; Foret, F., Fluorescence detector for capillary separations fabricated by 3D printing. *Analytical Chemistry* **2014,** *86* (24), 11951-11956; (c) Salentijn, G. I. J.; Permentier, H. P.; Verpoorte, E., 3D-Printed paper spray ionization cartridge with fast wetting and continuous solvent supply features. *Analytical Chemistry* **2014,** *86* (23), 11657-11665.
8. (a) Melchels, F. P. W., Celebrating three decades of stereolithography. *Virtual and Physical Prototyping* **2012,** *7* (3), 173-175; (b) Bertsch, A.; Bernhard, P.; Renaud, P. In *Microstereolithography: Concepts and applications*, Antibes-Juan les pins, Antibes-Juan les pins, 2001; pp 289-298.

9. Ikuta, K.; Maruo, S.; Kojima, S. In *New micro stereo lithography for freely movable 3D micro structure-super IH process with submicron resolution*, Micro Electro Mechanical Systems, 1998. MEMS 98. Proceedings., The Eleventh Annual International Workshop on, 25-29 Jan 1998; 1998; pp 290-295.
10. Nakamoto, T.; Yamaguchi, K.; Abraha A, P. In *Consideration on the producing of high aspect ratio micro parts using UV sensitive photopolymer*, Micro Machine and Human Science, 1996., Proceedings of the Seventh International Symposium, 2-4 Oct 1996; 1996; pp 53-58.
11. Bertsch, A.; Zissi, S.; Jezequel, J. Y.; Corbel, S.; Andre, J. C., Microstereophotolithography using a liquid crystal display as dynamic mask-generator. *Microsystem Technologies* **1997,** *3* (2), 42-47.
12. (a) Beluze, L.; Bertsch, A.; Renaud, P., Microstereolithography: A new process to build complex 3D objects. *Proceedings of SPIE - The International Society for Optical Engineering* **1999,** *3680* (II), 808-817; (b) Ha, Y.; Choi, J.; Lee, S., Mass production of 3-D microstructures using projection microstereolithography. *Journal of Mechanical Science and Technology* **2008,** *22* (3), 514-521; (c) Singh-Gasson, S.; Green, R. D.; Yue, Y.; Nelson, C.; Blattner, F.; Sussman, M. R.; Cerrina, F., Maskless fabrication of light-directed oligonucleotide microarrays using a digital micromirror array. *Nature Biotechnology* **1999,** *17*, 974 - 978; (d) Sun, C.; Fang, N.; Wu, D. M.; Zhang, X., Projection micro-stereolithography using digital micro-mirror dynamic mask. *Sensors and Actuators A: Physical* **2005,** *121* (1), 113-120; (e) Waldbaur, A.; Carneiro, B.; Hettich, P.; Wilhelm, E.; Rapp, B., Computer-aided microfluidics (CAMF): from digital 3D-CAD models to physical structures within a day. *Microfluidcs & Nanofluidics* **2013**, 625-635; (f) Pan, Y.; Zhou, C.; Chen, Y. In *Rapid Manufacturing in*

Minutes: The Development of a Mask Projection Stereolithography Process for High-speed Fabrication, ASME 2012 International Manufacturing Science and Engineering Conferences, Notre Dame, Indiana, USA, Notre Dame, Indiana, USA, 2012.

13. Zheng, X.; Deotte, J.; Alonso, M. P.; Farquar, G. R.; Weisgraber, T. H.; Gemberling, S.; Lee, H.; Fang, N.; Spadaccini, C. M., Design and optimization of a light-emitting diode projection micro-stereolithography three-dimensional manufacturing system. *Review of Scientific Instruments* **2012,** *83* (12).

14. O'Neill, P. F.; Ben Azouz, A.; Vázquez, M.; Liu, J.; Marczak, S.; Slouka, Z.; Chang, H. C.; Diamond, D.; Brabazon, D., Advances in three-dimensional rapid prototyping of microfluidic devices for biological applications. *Biomicrofluidics* **2014,** *8* (5), 052112.

15. (a) Bonyar, A.; Santha, H.; Ring, B.; Varga, M.; Gabor Kovacs, J.; Harsanyi, G., 3D Rapid Prototyping Technology (RPT) as a powerful tool in microfluidic development. *Procedia Engineering* **2010,** *5* (0), 291-294; (b) Bonyar, A.; Santha, H.; Varga, M.; Ring, B.; Vitez, A.; Harsanyi, G., Characterization of rapid PDMS casting technique utilizing molding forms fabricated by 3D rapid prototyping technology (RPT). *International Journal of Material Forming* **2012**, 1-8.

16. Anderson, K. B.; Lockwood, S. Y.; Martin, R. S.; Spence, D. M., A 3D printed fluidic device that enables integrated features. *Analytical Chemistry* **2013,** *85* (12), 5622-5626.

17. Aritome, K.; Bula, W. P.; Sakamoto, K.; Murakami, Y.; Miyake, R., 3D printed microfluidic devices and reconfigurable analysis system. In *17th International Conference on Miniaturized Systems for Chemistry and Life Sciences*, Freiburg, Germany, 2013; pp 1622-1624.

18. Bhargava, K. C.; Thompson, B.; Malmstadt, N., Discrete elements for 3D microfluidics. *Proceedings of the National Academy of Sciences* **2014,** *111* (42), 15013-15018.

19. Erkal, J. L.; Selimovic, A.; Gross, B. C.; Lockwood, S. Y.; Walton, E. L.; McNamara, S.; Martin, R. S.; Spence, D. M., 3D printed microfluidic devices with integrated versatile and reusable electrodes. *Lab on a Chip* **2014,** *14* (12), 2023-2032.

20. Comina, G.; Suska, A.; Filippini, D., Low cost lab-on-a-chip prototyping with a consumer grade 3D printer. *Lab on a Chip* **2014,** *14* (16), 2978-2982.

21. Roda, A.; Guardigli, M.; Calabria, D.; Calabretta, M. M.; Cevenini, L.; Michelini, E., A 3D-printed device for a smartphone-based chemiluminescence biosensor for lactate in oral fluid and sweat. *Analyst* **2014,** *139* (24), 6494-6501.

22. Roda, A.; Michelini, E.; Cevenini, L.; Calabria, D.; Calabretta, M. M.; Simoni, P., Integrating biochemiluminescence detection on smartphones: Mobile chemistry platform for point-of-need analysis. *Analytical Chemistry* **2014,** *86* (15), 7299-7304.

23. Begolo, S.; Zhukov, D. V.; Selck, D. A.; Li, L.; Ismagilov, R. F., The pumping lid: investigating multi-material 3D printing for equipment-free, programmable generation of positive and negative pressures for microfluidic applications. *Lab on a Chip* **2014,** *14* (24), 4616-4628.

24. Rogers, C. I.; Qaderi, K.; Woolley, A. T.; Nordin, G. P., 3D printed microfluidic devices with integrated valves. *Biomicrofluidics* **2015,** *9* (1), 016501.

25. Au, A. K.; Bhattacharjee, N.; Horowitz, L. F.; Chang, T. C.; Folch, A., 3D-printed microfluidic automation. *Lab on a Chip* **2015, DOI: 10.1039/C5LC00126A**.

26. Su, C.-K.; Hsia, S.-C.; Sun, Y.-C., Three-dimensional printed sample load/inject valves enabling online monitoring of extracellular calcium and zinc ions in living rat brains. *Analytica Chimica Acta* **2014,** *838* (0), 58-63.

27. (a) Comina, G.; Suska, A.; Filippini, D., PDMS lab-on-a-chip fabrication using 3D printed templates. *Lab on a Chip* **2014,** *14* (2), 424-430; (b) Chan, H.; Chen, Y.; Shu, Y.; Chen, Y.; Tian, Q.; Wu, H., Direct, one-step molding of 3D-printed structures for convenient fabrication of truly 3D PDMS microfluidic chips. *Microfluidics & Nanofluidics* **2015**, 1-10.

28. Au, A. K.; Lee, W.; Folch, A., Mail-order microfluidics: evaluation of stereolithography for the production of microfluidic devices. *Lab on a Chip* **2014,** *14* (7), 1294-1301.

29. Jokerst, J. C.; Emory, J. M.; Henry, C. S., Advances in microfluidics for environmental analysis. *Analyst* **2012,** *137* (1), 24-34.

30. (a) Marle, L.; Greenway, G. M., Microfluidic devices for environmental monitoring. *TrAC Trends in Analytical Chemistry* **2005,** *24* (9), 795-802; (b) Li, H.-F.; Lin, J.-M., Applications of microfluidic systems in environmental analysis. *Analytical Bioanalytical Chemistry* **2009,** *393* (2), 555-567.

31. Greenway, G. M.; Haswell, S. J.; Petsul, P. H., Characterisation of a micro-total analytical system for the determination of nitrite with spectrophotometric detection. *Analytica Chimica Acta* **1999,** *387* (1), 1-10.

32. Sieben, V. J.; Floquet, C. F. A.; Ogilvie, I. R. G.; Mowlem, M. C.; Morgan, H., Microfluidic colourimetric chemical analysis system: Application to nitrite detection. *Analytical Methods* **2010,** *2* (5), 484-491.

33. Beaton, A. D.; Cardwell, C. L.; Thomas, R. S.; Sieben, V. J.; Legiret, F.-E.; Waugh, E. M.; Statham, P. J.; Mowlem, M. C.; Morgan, H., Lab-on-chip

measurement of nitrate and nitrite for in situ analysis of natural waters. *Environmental Science & Technology* **2012,** *46* (17), 9548-9556.

34. Czugala, M.; Maher, D.; Burger, R.; Fraser, K. J.; Ducree, J.; Diamond, D.; Benito-Lopez, F., Portable lab-on-a-disc system integrating photo-switchable micro-valves for in-situ aquatic environmental monitoring. In *16th International Conference on Miniaturized Systems for Chemistry and Life Sciences*, Okinawa, Japan, 2012; pp 269-271.

35. Ramírez-García, S.; Baeza, M.; O'Toole, M.; Wu, Y.; Lalor, J.; Wallace, G. G.; Diamond, D., Towards the development of a fully integrated polymeric microfluidic platform for environmental analysis. *Talanta* **2008,** *77* (2), 463-467.

36. Xu, Y.; Wang, W.; Li, S. F. Y., Simultaneous determination of low-molecular-weight organic acids and chlorinated acid herbicides in environmental water by a portable CE system with contactless conductivity detection. *Electrophoresis* **2007,** *28* (10), 1530-1539.

37. Shiddiky, M. J. A.; Park, H.; Shim, Y.-B., Direct analysis of trace phenolics with a microchip: In-channel sample preconcentration, separation, and electrochemical detection. *Analytical Chemistry* **2006,** *78* (19), 6809-6817.

38. Noh, H.-B.; Lee, K.-S.; Lim, B. S.; Kim, S.-J.; Shim, Y.-B., Total analysis of endocrine disruptors in a microchip with gold nanoparticles. *Electrophoresis* **2010,** *31* (18), 3053-3060.

39. Bercovici, M.; Kaigala, G. V.; Backhouse, C. J.; Santiago, J. G., Fluorescent carrier ampholytes assay for portable, label-free detection of chemical toxins in tap water. *Analytical Chemistry* **2010,** *82* (5), 1858-1866.

40. Apilux, A.; Dungchai, W.; Siangproh, W.; Praphairaksit, N.; Henry, C. S.; Chailapakul, O., Lab-on-paper with dual electrochemical/colorimetric detection for

simultaneous determination of gold and iron. *Analytical Chemistry* **2010,** *82* (5), 1727-1732.

41. Palchetti, I.; Mascini, M., Nucleic acid biosensors for environmental pollution monitoring. *Analyst* **2008,** *133* (7), 846-854.

42. Ryvolová, M.; Macka, M.; Ryvolová, M.; Preisler, J.; Macka, M., Portable capillary-based (non-chip) capillary electrophoresis. *TrAC Trends in Analytical Chemistry* **2010,** *29* (4), 339-353.

43. Kiplagat, I. K.; Kubáň, P.; Pelcová, P.; Kubáň, V., Portable, lightweight, low power, ion chromatographic system with open tubular capillary columns. *Journal of Chromatography A* **2010,** *1217* (31), 5116-5123.

7 3D-Printing - Microfluidic Applications

The work presented in this chapter was published in; **Shallan, A.; Smejkal, P.; Corban, M.; Guijt, R.; Breadmore, M., Cost-Effective Three-Dimensional Printing of Visibly Transparent Microchips within Minutes.** ***Analytical chemistry*** **2014, 86, 3124-3130.** Hence, the text was modified only when necessary.

In this chapter, a desktop 3D-printer was used to fabricate micro- to millifluidic devices with integrated functionalities. The minimal cross sectional area of 250 µm was achieved for monolithic microchannels and 200 µm for positive structures.

7.1.1 Printer Specifications and Characterization

The Miicraft® (Miicraft, Hsinchu, Taiwan) is a DMD-based 3D printer with bottom-up projection to sequentially cure layers of resin (Figure 7.1). The object is designed in computer-aided design (CAD) software and converted into STL with triangle facets. The Miicraft® uses an Open Source Arduino Mega 2560 microcontroller board and Python-based software as the controller and slicer. A digital 3D model is virtually sliced into 2D cross sectional layers to generate bitmap images that sequentially feed into the DLP pico-projector (450 ppi). The projector has standard WVGA resolution (854 × 480 pixels) and has been modified to suit SL. The fully automated system allows fabrication of models of up to 43 mm × 27 mm × 180 mm ($x \times y \times z$) at printing speeds of 20 mm/h in height regardless of the design complexity. The printer is smaller, lighter and cheaper than other commonly available 3D printers and has an $x \times y$ pixel size of 56 µm × 56 µm and a pre-set Z resolution of 50 or 100 µm.

The colourless resin is proprietary, consists of a modified acrylate oligomer and monomer, an epoxy monomer, a photoinitiator, and additives, and has a low viscosity of 186 cps. The added epoxy monomer most likely lowers the viscosity at the expense of longer curing times.[1] The clear resin exhibits 60% transmittance from 430 to 620 nm for a 500 μm thick layer (Figure 7.2). The resin is expected to have autofluorescence like other acrylate resins, but a full evaluation of the autofluorescence properties of the printed resin was not undertaken. During the experiments, no autofluorescence was observed using a USB microscope fitted with 480 nm excitation and 510 nm emission filters. However, it was not possible to detect fluorescent compounds with excitation wavelengths of < 400 nm, like quinine (λ_{ex} = 350 nm, λ_{em} = 450 nm), as the resin absorbs strongly at this range. The cured resin is hydrophobic as indicated by the adsorption of the hydrophobic dye rhodamine 6G and the formation of water in oil rather than oil in water droplets. The filling of the microchannels was similar to that of PDMS channels, a hydrophobic material frequently used for the fabrication of microfluidic devices. The resin is electrically insulating which allows for electrophoretic separations.

The printing chamber contains a vertically moving stage onto which printed structures adhere up side down. This bottom-up format offers better vertical resolution over the top-down format and is more efficient regarding resin consumption. A small amount of fresh resin is automatically pumped to the resin vat as required during the printing process, which also minimizes incomplete crosslinking due to oxygen inhibition by avoiding long direct contact with air. A Teflon film at the base of the resin vat prevents the cured resin from sticking to the transparent window through which the projector images shine to cure the resin layers. Once a layer is cured, the stage moves up few millimetres to fill the vat with fresh resin then lowers

to a distance of 50 or 100 μm between the last cured layer and the bottom of the resin vat, depending on the preset layer thickness parameter. A photograph of an object halfway through the printing process is shown in Figure 7.1A. After the printing is complete, the model is washed with isopropyl alcohol and the uncured resin is flushed out, dried with compressed air, and postcured in the right-side chamber (Figure 7.1B). This approach does also not require a sacrificial material during the curing process, providing great flexibility in design across the three dimensions.

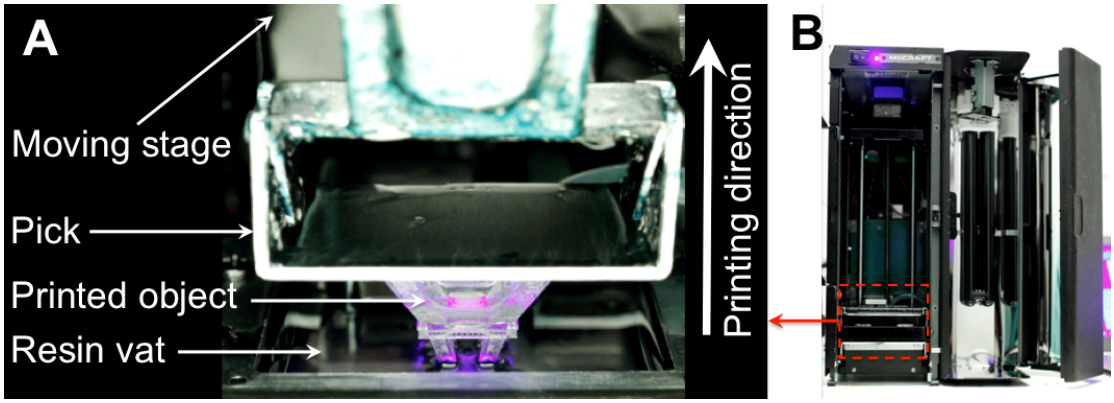

Figure 7.1 Miicraft® 3D printer. (A) Printing process in progress. A pico-projector below the resin vat (not shown here) projects light patterns, at 365 nm, from the bottom up on the resin. First, the stage moves the pick down, leaving a 50 µm gap between the pick and the bottom of the resin vat. After each curing step, the pick is moved up to allow fresh resin to redistribute in the bath before it is lowered to leave a 50 µm gap between the last cured layer and the bottom of the resin vat. The process is repeated until the model is created. The model is then rinsed with isopropyl alcohol, air-dried, and postcured for 10 min in the postcure chamber. (B) Printer with the doors open showing the printing unit on the left and the postcuring unit on the right. The dashed line shows the position of the resin vat shown in A with the stage in the home position. The printer size is 20.5 cm × 20.8 cm × 33.5 cm (width × depth × height) and weighs 6.5 kg.

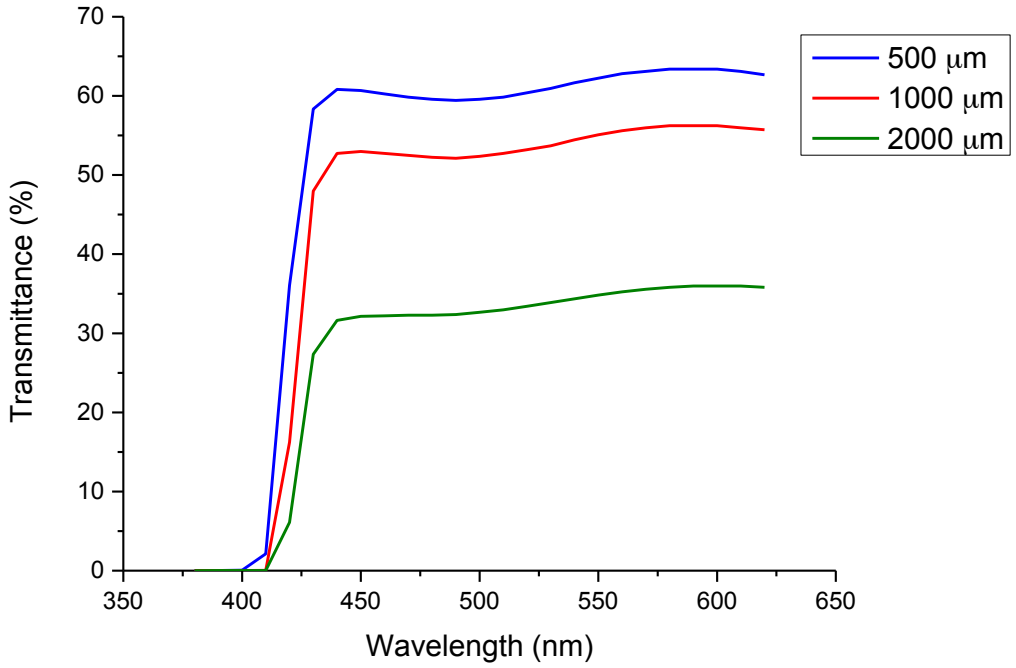

Figure 7.2 Cured Miicraft® clear resin % transmittance for different layer thickness (500, 1000, and 2000 μm).

A number of geometries was designed to evaluate the capability of the Miicraft® to print both positive and negative structures using the suggested exposure time of 3.5 s. High-aspect ratio columns were printed, but the material was not rigid enough to hold the structure in the upright position. Figure 7.3 shows scanning electron microscopy (SEM) images of L-shaped trenches, columns, and channels printed using an exposure time of 3.5 s. Close examination of the SEM images reveals more about the printing properties. The L-shaped trenches in Figure 7.3A have dimensions that are 50 or 100 μm narrower than the original design.

Considering the pixel size of the projector of 56 μm, this deviation corresponds to one or two pixels and could be attributed to the alignment between the digital images sent from the computer and the physical location of the pixels on the DMD. There are few points to be considered. First, when a pixel is partly covered by the design, it will be 'on' during projection, making the cross-linked feature up to 50 μm too large. If this occurs at both sides, the printed feature will be 100 μm larger than originally designed. Second, the light intensity within each pixel is not homogeneous. The intensity follows a Gaussian distribution with intensity maximum at the centre of the pixel. The light produced from neighbouring pixels may overlap and the light intensity at any point is the sum of the overlapping intensities. The resin will cure only if threshold intensity is reached. Third, the pixels are aligned diagonally to the metal stage to compensate for the inhomogeneity of light intensity within each pixel. This explains the observation of half printed pixels in the SEM images taken for round objects (Figure 7.4). As the light on the edge of a pixel is lower in intensity and in the absence of neighbouring "ON" pixels, the resin is not fully cured and will be washed away during the cleaning process. Finally, examining the sliced images revealed errors in the slicing program, ± 50 or 100 μm (Figure 7.5).

When targeting the open spaces like channels in microfluidics, this translates to the equivalent narrowing of the channel. The pixel alignment issue does not affect the vertical wall profile because within a single print run, the alignment of the mask and the DMD remains the same. Rotation of the model in the software by 45° to align the edges with the pixels did not produce any improvement in the accuracy of the channel geometry due to limitations of the slicing software. Panels B and C of Figure 7.3 show SEM images of posts and holes of various sizes where there is a size error of 50 or 100 μm. This corresponds to one or two pixels on either side of the mask and to errors in the slicing software. Realigning the model and slicing may improve the accuracy and such errors can be neglected for larger strucures. An array of square-based 400 μm × 400 μm × 1000 μm columns were printed and the %RSD values were 3.4, 3.8, and 2.0% in x, y, and z (n = 25), respectively.

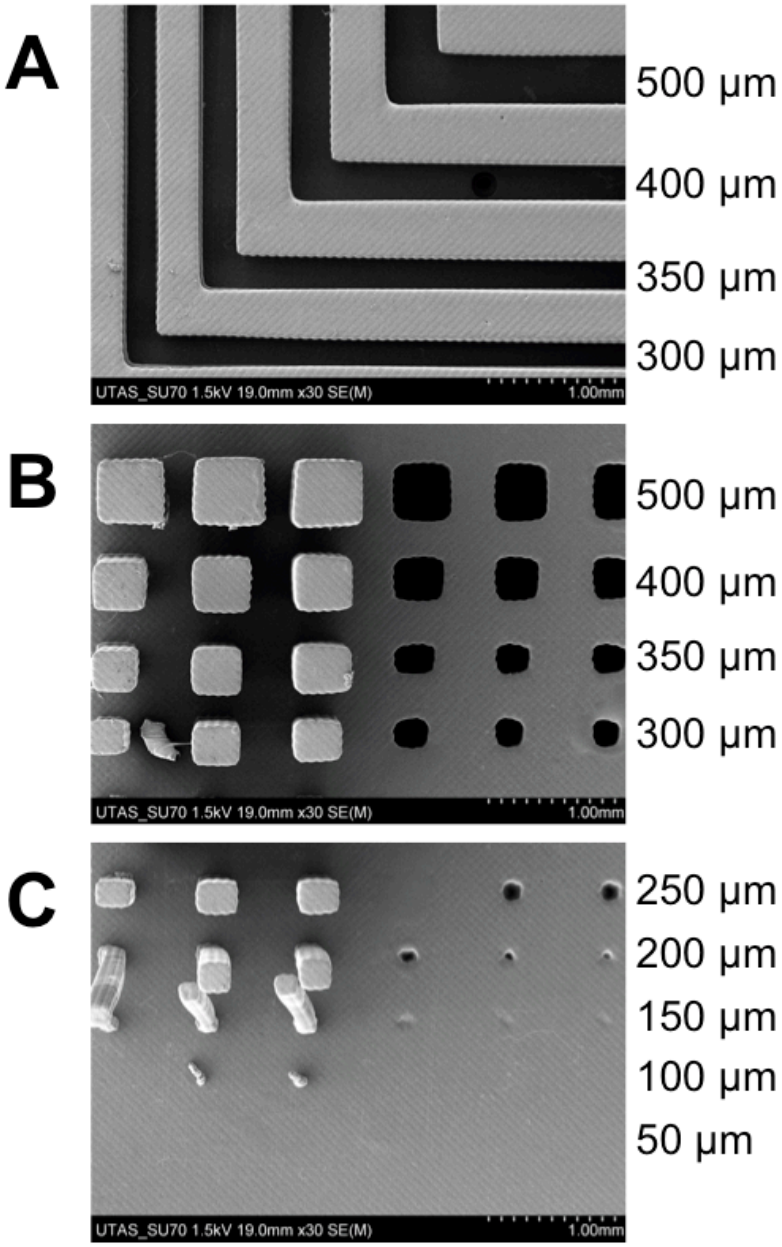

Figure 7.3 SEM images of positive and negative structures printed with an exposure time of 3.5 s. (A) L-Shaped trenches designed with a width of 300, 350, 400, and 500 µm. (B) Rows with three columns and three channels. The squares were designed to be 500, 400, 350, and 300 µm from the top to bottom with a constant height of 2000 µm. (C) Square columns and channels (x and y dimensions equal across a row) designed to be 250, 200, 150, 100 and 50 µm from top to bottom.

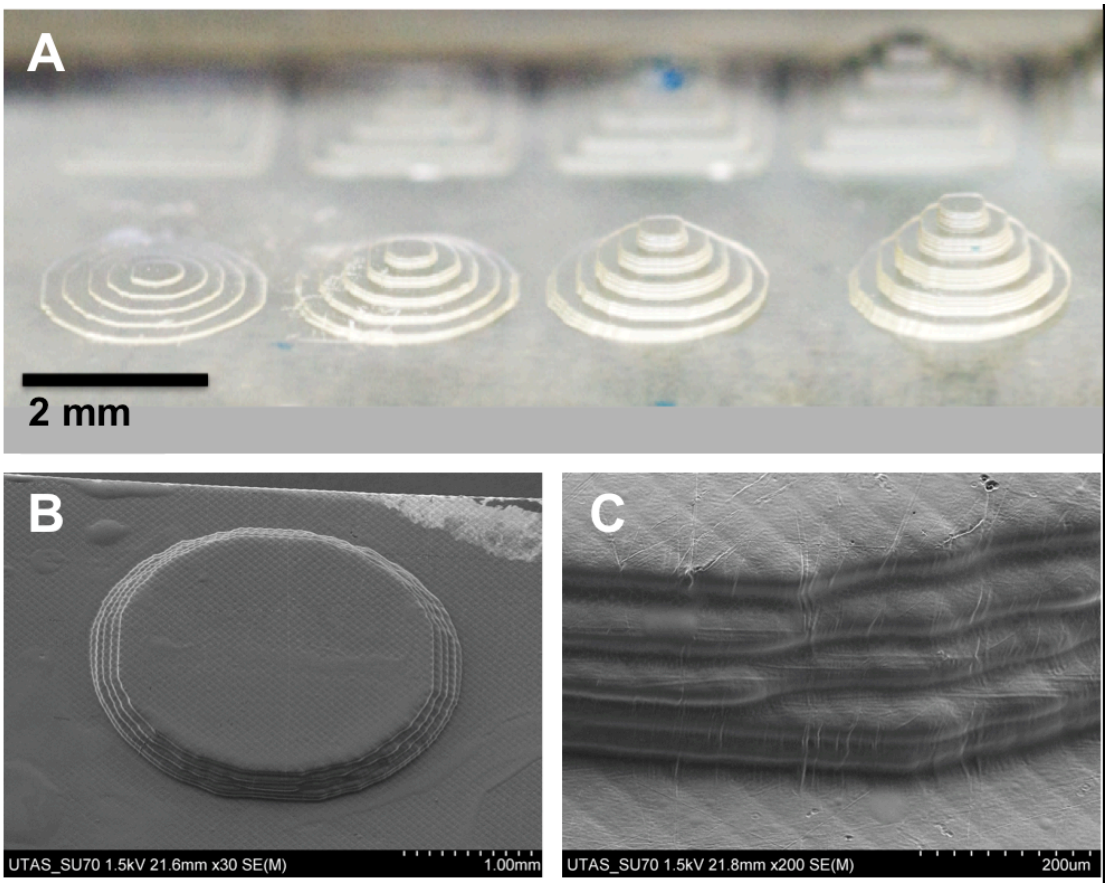

Figure 7.4 Round concentric steps printed to examine the z-resolution. (A) Photo of four concentric circular steps with varying heights of 50, 100, 150 and 200 μm (from left to right). (B) SEM image of steps that are 50 μm high each printed with an exposure time of 3.5 s. (C) SEM image revealing diamond shape pattern on the surface due to uneven light intensity of each pixel.

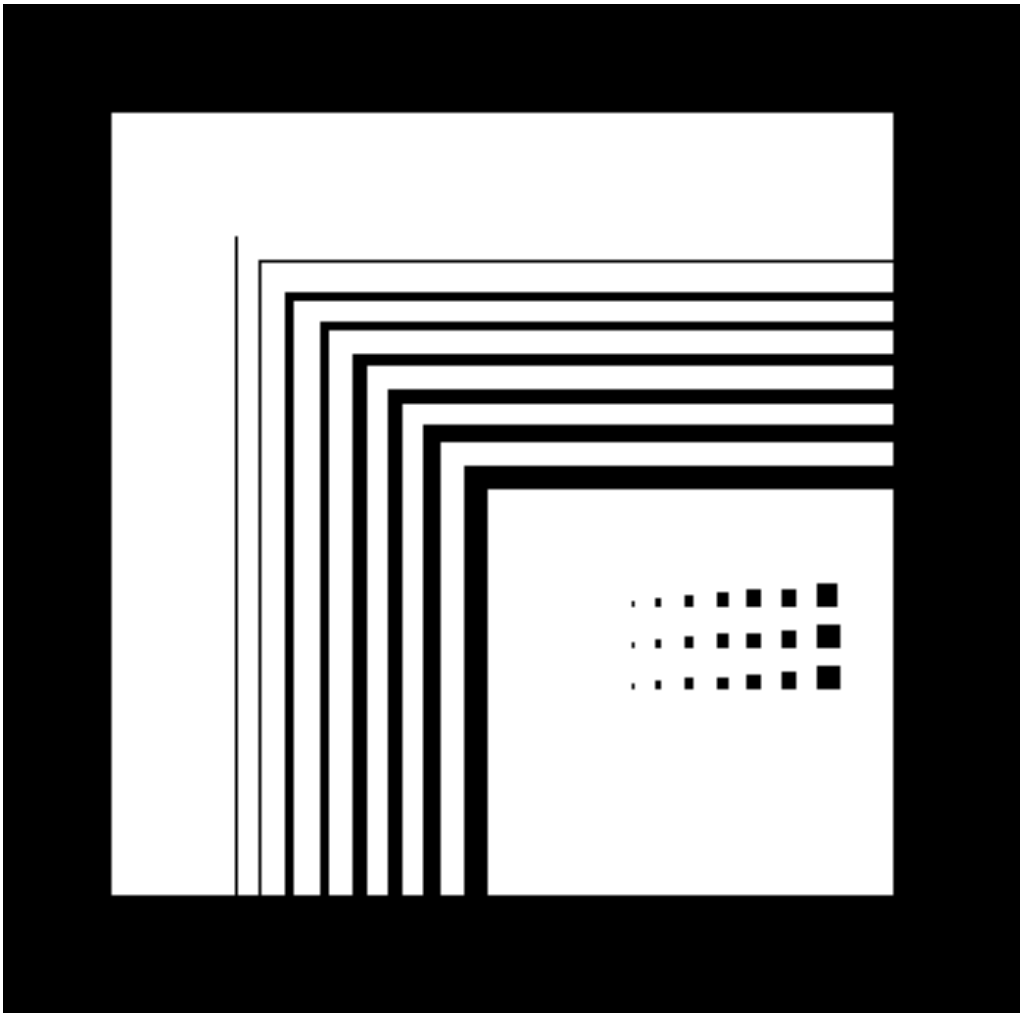

Figure 7.5 Sliced image for the design printed in Figure 7.3, columns are not shown in this image. White areas represent areas where the light intensity will reach the threshold to cure the resin. Black areas are underexposed and the uncured resin will be washed away during the cleaning process. Channels and squares dimensions were drawn in AutoCAD to be; 50, 100, 150, 200, 250, 300, 350, 400 and 500 μm. Unequal dimensions of the squares and the missing horizontal channel indicate 50 or 100 μm error from the slicing software.

The ability to print round shapes and the z resolution were studied by printing concentric circular steps (Figure 7.4). The z resolution (50 μm) is governed by the upward movement of the stage, which is determined by the number of turns of the shaft carrying the stage. The SEM image of the surface (Figure 7.4C) shows half-diamond shapes on the edges corresponding to a half-pixel and shows that the pixels are aligned at a 45° angle with respect to the metal pick. The light intensity of each pixel follows Gaussian distribution and extends to the neighbouring pixels. Areas between the pixels will polymerize as the light intensity equals the sum of the lower intensity light from all the neighbouring pixels but when adjacent pixel is OFF the resin on the edge of the pixel is underexposed and may wash off during the rinse with isopropyl alcohol.[2] Hence, the alignment of the pixels at 45^{o} relative to the stage will result in more accurate dimensions of the printed object.

Figure 7.6 shows a fully enclosed square channel designed to be 250 μm. The image shows a difference in surface roughness among the four sides of the channel. The bottom of the channel (side closest to the metal pick) was, like the open channels, flat and smooth (peak-to-valley distance of < 1 μm). The roof of the channel is rough (peak-to-valley distance of ≈10 μm), because of the so-called "back side effect"[3]: when a newly cured layer is not supported by a previously cured layer (or the metal stage), over curing results in structures exceeding the 50 μm target height, with an increased roughness on the back side caused by an uneven intensity profile of each pixel (Figure 7.7). Solving this problem will require changing the curing depth, intensity, exposure wavelength, or time when printing roofs or unsupported structures. These changes require the development of new resins and modification of the printer hardware and software.

Despite the *x, y,* and *z* resolution of approximately 50 μm, the smallest fully enclosed features achieved were 250 μm square channels. It is suspected that the remaining resin in smaller channels may be in a partially cured or in gel form, creating a high backpressure and making its removal from the channels difficult, especially for longer channels. Developing a new resin with a lower viscosity and a longer curing time may help resolve this issue at the expense of longer fabrication times. This is a challenging task as the resin should also fulfil other physical and chemical compatibility requirements.

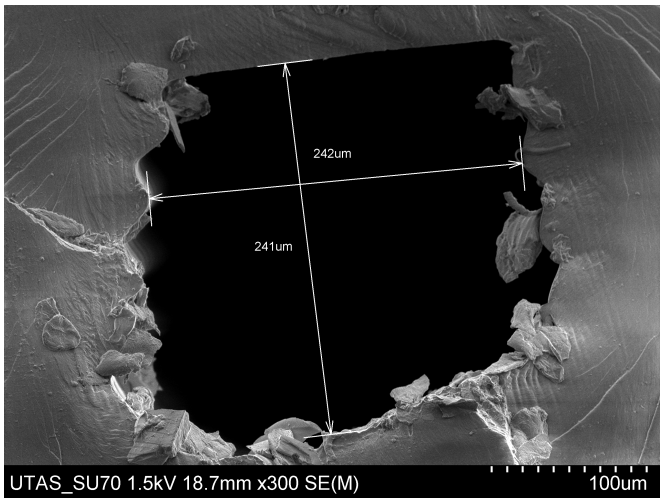

Figure 7.6 SEM images of a transverse section of closed channels designed with equal dimensions for width and depth, 250 μm. The models were printed upside down. The backside effect results in a rough surface for hanging structures. The roughness of the sidewalls is due to the layering nature of the printing process.

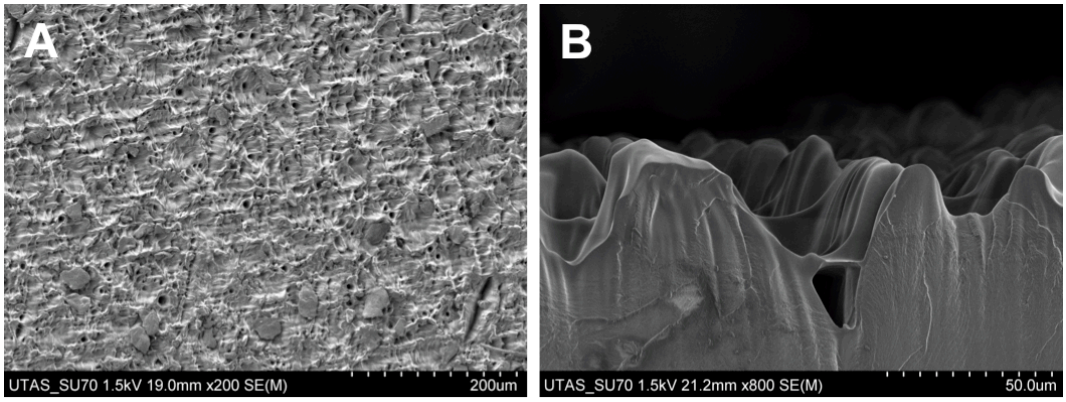

Figure 7.7 SEM images of the back of a printed hanging structure showing the backside effect. (A) Overview of the surface roughness showing a diamond shape pattern. The scale indicates 56 μm dimensions which corresponds to the projector's pixels. (B) The surface roughness is indicated by the valley-to-peak distance of approximately 10 μm.

In all the experiments, except for ITP, the flow rate was controlled using a syringe pump (Pump 33, Harvard Apparatus) and 20 mm internal diameter plastic syringes connected to the device through Teflon tubing and commercial fittings (Upchurch). In the ITP experiment, voltage was applied through an interface fitted with two platinum electrodes using a laboratory-built power supply. Fluorescence images were taken with a USB microscope (Dino-Lite Premier AM4113T-GFBW) fitted with a blue light-emitting diode for excitation and a 510 nm emission filter, while white light images for the gradient generator and the nitrate test were recorded with a digital camera (Canon PowerShot SX260 HS).

7.1.2 Results and Discussion

The Miicraft® was used to quickly fabricate 3D microfluidic devices at a cost of few dollars per device. I demonstrate four applications with designs previously published using conventional fabrication methods. The applications targeted in this work include pressure-driven flow using syringe pumps (mixing, gradient generation, and droplet extraction) and applied electric field (ITP). These applications benefit from the 3D geometry, the easy connection to other commercially available units, or the fast and flexible modification of channel dimensions. A device combining multiple units was applied for continuous colorimetric nitrate analysis in tap water using the Griess test and standard addition in a single run.

7.1.2.1 Mixing

Fluid mixing is a function required in many microfluidic systems. Spontaneous fast and efficient fluid mixing is difficult to achieve inside microchannels because of the laminar nature of the flow. Passive mixers are simpler, cheaper, and more reliable than active mixers that rely on moving parts. It has been

well documented that the mixing efficiency is increased when moving from 2D to 3D geometries[4]; however, these geometries are much harder to fabricate. Carrieѐ proposed a 3D micromixer of sequential symmetrical units based on Baker's transformation.[5] Mixing is achieved by splitting and recombining the flows at a perpendicular angle, with each split and recombination termed a mixing unit. After passing through multiple units, the folded flow streams are sufficiently narrow to allow for fast diffusion-based mixing. The fabrication of this device with conventional methods is challenging and was recently realized in glass using femtosecond laser writing,[6] which is not readily available to most laboratories. The same design was printed including threads that securely fit commercially available connectors (Figure 7.8A). To take into account the capabilities of the printer, the original dimensions were scaled up by 10, yielding 500 μm wide and deep channels (Figure 7.8B). The entire chip was 40 mm × 25 mm × 17 mm (width × depth × height), including connectors to the syringe pump, and could be printed in 50 min with a material cost of US$ 2. Figure 7.9 shows the performance of this mixer compared to that of a straight channel with similar dimensions using aqueous solutions of 0.1 μg/mL fluorescein (green) and 1 μg/mL rhodamine B (red) at a flow rate of 100 μL/min each. Intensity profile analysis (Figure 7.9) of the fluorescence images shows a homogeneous distribution of green and red across the channel, indicating complete mixing after passing through four mixing units, while maxima of green or red on either side of the control straight channel indicated no mixing after passing through the same length.

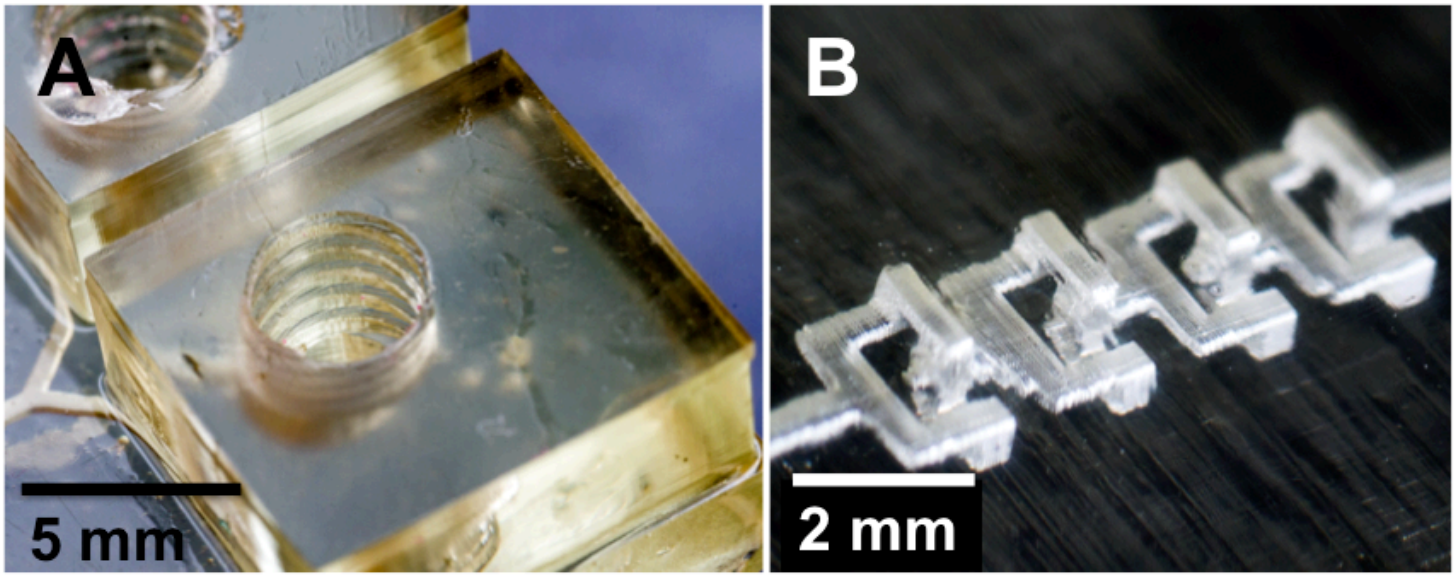

Figure 7.8 3D passive micromixer printed with clear resin. (A) Thread (10-32) for connecting the device to syringe pumps. (B) Four mixing units printed horizontally at 10 times larger than the original design to obtain channels that are 500 μm wide and deep.

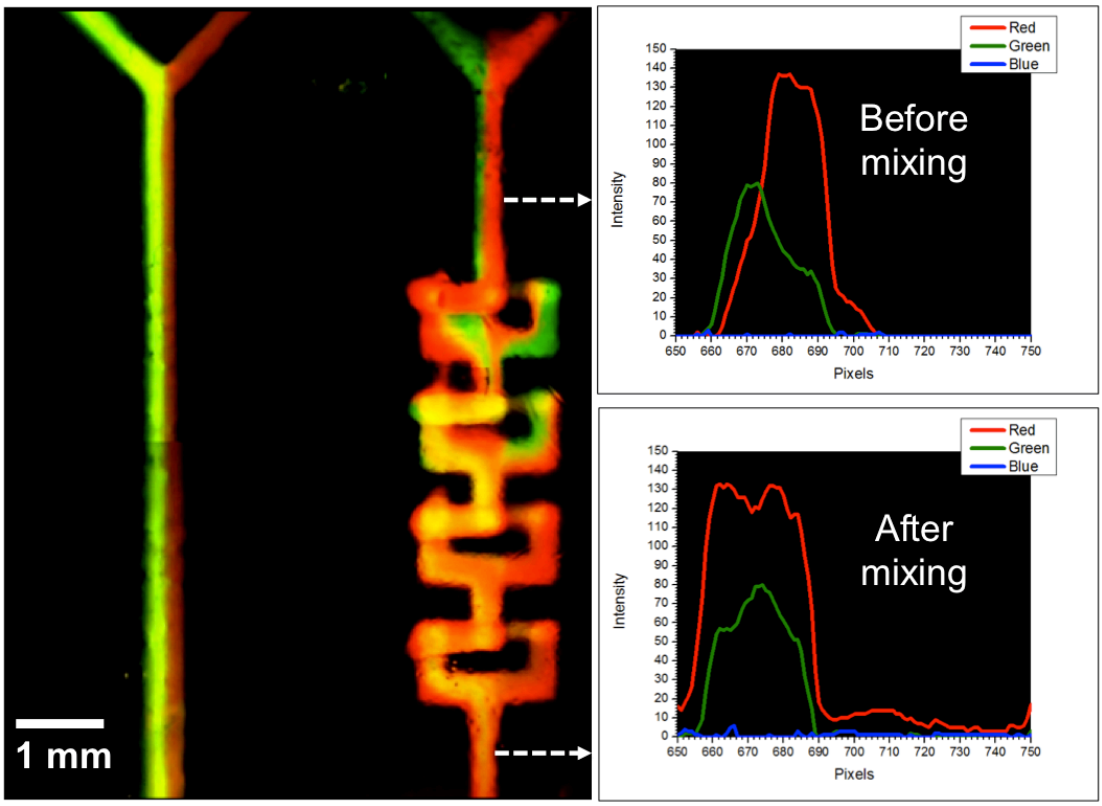

Figure 7.9 Mixing experiment using the printed device. Fluorescent images of the mixing performance compared to flow in a straight channel using aqueous solutions of 0.1 µg/mL fluorescein (green) and 1 µg/mL rhodamine B (red) at a flow rate of 100 µL/min each. The intensity profiles (on the right side) indicate different distributions of fluorescein and rhodamine B before mixing (top) and a homogeneous distribution after four mixing units (bottom).

7.1.2.2 Gradient Generation

Gradient generators operate by splitting and combining two different flows in a defined and systematic manner. Gradients produced in this way have been used for screening studies, including chemotaxis,[7] cytotoxicity tests,[8] and other assays. A combinatorial gradient generator that included dilution, distribution, and mixing functions was reported by Neils *et al.* and required the assembly and bonding of nine layers.[9]

2D gradient generators are more popular as they are easy to fabricate, but 3D designs pack the microchannels more densely than those in 2D, reducing the footprint and making it more convenient for portable devices. A gradient generator with 3D channels (200 μm wide and 30 μm deep) with three levels of splitting and recombining was reported using direct projection in dry-film photoresists.[10] The process required repeating three fabrication steps (lamination, exposure, and development) four times for the five-layer device. I printed the same design with 1000 μm × 500 μm channels (Figure 7.10A) and threads for fluidic connection in 210 min, with a material cost of US $5 in a single step. The gradient was visualized using white light and the dyes bromothymol blue (blue) and rhodamine B (red) (Figure 7.10B). The solutions were prepared in methanol (1 mg/mL each), and the flow rate was 1 mL/min. As shown in Figure 7.10B, a five-step gradient is produced ranging from red to blue. The efficiency of the device for generating gradients was demonstrated by the linear relation between the colour intensity measured through the green channel and the expected red dye percentage ($R^2 = 0.9848$) (Figure 7.11).

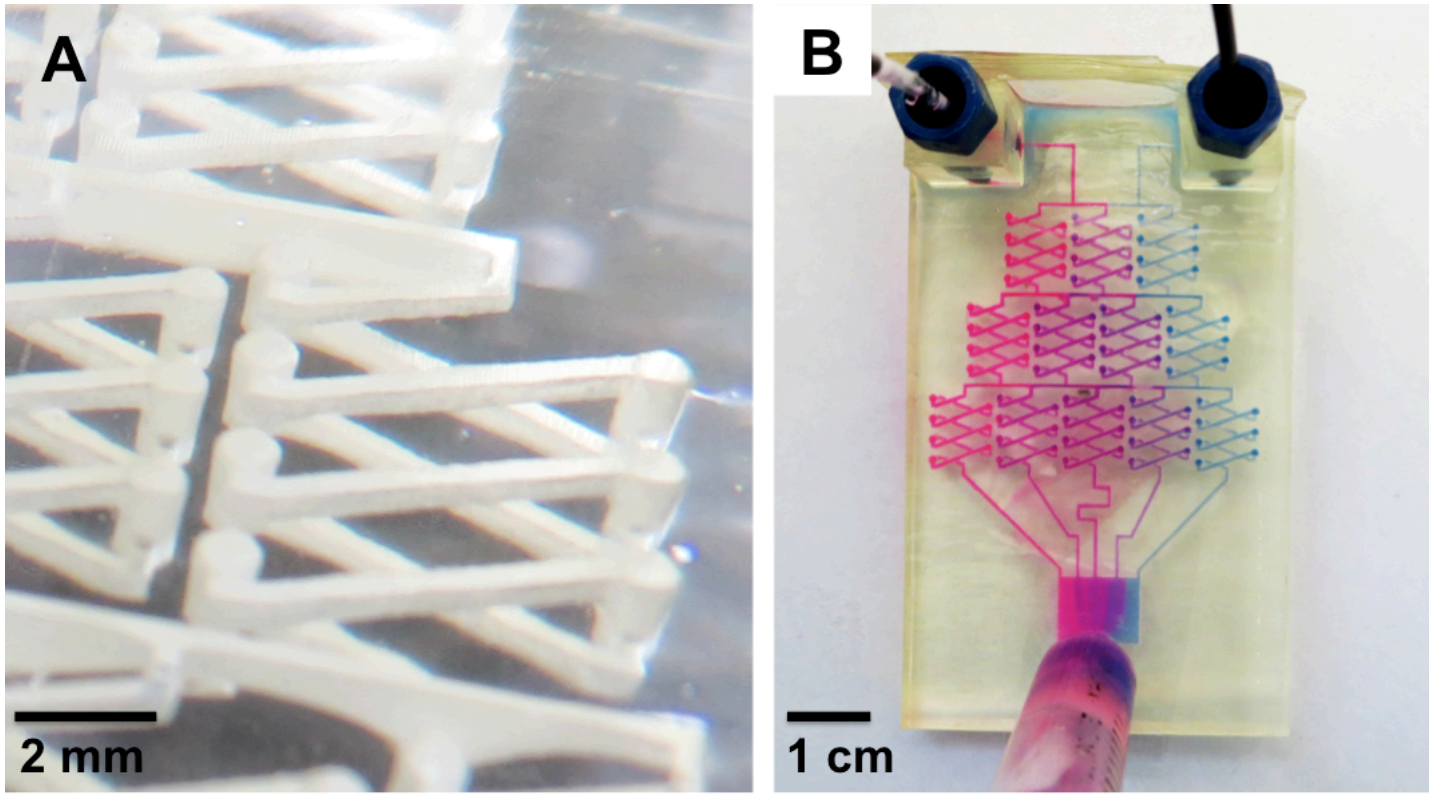

Figure 7.10 Gradient generator printed in clear resin. (A) Close-up of one 3D printed unit. (B) Gradient generation using two coloured dyes, rhodamine B (left) and bromothymol blue (right). The device has three levels of combining, mixing, and splitting, resulting in three mixtures with different dye ratios and pure dyes on the peripheral units.

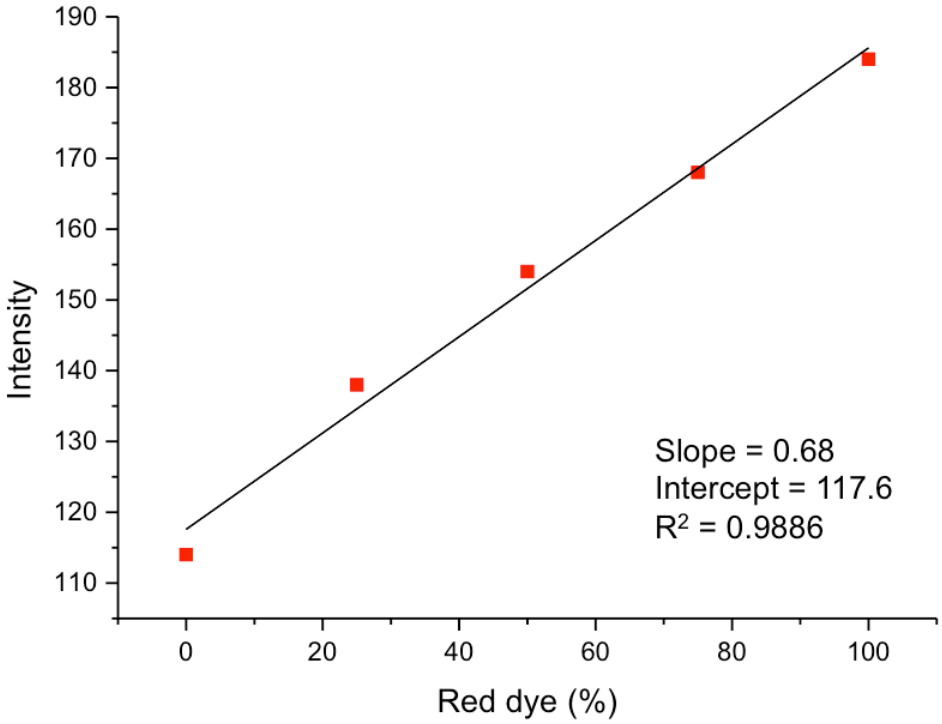

Figure 7.11 Linear relation between the expected red dye concentration and measured intensity profiles confirming the splitting ratios of the gradient generator. As the intensity measurements were taken in a white light background, the red dye was read through the green channel as a negative response, which explains the non-zero intercept.

7.1.2.3 Droplet Extraction

Droplet-based systems use immiscible phases to create discrete droplets of one phase in another. Droplet microfluidics serves different applications, including the synthesis of biomolecules, crystallization studies, drug delivery, and diagnostic testing.[11] There are different types of droplet generators, and the design used here is based on the droplet generator reported by Li *et al.*[12] The aqueous phase is sandwiched between two streams of organic phase, resulting in water-in-oil droplets. Here, droplets were used for extraction, which is superior to laminar-flow extraction because internal circulation within the droplet greatly increases the extraction efficiency. The microchip was 91 mm × 18 mm × 15 mm (width × depth × height; material cost of less than US $3) and featured two inlets and two outlets (Figure 7.12A). Droplets were formed when the flows of the aqueous phase, containing a mixture of two fluorescent dyes, coumarin 334 (green) and rhodamine B (red), and the organic phase (decanol) merged. Coumarin 334 is neutral and thus extracted into decanol, while rhodamine B is positively charged and remains in the aqueous droplet. The hydrophobic channel wall is wetted with decanol as illustrated with the green layer surrounding the red droplets (Figure 7.12B). 3D printing allowed the inclusion of a spherical collection reservoir at the end of the extraction channel with top and bottom channels to direct the separated phases into two separate reservoirs (Figure 7.12C,D) that allow the collection of separate phases as a single and continuous flow. The inclusion of windows on the sides of the reservoir facilitates visual observation of the phase separation to optimize the flow rate. The flow rates of both the aqueous sample and decanol were set at 1 μL/min. The printer used in this work demonstrates the valuable ability to rapidly and cheaply fabricate a relatively complicated 3D device in a material that is resistant to organic solvents, eliminating one of the

limitations of many of the other materials available for 3D printers. The extraction efficiency was verified by measuring the intensity profiles of the green and red dye in the organic and aqueous phases (Figure 7.13).

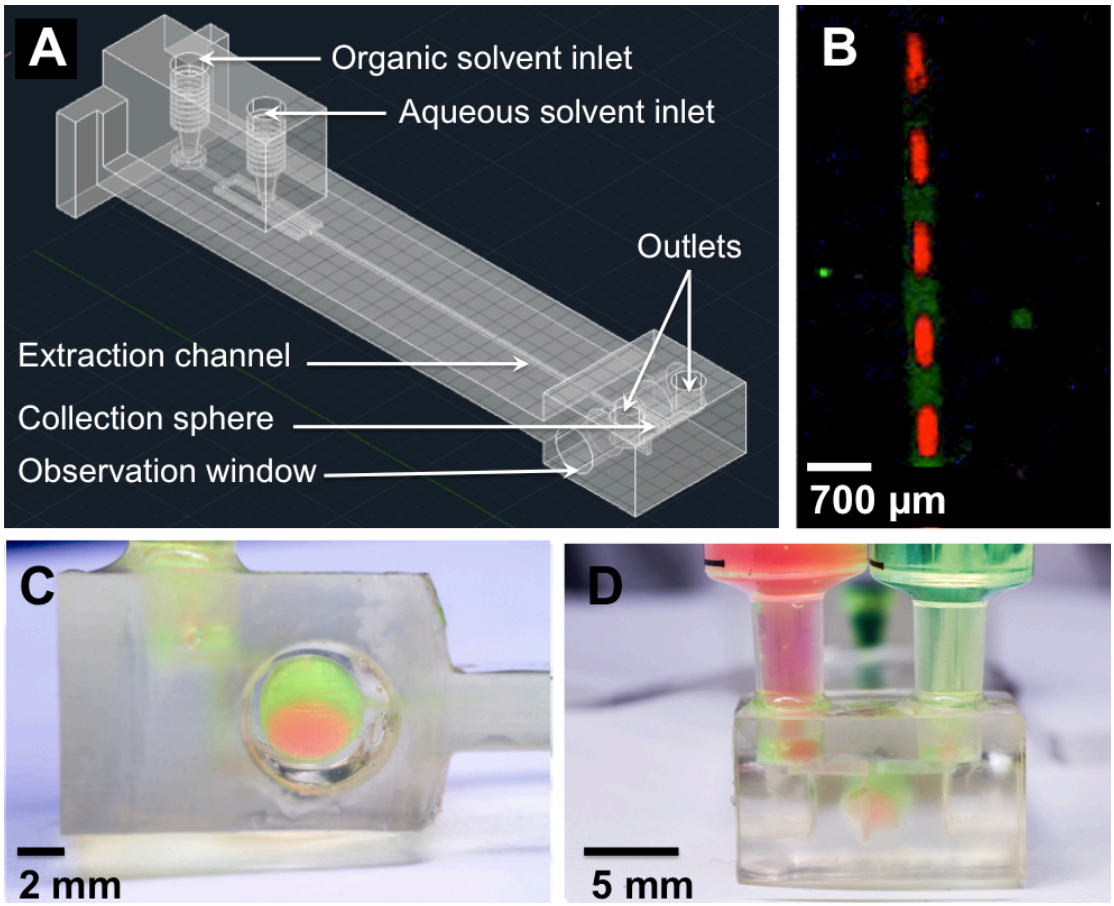

Figure 7.12 Droplets for liquid−liquid extraction. (a) CAD design of the device featuring one channel for the aqueous phase and two channels for the organic phase. The long straight channel ends with a collection sphere with channels on top and bottom for the collection of the organic and aqueous phases, respectively. (b) Extraction of coumarin 334 (green) into decanol (organic phase) from an aqueous mixture with rhodamine B (red) as seen under a microscope with fluorescent detection of the formed droplets. The flow rates of both the aqueous sample and decanol were set at 1 µL/min. (c) Side view of the collection sphere at the end of the channel showing phase separation. (d) Top and bottom channels direct each phase into separate reservoirs.

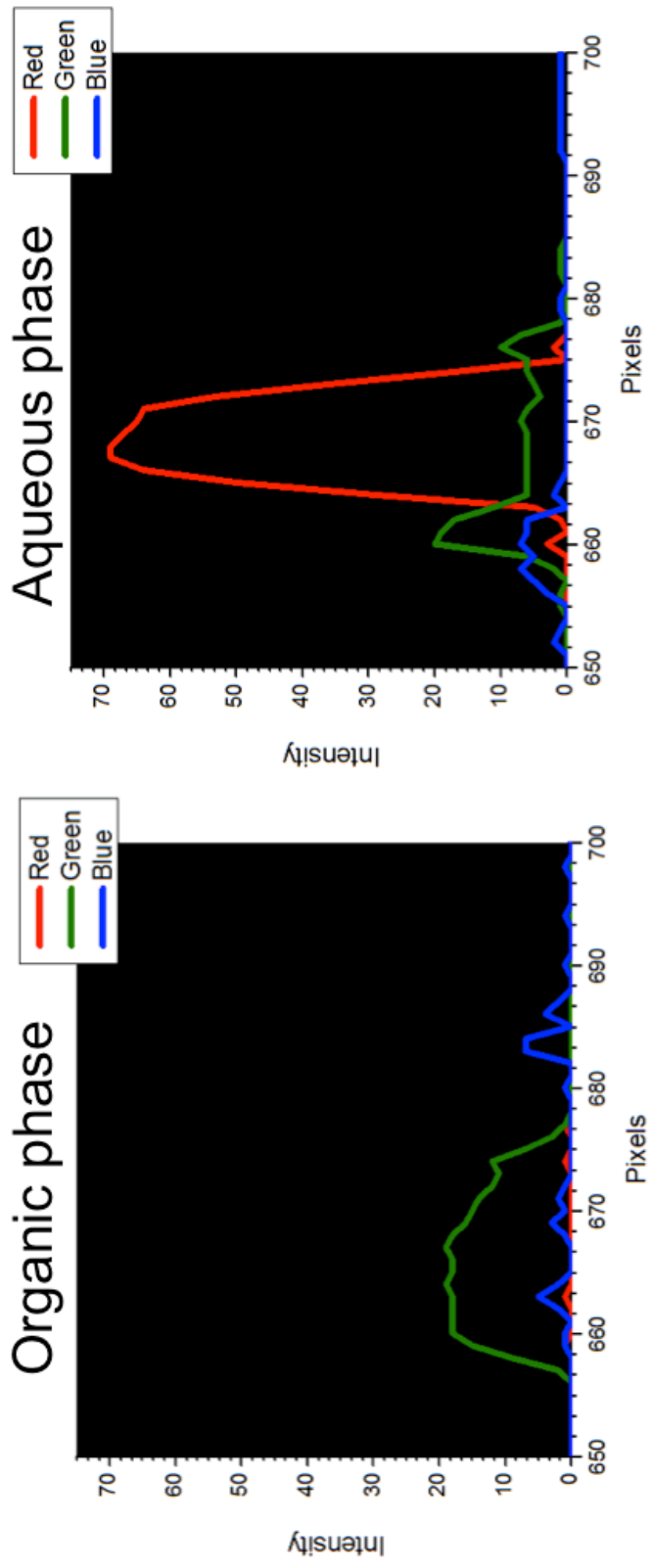

Figure 7.13 Intensity profiles at the end of the straight channel of the droplet generator. The organic phase contains coumarin 334 (green) and the aqueous phase (droplets) contains rhodamine B (red). The traces of green colour in the intensity profile of the aqueous phase are due to the fact that water-in-oil droplets are formed and each droplet is surrounded with a thin film of oil.

7.1.2.4 Isotachophoresis

Another major application area of microfluidics is electrophoresis where both the electrical insulation and optical properties are important. However, performing CZE in wide channels (> 250 μm) necessitates the use of low-conductivity buffers to prevent excessive joule heating that leads to poor separation. ITP is an electrophoretic separation technique characterized by a self-sharpening mechanism of the separated zones. In the discontinuous electrolyte system, the sample ions are separated on the basis of mobility, with the fastest analytes closest to the leading electrolyte and the slowest analytes stacked at the terminator end. Separation of three anionic dyes, 1 ppm xylenol orange (red, fastest), 1 ppm CNF (blue), and 1 ppb fluorescein (green) was achieved. The ITP system employs a LE composed of 10 mM hydrochloric acid adjusted to pH 9 with Tris and 0.5% HPMC to suppress the EOF. The dyes were dissolved in the TE composed of 1 mM 3- (cyclohexylamino)-1-propanesulfonic acid (CAPS) adjusted to pH 9.4 with Tris. The device contained a 10 cm long serpentine channel (500 μm × 1000 μm (Figure 7.14A)), and 1000 V was applied across the channel (100 V/cm). The zones took 5 min to reach steady state (Figure 7.14B). The entire chip was 40 mm × 25 mm × 4 mm (width × depth × height) with a print time of 12 min costing US $1 per microchip. The ability to perform separations and optical detection on printed devices offers great research opportunities as modifications, and testing can be done within hours.

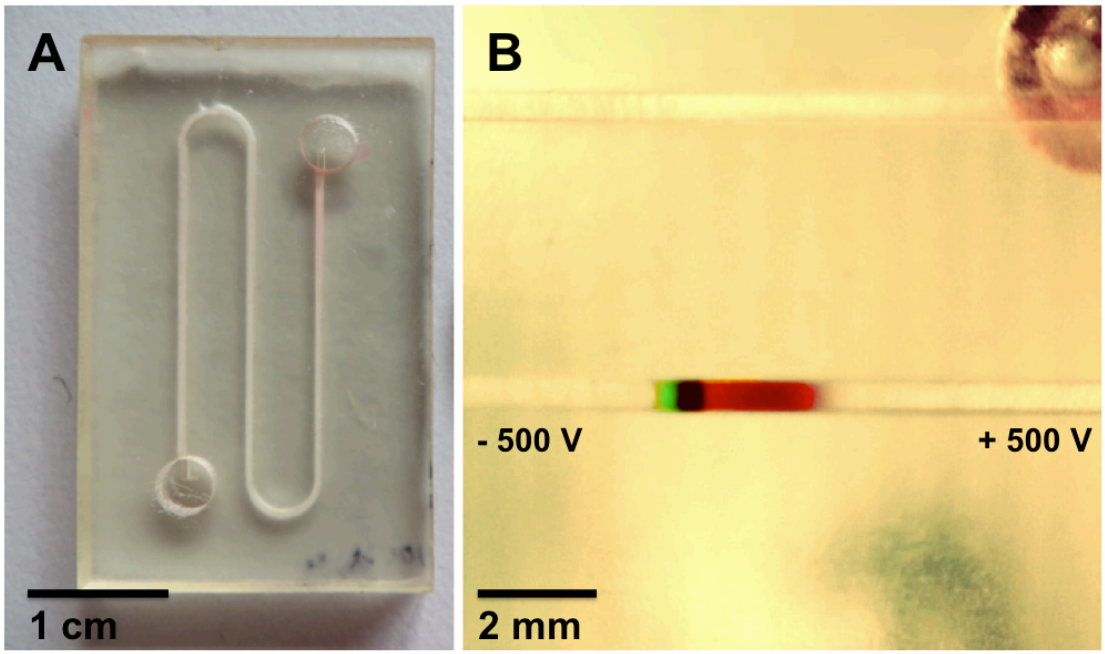

Figure 7.14 ITP separation. (A) Printed microchip used for separation. (B) ITP of three coloured dyes: 1 ppm xylenol orange (red, fastest), 1 ppm carboxy-naphthofluorescein (blue), and 1 ppb fluorescein (green). The leading electrolyte was 10 mM hydrochloric acid adjusted to pH 9 with Tris and 0.5% HPMC. Dyes were dissolved in the terminating electrolyte composed of 1 mM CAPS adjusted to pH 9.4 with Tris. The voltage applied across the channel was 1000 V (100 V/cm).

7.1.2.5 Analysis of Nitrate in Tap Water

Nitrite is an essential nutrient that naturally present in oceans, rivers and groud water but toxic levels can be monitored in industrial effluents, agricultural runoff and wastewater. According to the current World Health Organisation guidelines, maximum permissible nitrite levels in drinking water is 3 mg/L (65.2 μM) for short-term exposure and 0.2 mg/L (4.3 μM) for long-term exposure.[13]

Nitrate levels in surface water are usually very low (0 - 18 mg/L) but nitrate levels in industrial pollution may be higher than this and require quick corrective action from the water treatment plant. Nitrate levels of ≤ 100 mg/L are safe for adults but not for infants less than 3 months old as levels above 50 mg/L can cause methemoglobinemia also known as "blue baby".

Since environmental samples are more abundant, 10s - 100s mL, compared to biological samples, microfluidic dimensions of 10-100 μm are not necessary. Mesofluidic dimensions, 0.5-2.0 mm, are less prone to blocking with turbid samples containing particles up to 100 μm in size. To demonstrate the potential of 3D printing to make complex fluidic microchips, a microchip was designed for continuous monitoring of nitrate in water using the Griess test and standard addition method to correct for the matrix effect. Nitrate is first reduced into nitrite using nitrate- and nitrite-free zinc dust in acid medium then reacted with Griess reagent to produce a distinct pink colour. Batch colorimetric detection was used as the standard method to validate the performance of the printed device (Figure 7.15).

The printed microdevice has four inlets and three fluidic layers (Figure 7.16A) and was 41 mm × 117 mm × 22 mm (width × depth × height) with a print time of 290 min costing US$ 20 per microchip. Despite the longer fabrication time, this

device combines multiple fluidic functional units, allowing an automated standard addition as well as a series of detection cells with increasing path lengths to improve linear range, which greatly increases the field usability of the device. It would be difficult to fabricate an equivalent microchip for the same cost in the same time using any other technique. The top (yellow) and bottom (red) fluidic layers were used to introduce the sample and Griess reagent, respectively. The middle fluidic layer was used for creating a gradient of five concentrations of nitrite covering the range of 0-100 μM, which is equivalent to nitrite ion concentrations of 0 - 4.6 mg/L, and allows online quantitative analysis by standard addition. All solutions were injected using a syringe pump (Pump 33, Harvard Apparatus) at a high flow rate of 2000 μL/min to fill the channels that was then gradually reduced, via a stepwise decrease of 500 μL/min each time. This increases the applicability of the device, as the Griess test is known to be strongly dependent on ionic strength. The effluents from the three layers are combined and fed into five individual mixers where the sample, standards, and reagents are mixed and the colorimetric reaction takes place. A flow rate of 500 μL/min was used to see the pink colour develop in 1 min. A series of detection cells with varying path lengths (0.5 - 15 mm) were incorporated to expand the linear range of the microdevice and allow direct measurement without the need to dilute the sample. Colorimetric detection was performed by image processing of a photograph taken by a digital camera (Canon PowerShot SX260 HS) analysed for intensity through the green channel as negative peaks using ImageJ software.

A photo of the detection region of the microchip is shown in Figure 7.16B for a tap water sample. Nitrate was reduced into nitrite off-chip with zinc dust in acid medium. Colour changes across each row correspond to standard addition of nitrite to the sample using the gradient generator, while the different rows correspond to a

different detection path length. It can be seen from the image that with the highest concentration of standard the pink colour is first visible with a path length of 5 mm, and that the intensity increases with the increased detection path length. It is also apparent when using detection path lengths of ≥ 5 mm, the intensity decreases moving across the chip as the concentration of nitrite added to the sample is decreased. More quantitative analysis is obtained by examination of the green channel from the photo, with data for the 1, 5, and 10 mm detection cells shown in Figure 7.17. The data reveal that it was not possible to measure colour in all of the detection cells with a 1 mm path length, with colours at the two lowest concentrations of nitrate added not being detectable. In contrast, with the 10 mm detection path length, colour saturation is reached at the middle standard, with the same intensity value obtained with additions of higher concentrations of nitrite. The 5 mm detection path length provided the most linear region, although there is slight curvature at the largest standard addition as it approaches saturation. Using this calibration curve, the concentration of nitrate was calculated to be 2.59 ± 10.88 μM (95% confidence interval) in tap water, compared to a concentration of 1.16 ± 1.36 μM using a conventional spectrometer (absorbance at 540 nm). The high error in both the standard and microchip methods is a result of the low concentration of nitrate in tap water, close to the detection limit of the method. The precision could be improved by using a smaller standard addition range, but this was not done to preserve the ability to quantify up to and over the acceptable levels in drinking water. The microchip discussed here offers a very promising approach for online determination of nitrate in water, and the ability to easily integrate multiple detection points with different detection path lengths greatly enhances the field usability of such a microchip.

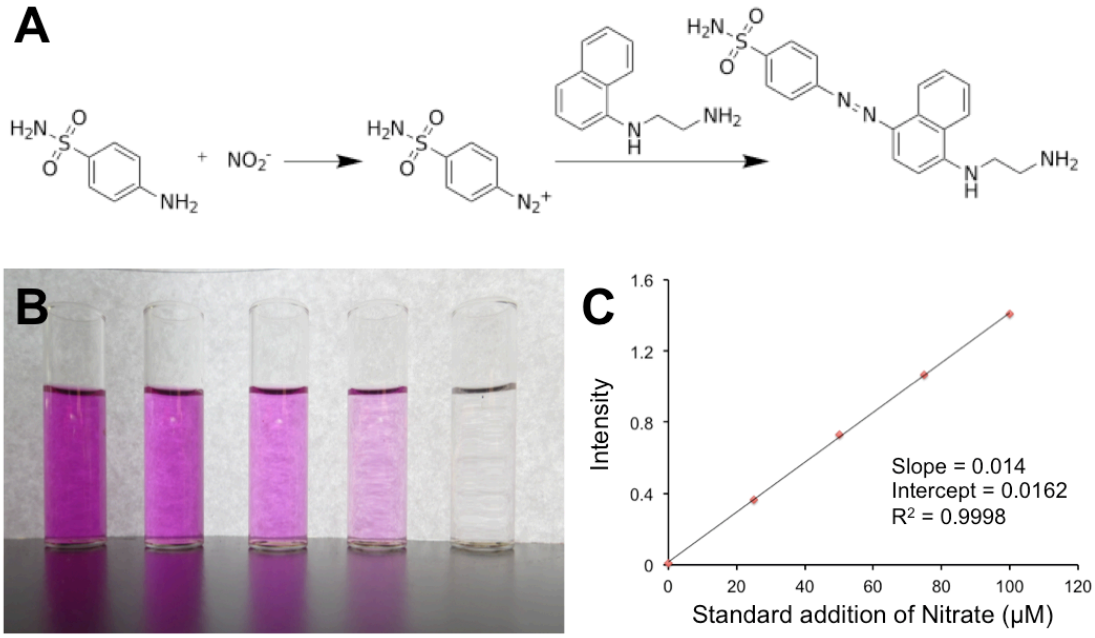

Figure 7.15 Griess test for nitrate after reduction into nitrite. (A) Reaction mechanism. (B) Pink colour intensity is proportional to the added standard concentration of nitrate. (C) Linear calibration range using batch colorimetric detection at 540 nm as the standard method for nitrate determination in tap water.

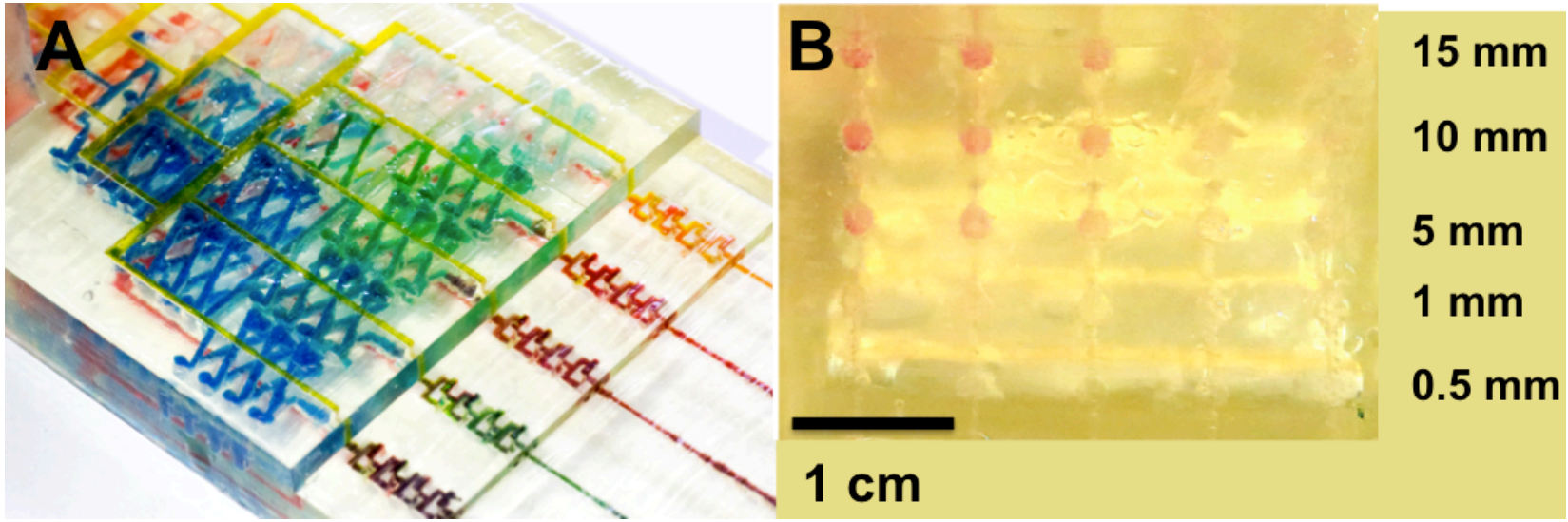

Figure 7.16 Griess test for nitrate in tap water using the printed device. (A) Device filled with coloured solutions to show the different fluidic layers. The top yellow layer is the sample; the middle blue layer shows the gradient generator, and the red layer is the reagent. (B) Photo of the multiple detection points.

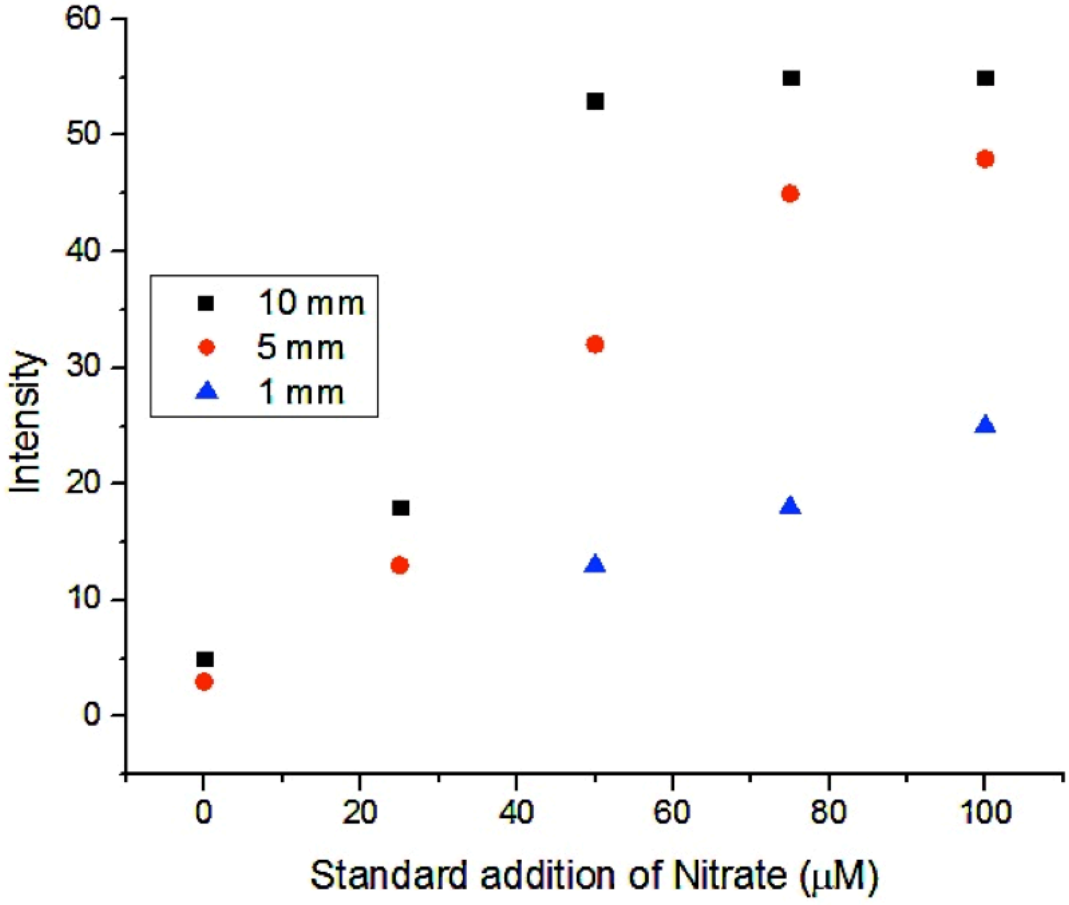

Figure 7.17 Standard addition curves with intensity measured through the green channel as a negative reading with detection path lengths of 1, 5, and 10 mm.

7.1.3 Conclusions

In this work, the capabilities of a commercially available DMD-based 3D printer for the fabrication of microfluidic to millifluidic devices were explored. While there is certainly a room for improvement in hardware and resin chemistry, this is the first report of the use of a low-cost consumer-targeted 3D printer for the direct fabrication of enclosed microfluidic features in a transparent resin. The MiiCraft® provides a good compromise among price, resolution, size and ability to make transparent microchips in the visible spectrum, with devices showing acceptable transmittance above 430 nm. The print time of simple microfluidic devices can be as low as 12 min with a material cost of US $1 per device, making this an attractive approach for rapid prototyping. While this may seem trivial for laboratories with substantial funds, it will expand the scope of microfluidics to be readily available to researchers on a limited budget. A complex 3D microfluidic structure was developed for continuous nitrate analysis. The device comprised three fluidic layers (sample, reagent, and standard addition of nitrite), micromixers, and a series of detection cells with depths increasing from 0.5 to 15 mm to increase the linear range of the colorimetric assay. This complex microdevice was printed in < 5 h and was used to determine the level of nitrate in tap water, with levels agreeing with values determined using an off-chip assay. The low cost of the printer (US$ 2,300 and US$ 138 per 500 mL of clear resin) and the simplicity with which complex 3D microfluidic devices operate offer great potential for improved development of microfluidic applications.

7.2 References

1. Pan, Y.; Zhou, C.; Chen, Y. In *Rapid Manufacturing in Minutes: The Development of a Mask Projection Stereolithography Process for High-speed Fabrication*, ASME 2012 International Manufacturing Science and Engineering Conferences, Notre Dame, Indiana, USA, Notre Dame, Indiana, USA, 2012.
2. (a) Kang, H. W.; Park, J. H.; Cho, D. W., A pixel based solidification model for projection based stereolithography technology. *Sensors and Actuators, A: Physical* **2012,** *178*, 223-229; (b) Zhou, C.; Chen, Y. In *Calibrating Large-area Mask Projection Stereolithography for Its Accuracy and Resolution Improvements*, Proceedings of Solid Freeform Fabrication Symposium, Austin, Texas, USA, Austin, Texas, USA, 2009.
3. Choi, J.-W.; Wicker, R. B.; Cho, S.-H.; Ha, C.-S.; Lee, S.-H., Cure depth control for complex 3D microstructure fabrication in dynamic mask projection microstereolithography. *Rapid Prototyping Journal* **2009,** *15* (1), 59 - 70.
4. (a) Di, L.; Fei, H.; Yang, L.; Jintian, L.; Changning, L.; Jiangxin, S.; Ya, C., Three-dimensional staggered herringbone mixer fabricated by femtosecond laser direct writing. *Journal of Optics* **2013,** *15* (2), 025601; (b) Lim, T. W.; Son, Y.; Jeong, Y. J.; Yang, D.-Y.; Kong, H.-J.; Lee, K.-S.; Kim, D.-P., Three-dimensionally crossing manifold micro-mixer for fast mixing in a short channel length. *Lab on a Chip* **2011,** *11* (1), 100-103; (c) Xia, H. M.; Wan, S. Y. M.; Shu, C.; Chew, Y. T., Chaotic micromixers using two-layer crossing channels to exhibit fast mixing at low Reynolds numbers. *Lab on a Chip* **2005,** *5* (7), 748-755; (d) Therriault, D.; White, S. R.; Lewis, J. A., Chaotic mixing in three-dimensional microvascular networks fabricated by direct-write assembly. *Nature Materials* **2003,** *2* (4), 265-271.

5. Carriere, P., On a three-dimensional implementation of the baker's transformation. *Physics of Fluids* **2007,** *19* (11), 118110-4.
6. Liao, Y.; Song, J.; Li, E.; Luo, Y.; Shen, Y.; Chen, D.; Cheng, Y.; Xu, Z.; Sugioka, K.; Midorikawa, K., Rapid prototyping of three-dimensional microfluidic mixers in glass by femtosecond laser direct writing. *Lab on a Chip* **2012,** *12* (4), 746-749.
7. Gao, Y.; Sun, J.; Lin, W.-H.; Webb, D.; Li, D., A compact microfluidic gradient generator using passive pumping. *Microfluid Nanofluid* **2012,** *12* (6), 887-895.
8. Lee, K.; Kim, C.; Kim, Y.; Ahn, B.; Bang, J.; Kim, J.; Panchapakesan, R.; Yoon, Y.-K.; Kang, J.; Oh, K., Microfluidic concentration-on-demand combinatorial dilutions. *Microfluidics & Nanofluidics* **2011,** *11* (1), 75-86.
9. Neils, C.; Tyree, Z.; Finlayson, B.; Folch, A., Combinatorial mixing of microfluidic streams. *Lab on a Chip* **2004,** *4* (4), 342-350.
10. Zhao, S.; Cong, H.; Pan, T., Direct projection on dry-film photoresist (DP2): do-it-yourself three-dimensional polymer microfluidics. *Lab on a Chip* **2009,** *9* (8), 1128-1132.
11. (a) Ben-Tzvi, P.; Rone, W., Microdroplet generation in gaseous and liquid environments. *Microsystem Technologies* **2010,** *16* (3), 333-356; (b) Teh, S.-Y.; Lin, R.; Hung, L.-H.; Lee, A. P., Droplet microfluidics. *Lab on a Chip* **2008,** *8* (2), 198-220; (c) Theberge, A. B.; Courtois, F.; Schaerli, Y.; Fischlechner, M.; Abell, C.; Hollfelder, F.; Huck, W. T. S., Microdroplets in microfluidics: An evolving platform for discoveries in chemistry and biology. *Angewandte Chemie International Edition* **2010,** *49* (34), 5846-5868.
12. Li, W.; Young, E. W. K.; Seo, M.; Nie, Z.; Garstecki, P.; Simmons, C. A.; Kumacheva, E., Simultaneous generation of droplets with different dimensions in

parallel integrated microfluidic droplet generators. *Soft Matter* **2008,** *4* (2), 258-262.

13. WHO, Guidelines for drinking-water quality. 3rd ed.; World Health Organization: Geneva, Switzerland, 2008.

8 Conclusions and Future Directions

Low-cost portable devices were developed using two different approaches. First, controlled dielectric breakdown was used to form nanojunctions, which is more accessible than conventional nanofabrication techniques. Second, fast-prototyping with a desktop SL 3D-printer was employed to fabricate microfluidic devices for different applications.

Nanojunctions integrated on-chip served as electrokinetic filters for sample pretreatment by permitting or blocking ionic species within a certain size/mobility range. The low-cost and simplicity of the method make it suitable for disposable devices. Applications include TDM of pharmaceuticals in blood like quinine (using single nanojunction) and ampicillin (using the SMTs). Small organic acids in blood acts as biomarkers for some disease states like DKA. Their extraction from whole blood was feasible within 60 s using the single nanojunction format and the LOD was 12.5 mM.

Biopolymers like proteins and DNA are very important biomarkers for prediction, early stage diagnosis and management of a progressing disease condition. Biomarker proteins present in very low concentration and require enrichment before analysis. Up to 80-fold enrichment was achieved using the single nanojunction format. Also, DNA was extracted from blood, enriched and desalted using the SMTs. LOD of 12.5 nM was achieved and can be improved by using a more sensitive detection method. These extraction and enrichment methods can be easily coupled with other analysis techniques for diagnostic applications.

The controlled dielectric breakdown method was optimized for PDMS. From this point, I would like to proceed to other materials that could be better suited for large

scale manufacturing like PMMA and other thermoplastics. Quinine and ampicillin were used as model drugs that can be easily detected because of native fluorescence or the availability of easy and simple labelling. Indirect detection enables the quantitation of non-fluorescent compounds but at compromised detection limits. Other drugs may require other labelling techniques or detection methods. While LOD achieved were optimum for the selected drugs, in the range of μg/mL, other drugs like the tricyclic antidepressant amitriptyline and the immunosuppressant tacrolimus, require detection in the lower ng/mL range. One approach to increase sensitivity will be through increasing the amount of analyte injected by either using a material that forms a highly porous nanojunction after dielectric breakdown or having multiple breakdown points. Alternatively, hydrogels with high surface charge can be useful but they are more laborious to integrate on a chip than the dielectric breakdown and they are more likely to deform under high applied electric field.

In the second part of this project, the microfabrication capabilities of a desktop 3D-printer based on SL were utilized for fast prototyping of devices that integrate commonly used in analytical processes like mixing, gradient generation and droplet extraction. It will be interesting to try other designs with integrated mechanical moving parts and valves for controlled fluid handling. For all the printed devices, I used the commercially available resin supplied by the Miicraft manufacturer. Other photocurable resins like Ormocomp® can offer better surface and antifouling properties. The technology is evolving at a very fast rate that the realization of true microfluidic dimensions is not far away.

9 Appendix

9.1 Controlled Dielectric Breakdown

9.1.1 Microfluidic Device

The microfluidic device is hybrid PDMS/glass with either single or double V-channel(s). Master templates with positive relief were made from PerMX (DuPont, NC, USA) or SU-8 photoresist according to manufacturer's instructions. All microchannels were 30 μm deep. All separation channels were 50 μm wide while the V-channels were 500 μm wide. The tips of the V-channels were separated by a 100 μm from the separation channel. The SMT design had two V-channels that were offset from each other by 500 μm.

A 10:1 (w/w) mixture of Sylgard 184 PDMS elastomer base and curing agent (Dow Corning Corporation, Midland, MI, USA) was degassed, placed on positive relief PerMX or SU-8 templates made in house on PMMA slides, degassed again, and heated in an oven at 70°C for 1 h. The PDMS cast and soda glass slide were plasma treated with handheld corona discharge device (model BD-20, 230 V power supply, Electro Technic Products) for 15 s and placed in conformal contact for 12 h in the oven at 70^{o}C to ensure complete binding.

9.1.2 Breakdown Procedure

Immediately before use, all channels were filled with breakdown electrolyte; 10 mM phosphate buffer, pH 11, or 50 mM potassium chloride. A breakdown voltage of 2200 V (electric field strength 22 V/μm) was applied across the 100 μm gap using a power supply that is controlled through LabView or an in-house regulated power supply.

9.1.3 Chemicals

9.1.3.1 Permeability Studies

Fluorescein, BSA, and fluorescamine for fluorescent tracking and reagents to prepare the buffers were purchased from Sigma-Aldrich Co. CNF from Molecular Probes (Oregon, USA) was prepared in 10 mM phosphate solution (pH 11.7) to obtain 200 μg/mL solution. Simultaneous transport of inorganic ions was done using 0.1 g/mL solutions of iron (III) nitrate ($Fe(NO_3)_3.9H_2O$) from ChemSupply (Beverley, S.A., Australia) and potassium thiocyanate (KSCN) from Ajax chemicals (Sydney, Australia) in 100 mM nitric acid (HNO_3) from Merck (VIC, Australia). All solutions were prepared in Milli-Q water obtained from a Millipore (North Ryde, Australia) purification system.

BSA was labelled with fluorescamine by mixing 200 μL of 250 μg/mL in 10 mM phosphate and 0.9% (w/v) NaCl, with 20 μL of 10 mM fluorescamine in acetone. NaCl was obtained from Merck (Darmstadt, Germany).

9.1.3.2 Quinine Analysis

Quinine sulphate monohydrate is (3ξ,8α)-6'-Methoxycinchonan-9-ol sulfate hydrate (1:1:1) and has a molecular weight of 440.510 Da. Its chemical formula is $C_{20}H_{28}N_2O_7S$. The structural formula is:

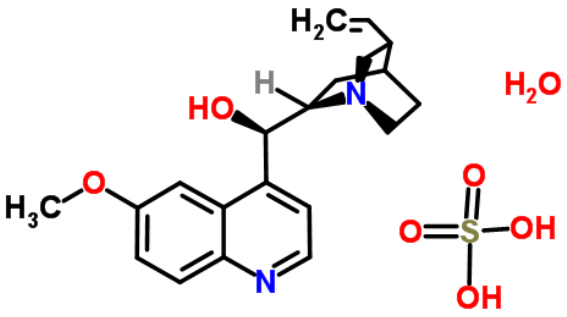

Quinine sulphate monohydrate (from Aldrich, Milwaukee, USA) was used to prepare 100 mg/mL stock solution in 3 mM sulphuric acid. This solution was used to spike blood samples to obtain 1 mg/mL. Different concentrations (0.5, 1.0, 2.5, 10.0, and 25.0 μg/mL) were obtained by serial dilution with whole blood.

ITP electrolytes for quinine analysis. LE of 10 mM sodium acetate (BDH, VIC, Australia), 20 mM acetic acid, 1 mM NaH_2PO_4, (pH 4.3) in presence of 0.1% (w/v) HPMC and TE of 10 mM β-alanine (Sigma-Aldrich, Steinheim, Germany) and 10 mM acetic acid (pH 4.2).

9.1.3.3 Small Organic Acids

The organic acids chosen were pyruvate, lactate, and β-hydroxy butyrate. Pyruvate is 2-Oxopropanoate and has a molecular weight of 87.055 Da. Its chemical formula is $C_3H_3O_3$. The structural formula is:

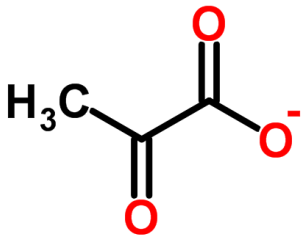

Lactate is 2-Hydroxypropanoate and has a molecular weight of 89.071 Da. Its chemical formula is $C_3H_5O_3$. The structural formula is:

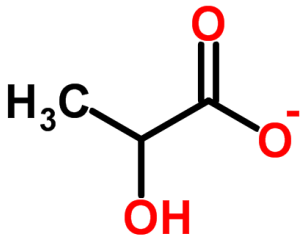

β-hydroxy butyrate is 3-Hydroxybutanone and has a molecular weight of 103.097 Da. Its chemical formula is $C_4H_7O_3$. The structural formula is:

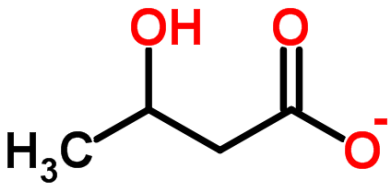

Stock solutions (25 mM) of the acids in 100 mM NaCl were prepared from their sodium salts and stored in the fridge.

ITP electrolytes for organic acids analysis. The LE was 20 mM HCl titrated with β-alanine to pH 3.3, 1% polyvinyl pyrrolidone (PVP) to suppress the EOF, and 250 μM R6G. The TE was 50 mM propionic acid. Stock solutions with double the concentrations were stored in the fridge and the LE was prepared daily by mixing equal amounts of the buffer-PVP and R6G.

9.1.3.4 Ampicillin Analysis

Ampicillin sodium is monosodium (2S, 5R, 6R)-6-{[(2R)-2-amino-2-phenylacetyl]amino}-3,3-dimethyl-7-oxo-4-thia-1-azabicyclo[3.2.0]heptane-2-carboxylate and has a molecular weight of 371.387 Da. Its chemical formula is $C_{16}H_{18}N_3NaO_4S$. The structural formula is:

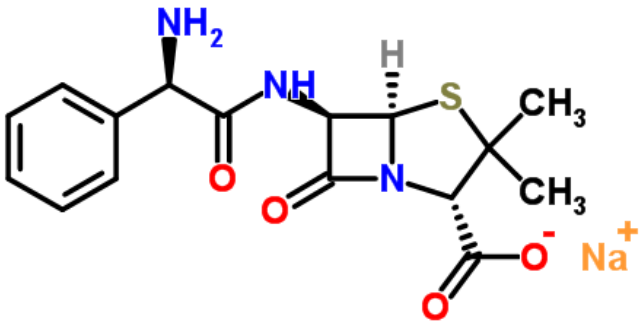

Whole blood samples from a healthy volunteer were treated with disodium salt of ethylene diamine tetraacetic acid (EDTA) to prevent coagulation and divided into small volumes (200 μL) then stored in the freezer at -4^{o}C.

9.1.3.5 Protein Labelling and Denaturing

Individual protein solutions were prepared: Insulin (5.8 kDa, pI = 5.3) at 5 mg/mL in 50 mM $NaHCO_3$, Apotransferrin (78 kDa, pI = 6.1) at 10 mg/mL in water, β-lactoglobulin (18.4 kDa, pI = 5.1) at 10 mg/mL in water, ovalbumin (44.3 kDa, pI = 4.54, 4.9) at 20 mg/mL in water, and BSA (66.4 kDa, pI = 4.7, 4.9) at 20 mg/mL in water.

In individual vials, 20 μL of each protein solution (40 μL for insulin) were mixed with 120 μL (60 μL for insulin) of 100 mM $NaHCO_3$, and then labelled with 60 μL (30 μL for insulin) freshly prepared fluorescamine (3 mg/mL in acetone).

Equal volumes of the labelled protein and SDS sample buffer were mixed then heated to 100^{o}C using a heating block for 6 min. The SDS sample buffer was 100 mM Tris, 2% SDS, 4% Dithioerythritol (DTT), and pH adjusted to 6.8 with HCl.

Each solution was diluted to the desired concentration with buffer (100 mM Tris-phosphate, pH 8.3, 0.1% SDS and 10% glycerol).

9.1.3.6 Short ssDNA

Stock solution of 5 μM fluorecein-labelled ssDNA, in 10 mM Tris-HCl buffer (pH 8.0), was diluted as necessary for each experiment.

9.1.4 Detection

Permeability studies were recorded with a high-definition colour CCD camera head (Digital Sight DS-Fi1c, Nikon, Japan) mounted on an inverted fluorescence microscope (Nikon, Eclipse Ti-U, Japan) fitted with and operated with NIS-Elements BR 3.10 software (Melville, NY, USA). Filters were purchased from Semrock (Rochester, NY, USA); 1) multiband pass (excitation wavelength (λ_{ex}) at 390, 482, 563 and 640 nm and emission wavelength (λ_{em}) at 446, 523, 600 and 677 nm), 2) blue filter (λ_{ex} at 450-490 nm and λ_{em} at 520 nm) and 3) violet filter (λ_{ex} at 380-420 nm and λ_{em} at 450 nm).

Quantitative measurements were done using a photomultiplier tube (Hamamatsu Photonics KK, Hamamatsu, Japan) connected to the microscope. Data acquisition was made using an Agilent interface (35900E) connected to a laptop and operated by Agilent ChemStation for LC software (Agilent Technologies, Waldbronn, Germany).

Indirect fluorescence detection of organic acids was made using blue LED as the excitation source. Fluorescence intensity was measured using a photon counter. Data acquisition was made by computer using a LabView program with 100 ms gate time.

9.1.5 Power Supply

Breakdown voltage was supplied using one of the following power supplies:

a) 2-channel power supply controlled through LabView with current feedback and down regulates the applied voltage to maintain a certain current through the nanojunction.

b) 2-channel power supply (0-3 kV) with a built-in current feedback and completely stops the applied voltage once the current limit is reached.

Permeability studies and electrophoretic analysis were done using an in-house 4-channel (0-5 kV) dc power supply to apply an electrical potential to each reservoir through a custom-designed interface connected to 5 or 6 platinum electrodes. Platinum electrodes connected to a single V-channel shared the same voltage channel and hence provided the same voltage.

9.2 3D-Printing

9.2.1 Miicraft® Printer

The Miicraft® (Miicraft, Hsinchu, Taiwan) is a DMD-based 3D printer with bottom-up projection. It uses an Open Source Arduino Mega 2560 microcontroller board and Python-based software as the controller and slicer. The light source is a DLP pico-projector (450 ppi) with standard WVGA resolution (854 × 480 pixels). The fully automated system allows fabrication of models of up to 43 mm × 27 mm × 180 mm ($x \times y \times z$) at printing speeds of 20 mm/h in height regardless of the design complexity. The xy resolution is 56 μm × 56 μm and the z resolution is 50 or 100 μm. The printer size is 20.5 cm × 20.8 cm × 33.5 cm (width × depth × height) and weighs 6.5 kg.

The colourless resin is proprietary, consists of a modified acrylate oligomer and monomer, an epoxy monomer, a photoinitiator, and additives, and has a low viscosity of 186 cps.

9.2.2 Microfluidic Applications

9.2.2.1 Mixing

Dye solutions were prepared in Milli-Q water at 0.1 μg/mL fluorescein (green) and 1 μg/mL rhodamine B (red). A syringe pump (Pump 33, Harvard Apparatus) was used to provide a flow rate of 100 μL/min for both inlets. Fluorescence images were taken with a USB microscope (Dino-Lite Premier AM4113T-GFBW) fitted with a blue light-emitting diode for excitation and a 510 nm emission filter.

9.2.2.2 Gradient Generation

Dye solutions, bromothymol blue (blue) and rhodamine B (red), were prepared in methanol at 1 mg/mL each and the flow rate was 1 mL/min at both inlets. Light images were recorded with a digital camera (Canon PowerShot SX260 HS).

9.2.2.3 Droplet Extraction

Aqueous phase contained a mixture of two fluorescent dyes (1 μg/mL each), coumarin 334 (green) and rhodamine B (red), and the organic phase was decanol merged. The flow rates of both the aqueous sample and decanol were set at 1 μL/min.

9.2.2.4 Isotachophoresis

The sample mixture composed of three anionic dyes, 1 ppm xylenol orange (red, fastest), 1 ppm CNF (blue), and 1 ppb fluorescein (green) dissolved in TE. The ITP system employed a LE composed of 10 mM hydrochloric acid adjusted to pH 9 with Tris and 0.5% HPMC to suppress the EOF. The dyes were dissolved in the TE composed of 1 mM CAPS adjusted to pH 9.4 with Tris. The voltage was applied from the same power supply described earlier for electrophoretic separation.

9.2.2.5 Analysis of Nitrate in Tap Water

Standard nitrite solution was freshly prepared from sodium nitrite at 100 μM concentration. Nitrate was first reduced into nitrite using nitrate- and nitrite-free zinc dust in acid medium. All solutions were injected using a syringe pump (Pump 33, Harvard Apparatus) at a high flow rate of 2000 μL/min to fill the channels that was then gradually reduced, via a stepwise decrease of 500 μL/min each time. A flow rate of 500 μL/min was used to see the pink colour develop in 1 min. Colorimetric detection was performed by image processing of a photograph taken by a digital camera (Canon PowerShot SX260 HS) analysed for intensity through the green channel as negative peaks using ImageJ software.